

Search for a neutral technicolor signature in $p\bar{p}$ collisions at $\sqrt{s} = 1.8$ TeV

by

Jesse Andrew Green

A dissertation submitted to the graduate faculty
in partial fulfillment of the requirements for the degree of
DOCTOR OF PHILOSOPHY

Major: High Energy Physics

Major Professor: E. Walter Anderson

Iowa State University

Ames, Iowa

2001

Copyright © Jesse Andrew Green, 2001. All rights reserved.

Graduate College
Iowa State University

This is to certify that the Doctoral dissertation of
Jesse Andrew Green
has met the dissertation requirements of Iowa State University

Committee Member

Committee Member

Committee Member

Committee Member

Major Professor

For the Major Program

For the Graduate College

To my mother, Kristin.

TABLE OF CONTENTS

1	INTRODUCTION	1
2	THE STANDARD MODEL	3
3	TECHNICOLOR THEORY	6
4	THE DØ EXPERIMENT: A COLLIDER DETECTOR	8
	Introduction	8
	The DØ Experiment	10
	DØ Coordinate System and Transverse Energy	14
	Data Acquisition	15
	Luminosity	16
5	OVERVIEW OF THE SEARCH	17
	Physics Variables	18
	Search outline	20
6	DATA SELECTION	25
	Photon Identification	26
	b-jet Identification	29
	Missing Transverse Energy (\cancel{E}_T)	31
7	BACKGROUND CALCULATION	32
8	TECHNICOLOR MONTE CARLO AND ACCEPTANCE CORRECTIONS	41
	Acceptance Corrections	43
	b-tagging Correction	43
	HITSINFO (no hits in road) Correction	43
	CLEAN Correction	44

9 NEURAL NETWORK IMPLEMENTATION	49
The Input Layer: Physics Variables	50
The Hidden Layer	51
The Output Layer: D_{NN}	52
Training-Sample Selection	54
Other Considerations for Training	54
10 FINAL EVENT SELECTION USING NEURAL NETWORKS	57
11 RESULTS	59
The Search	59
The Method for Computing the Technicolor Cross-Section Limits	60
Technicolor 95% cross-section limits	62
APPENDIX A PYTHIA PARAMETERS USED TO GENERATE TECHNICOL- OR EVENTS	83
APPENDIX B OTHER EXPERIMENTAL SEARCHES FOR TECHNICOLOR . .	85
Searches at CERN Large Electron Positron (LEP) Collider Experiments	85
Searches at Fermilab	86
BIBLIOGRAPHY	91

LIST OF TABLES

Table 6.1	Shown are the results from the event selection cuts, excluding the NN cut. A typical Signal MC is shown for comparison. The acceptance correction efficiencies are included, and are described in Chapter 8.	27
Table 6.2	Definition of the road volume for a photon candidate [19]. This volume is inside the tracking chamber between the EM calorimeter signature and event vertex. .	28
Table 6.3	Definition of the standard HITSINFO cuts [17, 19]. Candidates passing this cut have a higher probability of being a photon. This probability is sometimes referred to as photon purity.	29
Table 6.4	Requirements for a μ -tag indicating a b-quark jet in terms of detector variables. MTC refers to muon tracks in the calorimeter.	30
Table 8.1	An example $\omega_T \rightarrow \gamma\pi_T$ event generated by PYTHIA. The ω_T does not show up since it is a virtual particle in the propogator, and PYTHIA only stores real particles for the event.	42
Table 8.2	Technicolor Monte Carlo (PYTHIA v6.126 with GEANT, SHOWERLIB). Shown are all of the mass combinations generated for this analysis. The quantity $A \times \epsilon$ is the fraction of events passing selection cuts with the correction applied. The last column is the relative fraction of technicolor and background events passing a NN cut of $D_{NN} > 0.9$	48
Table 11.1	Results of choosing the D_{NN} cut based on the discovery significance, $S/\sqrt{S+B}$. The σ deviation is given for the cases where the number of b -tagged data events exceeds the background calculation.	64
Table 11.2	Results summary of $\sigma \times BR$ limits at the 95% confidence level. The D_{NN} cut was selected by minimizing the <i>expected</i> 95% CL, which is a calculation based only on signal and background events as a function of D_{NN} ($S(D_{NN})$ and $B(D_{NN})$). .	65

LIST OF FIGURES

Figure 3.1	Leading-Order (LO) diagram for Techni-Omega production. In this case, the Z^0 or γ may be produced “off mass shell” and thus can mix with the ω_T/ρ_T^0 , since the quantum numbers ($S = 1, Q = 0$, color singlet, etc.) are the same.	7
Figure 4.1	The DØ detector. Shown are the central tracking, the calorimeter and muon systems. The beam enters both sides of the detector along the cylindrical axis. The pipe which is offset from the center is the beam-pipe for the main-ring. The Main Ring is the preaccelerator for the Tevatron, and for historic reasons only clears the Tevatron by about 90 inches at the DØ interaction region.	10
Figure 4.2	The DØ calorimeter system detail.	11
Figure 4.3	The DØ central tracking system detail.	12
Figure 5.1	Leading Order Feynman diagrams for single direct photon production: one of the ways that $\gamma b\bar{b}$ gets produced. Initial state quarks and gluons are on the left side of each diagram; final state particles are on the right side.	18
Figure 5.2	An example technicolor signal sample superimposed on background distributions. These show the variables considered for discrimination between technicolor and background before arriving on the final list of five.	22
Figure 5.3	Discriminating physics variables continued.	23
Figure 5.4	Discriminating physics variables continued.	24

Figure 7.1	The top plot shows the jet E_T tag-rate, $f(E_T)$, and has been normalized. It is assumed to be independent of η and run-number, and is one of the three components of the tag-rate function. The other two components are the normalization as a function of run-number, $N(r)$, and the tagged-jet η dependence, $\epsilon(\eta, r)$ (shown in the next figure). The bottom plot shows the run-range, r , dependence to the tag-rate function, and is a demonstration of how the efficiency of the DØ muon detector changed with time.	36
Figure 7.2	These show the other major component, $\epsilon(\eta, r)$, of the tag-rate function. The vertical axis is the rate of the number of μ -tagged jets over the number of untagged jets. The muon detection efficiency changed in different η -regions of the detector at different times, so the run number dependence is necessary in the function, $\epsilon(\eta, r)$, but not in $f(E_T)$	37
Figure 7.3	Plots showing comparison of Tag-Rate shapes to tagged data. The observables shown here and in the plots that follow show the bin-to-bin correspondence between the background calculation and μ -tagged data for several physics variables.	38
Figure 7.4	Plots showing comparison of Tag-Rate shapes to tagged data. The observables shown here and in the plots that follow show the bin-to-bin correspondence between the background calculation and μ -tagged data for several physics variables.	39
Figure 7.5	These plots also compare background shapes to tagged data. The five observables shown here are used in training the neural networks.	40
Figure 8.1	Here are five observables which show how technicolor would present itself in the data for 3 different mass values compared with background distributions, with the background calculated using the tag-rate method described in Chapter 7. These five variables have excellent signal-to-background discrimination properties, and are used in training the 32 neural networks to search for technicolor events in the data.	45
Figure 8.2	These are some of the variables that were considered for NN training, but not currently used. They either have relatively little discrimination power or are redundant in conjunction with the five NN variables currently in use.	46

Figure 8.3	The physics- η variables of the γ and the two leading jets. The Monte Carlo events are shown to correspond well to the background events derived from $D\bar{O}$ data. It can also be seen that the η distribution alone is not an effective discriminator between technicolor MC and background.	47
Figure 9.1	Diagram showing the node structure of a feed forward neural network with multiple inputs, one hidden layer, and a single output node, which is the neural network discriminant, D_{NN} . The input nodes correspond to the set of input physics variables selected to best discriminate between signal and background events.	50
Figure 9.2	This is the “activation function” used to give the output value at each of the hidden nodes and the output node, D_{NN} . The function origin is the threshold value, θ , and may be different for each node.	52
Figure 9.3	An example output of a neural network trained on a set of untagged technicolor signal events and a subset of untagged γjj data. The arrow shows where the D_{NN} cut was placed to get the best discrimination between signal and background by finding the minimum expected cross-section limit. Chapter 10 discusses the selection of the D_{NN} cut for each neural network trained at each technicolor mass point.	55
Figure 9.4	These plots show the comparison between the background calculation as a function of D_{NN} and the b -tagged data for 3 examples of neural networks. The events here pass the event selections mentioned in Section 6. There are 218 b -tagged data events to compare with 32,067 untagged events applied to the tag-rate function. The χ^2 comparison indicates good agreement between the data and background. This visual also shows the <i>lack</i> of evidence for technicolor events in the data for these 3 mass ranges.	56

- Figure 11.1 Shown in this and in the following figure are the observables used in training the neural networks. The dashed-line signal is normalized to $L = 105 \text{ pb}^{-1}$, and corresponds to one of the mass points that has been *excluded*. The left side plots correspond to data, background, and technicolor events passing event selection cuts. Each plot on the right side shows the sub-sample of events passing an optimal D_{NN} cut. The NN was trained on the shown signal, and the NN response to the signal in the right-hand plots is consistent. The cut of $D_{NN} \geq 0.83$ was selected to minimize the expected 95% confidence limit. See Figure 11.9 for the D_{NN} spectrum in this case. 66
- Figure 11.2 Shown are the remaining neural network variables continued from the previous page. This also shows before and after the optimal D_{NN} cut for the technicolor mass point $M(\omega_T) = 160 \text{ GeV}$, and $M(\pi_T) = 80 \text{ GeV}$. This mass point has been excluded at the 95% CL. See Figure 11.9 for the D_{NN} spectrum in this case. 67
- Figure 11.3 This case shown is for $M(\omega_T) = 140, M(\pi_T) = 80 \text{ GeV}$, which is one of the mass-points having an excess of data over background. See Table 11.1 for the results of this case. Here also, the right-hand plots use a D_{NN} cut optimized to maximize the discovery significance formula, $S/\sqrt{S+B}$ as discussed in Chapter 10. See Figure 11.8 for the D_{NN} spectrum in this case. 68
- Figure 11.4 Continued from 11.3. See Figure 11.8 for the D_{NN} spectrum in this case. . . . 69
- Figure 11.5 The case shown is for $M(\omega_T) = 160, M(\pi_T) = 40 \text{ GeV}$, which is one of the mass-points having an excess of data over background. Also, see Table 11.1. Here also, the D_{NN} cut for the right-hand plots is set to maximize the discovery significance formula $S/\sqrt{S+B}$. See Figure 11.8 for the D_{NN} spectrum in this case. 70
- Figure 11.6 Continued from 11.5. See Figure 11.8 for the D_{NN} spectrum in this case. . . . 71

Figure 11.7	Optimization results. These plots and the ones that follow illustrate the selection of the neural network discriminant (D_{NN}) cut for every technicolor mass point in this analysis by finding the minimum <i>expected</i> 95% CL (dependent only on the technicolor and background acceptances). Also shown on each plot are the 95% CL, $\sigma \times BR$, and number of accepted technicolor, data, and background events passing all cuts including the D_{NN} cut. If the 95% CL shown is less than the $\sigma \times BR$ for a mass point, then this mass point is considered to be excluded. The numbers shown are the same as in Table 11.2.	72
Figure 11.8	Optimization results continued. Compare with Table 11.2.	73
Figure 11.9	Optimization results continued. Compare with Table 11.2.	74
Figure 11.10	Optimization results continued. Compare with Table 11.2.	75
Figure 11.11	Optimization results continued. Compare with Table 11.2.	76
Figure 11.12	Optimization results continued. Compare with Table 11.2.	77
Figure 11.13	Optimization results continued. Compare with Table 11.2.	78
Figure 11.14	Optimization results continued. Compare with Table 11.2.	79
Figure 11.15	Optimization results continued. Compare with Table 11.2.	80
Figure 11.16	Optimization results continued. Compare with Table 11.2.	81
Figure 11.17	Optimization results continued. Compare with Table 11.2.	82
Figure B.1	The mass exclusion region measured by the L3 collaboration [34].	86
Figure B.2	The mass exclusion region measured by the DELPHI collaboration [35].	87
Figure B.3	The mass exclusion region measured by the CDF collaboration [36].	88
Figure B.4	The mass exclusion region measured by the CDF collaboration [37].	89
Figure B.5	The mass exclusion region measured by the DØ collaboration [38].	90

ACKNOWLEDGEMENTS

I have many people to thank. For starters, I wish to thank my advisor, Walter Anderson, and John Hauptman at Iowa State University, for their positive encouragement, financial support, advice, mentoring, and “going to bat” for me on numerous occasions. I also thank the hard work of my other committee members for their contributions and for the excellent courses that they have taught me. Thanks goes to German Valencia, Michael Strevens, and Dave Carter-Lewis.

I also wish to thank Pushpa Bhat and John Womersley for the discussions about Technicolor and for this topic of research that has become my thesis. In the Exotics group, I thank Greg Landsberg for his encouragement, patience and for teaching me how to ski, and I thank Tom Ferbel, Hugh Montgomery, and Iain Bertram for their encouragement and advice in many areas.

I think the definition of a great working environment is a place in which your friends and closest colleagues tend to be the same people. I thank John Krane for our excellent discussions, about physics and life, for his friendship, and for just being a cool and wise person in general. Linda Coney has been a rock of support for the past couple of years, and I thank her for her friendship, advice and encouragement. Brian Connolly has also been a great friend, and I am grateful for our numerous discussions and friendship. I would also like to thank Jeff McDonald, Russ Gilmartin, Tina Hebert, John Zhou, and anyone else whom I may have forgotten that has been a friend to me or has helped me out in some way.

There are a few people who definitely helped me keep my feet on the ground, *except* for that time when Kevin and I jumped out of a perfectly good airplane, while Chris took pictures. These people are Chris and Julie Green, Kevin and Nichole Davis, Sam Zeller, Sarah Martin, Florencia Canelli, Ben Kilminster, Yuri and Mosha Gerstein, Mary Anne Cummings, Saul Youssef, and Robin Erbacher.

My friends and fellow graduate students at Iowa State have been great people to know and to work with. Thanks go to Mike Tammaro, Wendy and Lars Ewell, Lori and Mark Bransford, Kristal Mauritz, Matt Breitwisch, and John Zhou.

I wish to give special thanks to Julianne Hill for the wonderful, supportive, and fun friendship that

we have had for nearly a decade. My mentor while I was at Creighton University for my M.S., Janet Seger, and my instructors, in particular, Michael Cherney, Robert Kennedy, and Fr. T.S. McShane, also deserve special thanks for getting me started in high-energy physics and for creating such a warm atmosphere in which to learn. I have many good memories of that time.

I am eternally grateful to my physics/calculus/computer science teacher at Caddo Magnet High School, Otto Sellers, for awakening within me abilities that I didn't know existed. I also thank Ascension Smith for organizing one of the best pilot magnet high school programs in the country. I appreciate the long-standing friendship with Allen Childress (thanks for the tips on neural networks!) and his parents Bruce and LuEllen. I would also like to thank Tigger and Ginger, who have been with me for so many years, and without whom my life would be *far* less entertaining.

I wish to thank my brother, John, for believing in me and occasionally reciting poems on my answering machine. Lastly, I thank my mother, Kristin, who has given me a constant level of support and encouragement from the beginning. Among many other things, I thank her for my love of science and nature, gifts beyond price.

ABSTRACT

The standard model (SM) of particle physics has been a very successful theory for decades; however, several features remain unexplained. One such feature is the mechanism of electro-weak symmetry-breaking. The Higgs mechanism is postulated as part of the SM to give us the masses of the W^\pm and the Z^0 bosons in a manner consistent with unitarity. The Higgs boson is a consequence of the mechanism currently used. It is massive, and has the quantum numbers of the vacuum; *i.e.* it is a scalar. Also, the pattern of fermion (quark and lepton) masses is yet to be understood. Technicolor introduces a new force and particles (techniquarks and technileptons), which can break electroweak symmetry and generate the vector boson masses without introducing fundamental scalars. Along with some necessary extensions to the theory, technicolor provides the known fermion masses, and it also predicts many new “techni-mesons.”¹ Previous searches for various technicolor channels have been performed throughout the high-energy physics community at CERN on the L3 and DELPHI Experiments, and at Fermilab on the CDF and DØ Experiments.² At the DØ experiment, we use neural networks to search for the lightest techni-mesons in a sample of $\gamma b\bar{b}$ data at the Tevatron. They are the techni- ω (ω_T) and its mass-degenerate techni- ρ (ρ_T^0), which decay to a γ and a techni-pion (π_T/π_T'). For the technicolor models considered, the π_T/π_T' decays predominantly to $b\bar{b}$. This analysis searches for ω_T/ρ_T^0 production using many Monte Carlo signal samples on the $M(\omega_T)$ vs. $M(\pi_T)$ mass plane. No evidence was found for the production of neutral technicolor particles in this channel, and 95% confidence level upper limits on cross-section \times branching ratio ($\sigma \times BR$) are computed.

¹E. Eichten, K. Lane and J. Womersley, “Finding Low-Scale Technicolor at the Tevatron,” *Phys. Lett. B* **405** 305 (1997), hep-ph/9704455; E. Eichten, K. Lane, “Low-Scale Technicolor at the Tevatron,” *Phys. Lett. B* **388** 803 (1996), hep-ph/9607213.

²K. Lane, “Technicolor Signatures— Ieri, Oggi E Domani,” hep-ph/0006143 (July 2000). This reference has compiled several searches for technicolor and is also a good summary of technicolor phenomenology that is within observational range of current and near-future experiments.

1 INTRODUCTION

Historically, mass has been an entirely empirical concept. It is a quantity that must be *measured* either directly or indirectly. It determines the gravitational pull between two bodies. In classical mechanics it is an essential part of Newton's second law

$$\vec{F} = M \vec{a}, \quad (1.1)$$

where \vec{F} is the applied force on a body of mass, M , and \vec{a} is the resulting acceleration. One way to measure an unknown mass using Equation 1.1 is to use the acceleration, a_{std} , produced by a standard force onto a standard mass; then the unknown mass may be computed *relative* to the standard mass by its acceleration, a_{unk} , under the standard force. *i.e.*

$$M_{unk} = M_{std} \frac{a_{std}}{a_{unk}}. \quad (1.2)$$

In other words, we only know the mass of a given object by comparison with an arbitrary standard. It is not yet understood from first principles. Mass is also present in other relationships. For example, in the theory of relativity, mass is equivalent to energy as shown by the equation

$$E = Mc^2, \quad (1.3)$$

where c is the speed of light (299,792,458 meters/second). This fact allows high-energy physicists to specify mass in units of energy, where the favorite unit of mass is the GeV or giga-electron volt (in units of $c = 1$). In addition, objects which have zero mass (photons for instance) travel at the speed of light, and objects which have a non-zero mass must travel less than the speed of light. In the theory of general relativity, mass is postulated to produce curvature in local space-time. This curvature causes light to bend in the vicinity of a massive body, local time intervals to dilate, and is also the mechanism behind the gravitational force. Mass also plays an important role in quantum field theory which describes the

motions and interactions of particles.

In the standard model, particle masses are generated by postulating the Higgs mechanism. Without the Higgs mechanism, the gauge bosons described by the local gauge-invariant Lagrangian density must be massless. This is fine for interactions involving the photons of the electromagnetic force and the gluons of the strong force. However, the W^\pm and Z^0 particles of the weak interaction are very massive, where $M(W^\pm) = 80.42 \text{ GeV}$, and $M(Z^0) = 91.19 \text{ GeV}$ [1]. For comparison, recall that the mass of the proton is 0.938 GeV ! The Higgs mechanism starts with the original local gauge symmetry which generated the mathematical form $(SU(2)_L)$ of the weak interaction. The “off center” ground state (or vacuum) of the Higgs potential breaks the local gauge symmetry. The new free fields are best expanded about the new minimum to facilitate the use of perturbation theory to perform calculations. With the correct “gauge rotation” chosen, the masses of the weak vector bosons, the W^\pm and Z^0 , become apparent. A Higgs particle (spin-0, therefore a boson) is also predicted by this construction, and the coupling of the new Higgs boson to the quarks and leptons of the standard model allows them to also have mass [2, 3].

The nature of the scalar field that is the basis of the Higgs mechanism is not known. It must have the same quantum numbers as the vacuum, however, but it could also be composite – made of more fundamental particles that add up to give a scalar. This analysis searches for particles that may implicate a new force, called technicolor. Technicolor may be the cause of the Higgs mechanism. The idea of technicolor is inspired by chiral symmetry breaking in QCD. At low temperature, the ground state, or vacuum, of quantum chromodynamics (QCD) must have no charge, no net angular momentum (spin), and no momentum. In order to accomplish this with fundamental spin-1/2 particles (quarks), particles of opposite spin, charge and momentum forms this vacuum “condensate,” which necessarily leave a net handedness. This non-zero chirality of the vacuum is what creates a potential like the Higgs potential mentioned above. Hence, technicolor begins with a chiral symmetry of *techniquarks* and *technileptons*, where the techniquarks fall under a higher-scale version of the strong force. Hence, chiral symmetry breaking by bound states of techniquarks is the mechanism behind electroweak symmetry breaking [4, 5, 6].

2 THE STANDARD MODEL

In 1979, Sheldon Glashow, Steven Weinberg, and Abdus Salam received the Nobel Prize in physics for the discovery of what is known today as the “3 – 2 – 1” standard model. This was the culmination of several decades of work from these individuals, and many colleagues. The standard model (SM) is a quantum field theory that describes how the known particles interact via three of the four forces in nature: electromagnetism and the weak and strong forces [7, 3]. It is not currently known how to incorporate the gravitational interaction to obtain a single field theory.

There are three major components of the standard model:

1. The known spectrum of fundamental particles: quarks, leptons, and mediators.
2. The mathematics and the set of assumed underlying ideas that include the following:
 - Lorentz invariance
 - Quantum mechanics with 1st and 2nd quantization, where 1st quantization introduces the commutation rules for canonical variables such as momentum and position. Second quantization introduces commutation (anti-commutation) rules for boson (fermion) creation and annihilation operators.
 - Noether’s theorem: Given a symmetry, there is a corresponding conserved quantity. These conserved quantities include energy, momentum, angular momentum, charge, spin, etc.
 - The principle of least action
 - Unitarity. When all final states are taken into account, the total probability of those states is 1.
 - Any new force is described by introducing a local gauge (or phase) invariant group. “Rotations” in this group correspond to new conserved currents. For a given $SU(N)$ group of dimension N , there are $N^2 - 1$ independent generators of rotation. Each of these generators is paired with a massless mediating particle, which communicates the interaction between particles.

- Simplicity: Use the *minimum* structure needed to describe known phenomena. For instance, quantum numbers not known to be correlated (such as color and charge) are designed to commute, by construction.
- Spontaneous symmetry breaking. Nature is seen to select a vacuum (ground state), which is not invariant under $SU(2)_L$ transformations, which is a symmetry of the weak force. The Higgs mechanism breaks this symmetry and provides for the masses of the W^\pm and Z^0 vector bosons. In addition, fermion masses are allowed and a new particle, the Higgs boson, is generated.

3. The specific group structure: $SU(3)_C \otimes SU(2)_L \otimes U(1)_Y$

- $SU(3)_C$ is the group which represents the structure of the color (strong) interaction. The quantum number of this group is the color-state which takes on the values of *red*, *green*, or *blue*. The eight massless gluons are the mediators of the color force.
- $SU(2)_L$ represents the left-handed “sector” of the electroweak force. The conserved quantum number is the weak isospin, I , with the particular component of that isospin, I_3 . The word “isospin” is chosen to strike the analogy with spin, which is also an $SU(2)$ quantum number. For example, left-handed electrons have a weak isospin of $-1/2$ and its associated electron-neutrino $+1/2$. Right-handed particles are weak isospin singlets ($I = 0$). The W^\pm and Z^0 bosons are the mediators of this sector.
- $U(1)_Y$, where $Y = 2(Q - I_3)$ is the weak hypercharge. This is chosen instead of just the particle charge, Q , in order to separate out the left-handed ($V - A$) sector. This separation is a result of parity violation in weak decays (right-handed neutrinos have not been observed). The photon, along with the $U(1)$ component of the Z^0 are the mediators. At low energies, $E \ll M_Z$, this reduces to the electromagnetic force.

Within the standard model framework, the electromagnetic force, mediated by the photon, propagates light, and the electric and magnetic forces. The photon is a quantum of energy and one unit of spin (angular momentum), and is therefore a boson. It does not carry an electric charge. As a result, the photon, to first order, does not interact directly with other photons. The photon is also massless. Hence, the electromagnetic potential between charged particles is long range and is inversely proportional to the distance between them ($\sim 1/r$).

The weak force, now unified with electromagnetism, is seen experimentally in the decays of long-lived particles. One example of this is β decay seen in nuclear physics experiments, such as the decay

of the neutron, $n \rightarrow p e^- \bar{\nu}_e$, or the long lifetime of particles, such as the charged pion which decays via $\pi^\pm \rightarrow W^\pm \rightarrow \mu \nu_\mu$. The mediators for this force are the W^\pm and Z^0 particles. The weak force is comparable in strength with the electromagnetic force at high energies. Otherwise, the weak force is associated with relatively rare processes, since the weak gauge bosons are quite heavy. In fact, due to their masses, they were not discovered directly until the early 1980's. Due to the masses of the weak vector bosons, the potential of the weak force is proportional to $\sim e^{-\mu r}/r$.

The strong force is the strongest force currently known. It governs the interactions between quarks, and ultimately holds atomic nuclei together. The extraordinary density of a typical nucleus (15 orders of magnitude more dense than normal matter) is a testament to the very high binding energy created by the strong force. The gauge bosons mediating this force are called gluons, and they carry their own version of charge, called color, of which there are three: red, green and blue. Gluons carry a net color charge allowing them to couple and exchange color with other gluons. Mathematically, this is a consequence of the *non-abelian* (or non-commuting) generators of the color- $SU(3)$ local gauge symmetry group. There are eight independent generators of this group, corresponding to eight gluons, each possessing different color-anticolor combinations. Also, gluons are massless and thus readily created. These facts, combined with the interplay between the number of colors (3) and the number of quarks (6) means that the potential between two quarks *increases linearly* with distance. At least qualitatively, these ideas suggest that quarks are confined to colorless bound states of $q\bar{q}$ (mesons) or to $q_{red}q_{green}q_{blue}$ (baryons). This remarkable theory of strong interactions describes a very broad range of measurements, and is consistent with the spectrum of mesons and baryons and with the existence of quark and gluon “jets” seen in high-energy physics experiments today.

The current standard model has been successful in describing the many phenomena of the known particles. However, the standard model is not complete. Contained within it is the Higgs mechanism, which is put in by hand in order to generate the masses of the W^\pm and Z^0 bosons and to break electroweak symmetry. The Higgs field may be thought of as a “place holder” used to parameterize electroweak symmetry breaking. The Higgs mechanism is likely to be a product of a deeper symmetry, however.

3 TECHNICOLOR THEORY

Technicolor was introduced by Weinberg & Susskind in 1979 to explain Electro-Weak Symmetry Breaking (EWSB) [8]. The symmetry breaking scheme in technicolor involves a QCD-like force which operates at or below the EWSB scale. The symmetry-breaking occurs in the breaking of chiral symmetry in the technicolor $SU(N_{TC})_L \otimes SU(N_{TC})_R$ Lagrangian, where N_{TC} is the number of technicolors. This chiral symmetry breaking is analogous to that found in QCD, where the vacuum ($q\bar{q}$ “condensates”) has a non-zero chirality due to conservation of spin (that must be zero), and momentum (also zero for the vacuum). In technicolor, techni-pions are the goldstone bosons that take the place of fundamental scalars. For example, the longitudinal components of the W^\pm and Z^0 bosons (which allow them to have mass) are techni-pions in the technicolor theory. Furthermore, gauge bosons in the extended technicolor (ETC) theory give mass to the standard model (SM) fermions. This happens through a Higgs-like coupling (via ETC gauge bosons) between technifermions and quarks/leptons of the standard model. Extended technicolor is a gauge field theory, which itself breaks to technicolor, color, and electro-weak symmetries [5, 6].

The original technicolor concept needed modifications to explain developments in known phenomenology, including better limits on flavor changing neutral currents (FCNC), and the discovery of the high mass of the top quark. This modification involved a “walking” coupling constant, where the coupling changes more slowly as a function of Q^2 than does the “running” of α_s . The large mass of the top quark requires a symmetry in addition to extended technicolor to give the known mass, since ETC cannot do this by itself. This additional symmetry is called top-color, and only operates on the third quark and lepton family.

This analysis searches for evidence of a technicolor model put forth by Eichten, Lane, and Womersley in 1997 [5], and updated in 1999 [6]. This model is only available in the PYTHIA high-energy physics event generator [14]. We search for the lightest technimesons via $\omega_T/\rho_T^0 \rightarrow \gamma \pi_T/\pi_T' \rightarrow \gamma b\bar{b}$, where the masses of π_T and ω_T/ρ_T^0 are allowed to vary in 20 GeV intervals on a “mass plane.” Figure 3.1 shows the leading order (LO) diagram for producing ω_T/ρ_T^0 assuming that only the indicated diagram contributes

significantly to the scattering cross-section. Because the ω_T and ρ_T^0 are considered to be degenerate and not distinguishable in this analysis, the symbol, ω_T , is used to discuss the mass eigenstate. Similarly, the π_T is degenerate with the π'_T , so unless the states need to be distinguished, they will be referred to as π_T . The π'_T , which contains a gg decay mode, was left out of the original version of PYTHIA.

Within the framework of technicolor, the longitudinal components (or polarization) of the massive vector-bosons, Z_L^0 and W_L^\pm , are considered to be techni-pions. Recall that the existence of a longitudinal (helicity of zero) polarization implies a rest frame for the particle. This, in turn, means that the W_L^\pm and Z_L^0 must each have non-zero mass, since only massive particles have a rest frame in the theory of special relativity.

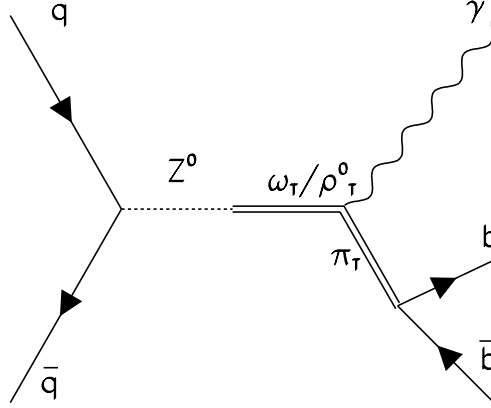


Figure 3.1 Leading-Order (LO) diagram for Techni-Omega production. In this case, the Z^0 or γ may be produced “off mass shell” and thus can mix with the ω_T/ρ_T^0 , since the quantum numbers ($S = 1, Q = 0$, color singlet, etc.) are the same.

The ETC gauge bosons couple most strongly between techni-fermions and the most massive standard model (SM) fermions. Therefore, the preferred π_T decay is to $b\bar{b}$ (for π_T mass below the $t\bar{t}$ threshold). As a result, a search for technicolor is done by examining data taken at the DØ experiment for excess $\gamma b\bar{b}$ events. Appendix B discusses other searches for technicolor at collider experiments.

4 THE DØ EXPERIMENT: A COLLIDER DETECTOR

Introduction

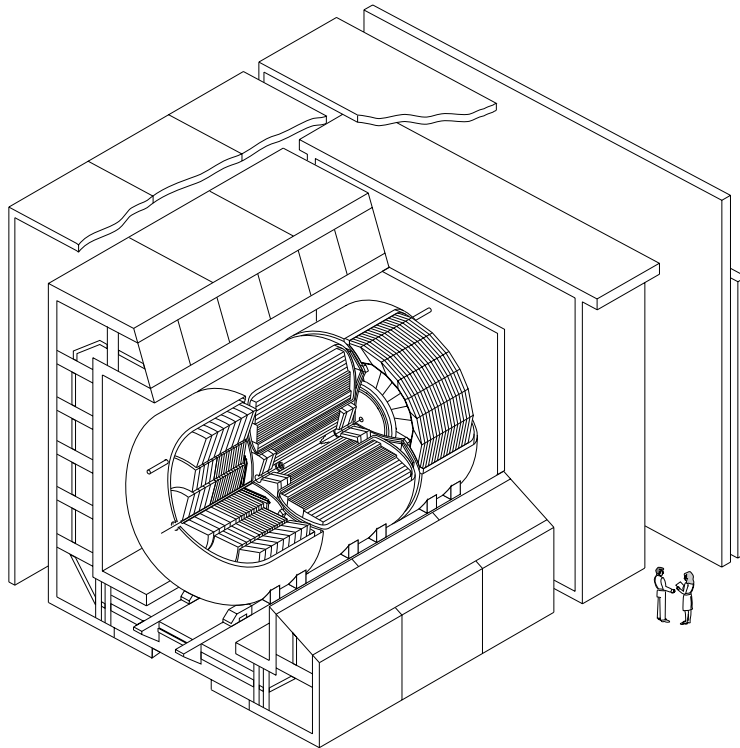
There are two major ways that experimentalists study high energy phenomena in nature. The first method involves collecting data on incoming particles from outer space with either space or earth-based particle detectors. Typically, these experiments measure the direction, energy, and identity of the incoming high-energy particles in order to tie them to a specific source and to infer its properties. The focus and interest of these measurements is more on the possible source (such as active galactic nuclei (AGN), decays of super-massive remnants of the big-bang, topological defects, etc.) that create the incoming particles, and on the transport mechanisms of those particles through intergalactic or interstellar space, rather than on probing their interactions with matter at the fundamental level. Depending on the type, these particle fluxes come from all directions in the sky, and at energies up to 4×10^{21} eV, with this highest energy having a flux on the order of $\sim 1/\text{year}$ onto a typical cosmic ray detector such as Fly's Eye [9]. Because the positions and angles of the incoming particles are not initially known, these detectors typically must have a very large collection area (or volume) in order to detect enough events to do a given measurement. The dimensions of these detectors range from meters to kilometers [10].

The second major way of studying high-energy phenomena involves directing a high-energy beam of particles onto a fixed target, or at an oppositely directed beam of particles. A particle detector is strategically placed to be able to record large amounts of data on the ensuing interactions between beam and target matter. These detectors are able to make very detailed and precise measurements of interactions because the intensity (or luminosity) and energy of the beam are typically well-known, and the position of the interaction point is usually known to within a few cm, mm or perhaps even microns. Thus, a very large amount of detection equipment may be trained on what happens in a small volume of space. With the luminosities available today combined with current data-handling technologies, billions of events may be used to make a given measurement. This allows physicists to study the inner workings of matter to a distance scale roughly inverse to the energy of the beam, and sometimes much smaller,

depending on the natural sensitivity of the measured quantity.

There are two major types of particle experiments operating today that use high-energy beams, colloquially referred to as “fixed target” and “collider” experiments. The fixed target detectors are such that the incoming particle beam is directed into either a solid, liquid, or gas at rest in the laboratory. Thus, the center-of-mass energy $E_{CM} \approx \sqrt{2E_{beam}M_{rest}}$ is the amount of usable energy available for illuminating the experimenters’ favorite problem, where M_{rest} is the mass of the stationary target particle. The products of the interaction shower forward in the direction of the beam, so the typical geometry of the fixed-target detector has the detection equipment downstream from the interaction point (IP). The only real disadvantage to the fixed-target technique is that, due to the conservation of momentum, the usable energy for a hard interaction is somewhat less than the energy of the incoming beam. Therefore, most fixed-target programs today are designed to make measurements that would not be practical for a 4π collider detector, or if the masses of the target and beam particles differ significantly. For instance, the NuTeV [11] detector at Fermilab is a fixed target system which facilitates measurements of neutrino-nucleon scattering by incorporating a secondary ν_μ beam (decayed from a π^+ or a π^- beam). Since the neutrino usually needs to traverse a large amount of material before interacting, detailed neutrino measurements are possible only in the fixed-target scenario.

The collider detector is the other major type of detector incorporated in high-energy physics, and it uses colliding particle beams, a major jump in the technology of beams. Collider detectors are considered to be the most versatile due to the energy available ($E_{CM} = 2E_{beam}$) to study the interactions, and the variety of interactions that may take place and be studied. The basic geometry of the collider detector is cylindrical where the beampipe defines the axis of the cylinder, and the expected IP is within several centimeters (longitudinally) from the detector center inside and along the beampipe. Perpendicular to the beam axis, the IP is usually known to within millimeters or microns. Bunches of particles from two independent beams are directed headlong into each other to collide as close to the center of the detector as possible. If the beam particles are of equal mass, then the center-of-mass energy available for a hard interaction is the sum of the incoming beam energies in the lab frame. In that case, the center-of-mass frame is at rest in the laboratory, and a hard scattering event will shower in all directions from the IP, so collider detectors must have as close to 4π coverage as possible in order to be able to fully reconstruct the event, where “reconstruct” means to determine the *identities* and *momenta* of all of the products of the hard-scattering event, not counting the spectator interactions. One such detector operating today is the DØ experiment, shown in Figure 4.1, located at Fermi National Accelerator Laboratory in Batavia, Illinois.



DØ Detector

Figure 4.1 The DØ detector. Shown are the central tracking, the calorimeter and muon systems. The beam enters both sides of the detector along the cylindrical axis. The pipe which is offset from the center is the beam-pipe for the main-ring. The Main Ring is the preaccelerator for the Tevatron, and for historic reasons only clears the Tevatron by about 90 inches at the DØ interaction region.

The DØ Experiment

The DØ (or Dzero) experiment is a premier colliding-beam experiment in the field of particle physics. It is served by oppositely directed beams of protons and anti-protons made to collide at or near the center of the experiment. The main service beam at Fermilab, called the Tevatron, is the device which delivers the counter-rotating beams of protons and anti-protons to the collider experiments. A similar experiment, called Collider Detector at Fermilab (CDF) is the other collider detector using the Fermilab Tevatron.

The DØ detector is currently being upgraded for Run II at the Tevatron, and has begun taking data as of April 2001. This upgrade has entailed rebuilding the tracking system and muon systems, and

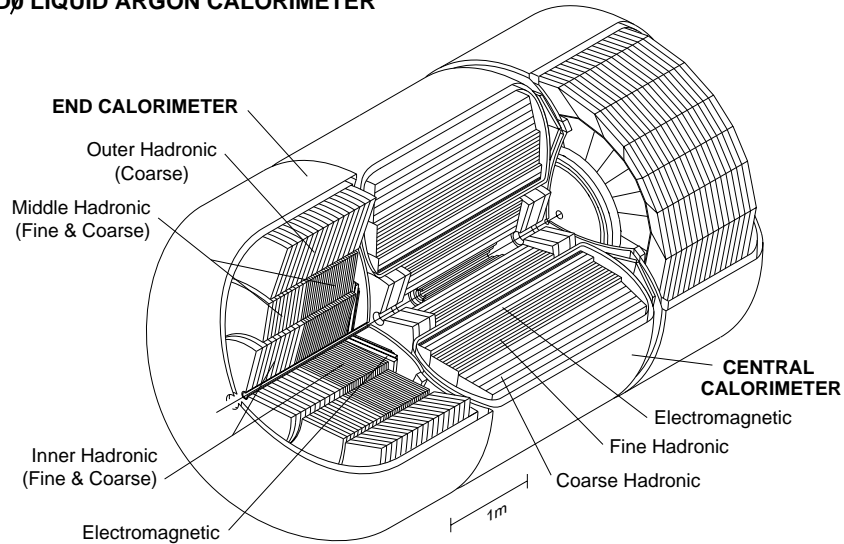
DØ LIQUID ARGON CALORIMETER

Figure 4.2 The DØ calorimeter system detail.

upgrading the electronics to handle a much higher luminosity from the Tevatron. However, since the data taken for this thesis was during Run I (from 1992-1996), the Run I version of the DØ experiment will be described.

The Run I version of the DØ experiment [12] consists of several subsystems, starting from the center and working radially outwards:

- Central Vertex detector
- Central tracking
- Forward tracking
- Transition Radiation detector
- “Level 0” hard-interaction detector
- Calorimeter (Central (CC), and Forward(EC)):

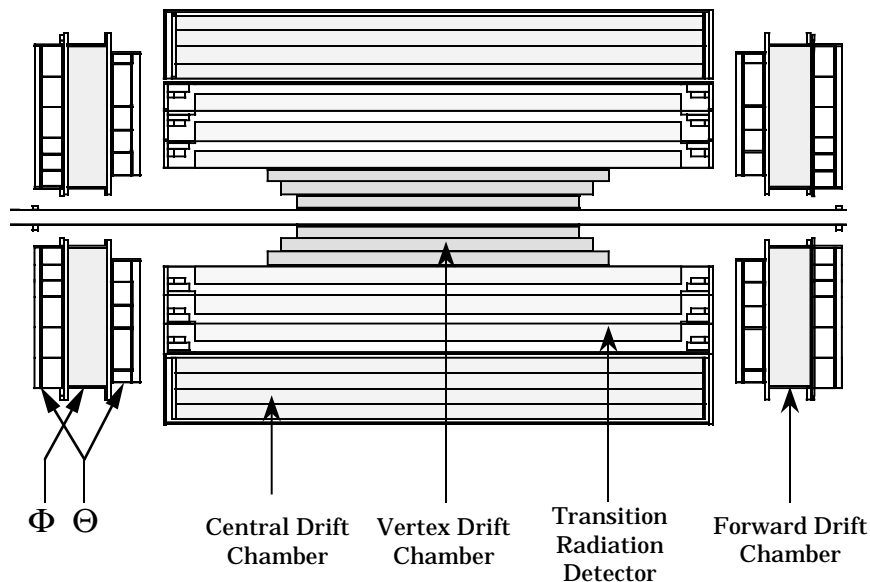


Figure 4.3 The DØ central tracking system detail.

- Electromagnetic (Central and Forward)
- Fine hadronic
- Coarse hadronic
- Inter-cyrostat detector (ICD)
- Muon detector

As a whole, the DØ detector is arranged in a roughly cylindrical manner around the Tevatron beam pipe. The beam pipe is beryllium, and its relatively low number of interaction lengths keeps interactions between the outgoing particles and the pipe material to a minimum. The hollow beam pipe has a diameter of ~ 3 cm. To further reduce interactions between final state particles and the beam-pipe, the beam-pipe material is made to be much thinner inside the detector than in the rest of the Tevatron accelerator complex.

The three major systems in the DØ detector are the tracking, calorimeter, and muon systems. We want to non-destructively obtain the charged tracking information of the original particles coming from the IP before they interact with very much material; therefore, the tracking system is closest to the beampipe. This system, shown in Figure 4.3, is a 1m-radius cylinder of wire chambers and a transition radiation detector. All of this is surrounded by the hermetically sealed liquid-argon sampling calorimeter. Like the calorimeter, the tracking system is also on the ends of the detector, to give

approximately 4π coverage, except for the narrow region along the beampipe at $|\eta| > 4.5$ (an angle of $\theta < 0.022$ radians). The vertex tracking system (VTX) is the most central sub-system and occupies a space of a little less than $1m$ in radius from the beam, and about $3.5m$ longitudinally. In order to reconstruct a $p\bar{p}$ event, the position of the primary hard interaction (or “vertex”) between the proton and anti-proton beams needs to be determined. The VTX detector also contains tracking information to assist in particle identification, since charged particles leaving the interaction point (IP) can be detected.

After the VTX, going radially outwards from the beam-pipe is the Transition Radiation Detector (TRD). The TRD is mostly used to distinguish between electrons and pions by using the corresponding X-ray light produced in the TRD when the particle in question crosses a material boundary (within the TRD). Since this analysis focuses on photon identification, the TRD is not used in the event classification.

Further outward, the Central Drift Chamber (CDC) is used to detect particle tracks outside of the TRD, and is arranged in a cylindrical fashion as well. The CDC uses wire chambers with the wires arranged axially with the z-axis of the detector. The Forward Drift Chambers (FDC) are North and South end counterparts to the CDC. For each end of the detector, the FDC has three layers. The one closest to the center has wires which run around the beam pipe in four straight-line segments to measure the $r - \theta$ of the charged particle. The middle one has wires that run radially to measure ϕ . The outermost layer complements the first layer by being rotated 45° to improve resolution and eliminate left-right ambiguities.

Further out in r is the calorimeter, shown in Figure 4.2, which is the primary energy-measuring device of DØ. In general, particles that can be absorbed by the calorimeter material may have their energies measured. These mostly include photons, electrons and jets (hadrons). The calorimeter system consists of three completely separate volumes for ease of access to the tracking system and TRD. Those sections are the central calorimeter (CC), and two end calorimeters (EC). To differentiate between the two ends, the naming convention EC North (ECN), and EC South (ECS) is used. Each of the three sections of the calorimeter are contained in large steel cylindrical containers for the ends, and a long cylinder with the 1 m center removed to leave room for the tracking system, resulting in a donut-shape. Inside the containers is the liquid argon-filled sampling calorimeter. Generically, the unit cell of this type of calorimeter is one layer of absorber material such as steel, copper, or uranium, followed by an active detector region that measures charged particles showering from the absorbing material. An effective calorimeter is designed with many of these cells deep as well as wide, so as to be able to record

total energy as well as positional information of the original incoming particle. Eventually, this system is calibrated using beams of known energy and identity, combined with detailed computer simulations.

Finally, the muon system is located furthest radius from the beam pipe, and therefore is at the interaction point. This system uses a series of three cubical wire-chamber shells to detect the charged muon. The energy is measured by placing a ~ 2 Tesla iron toroid magnet between layers 1 and 2. The amount of bend in the path of the muon determines its momentum. Any muons that are produced in the event will leave a minimum-ionizing trail in the calorimeter, but will not shower for two major reasons: the energy loss due to bremsstrahlung is relatively low because it is proportional to the inverse square of the mass of the muon, and ionization loss is inverse to the mass to the first power [13]. Additionally, the muon is long-lived (2.2×10^{-6} s, corresponding to $c\tau = 660$ m.). It is therefore useful to place any muon detection equipment outside of the calorimeter, since nearly anything exiting the detector from the IP would be a muon. Tau particles decay too quickly (usually in the tracking region) to have a similar effect. Hence, the vast majority of outgoing particles from the detector will be muons. Since muons are charged, the muon system uses a bending magnet in between layers of wire chambers in order to detect and measure the energy of outgoing muons. No attempt is made to absorb the muon energy. Therefore, except for the narrow angular region along the beam-pipe, muons, and weakly-interacting neutral particles, the energy of an event is contained within the confines of the DØ detector.

The Level Ø (LØ) detector “wakes up” the electronics to possibly record the event. It consists of an arrangement of hodoscopes on both the north and south ends of the calorimeter system. This detector is most likely to fire when a hard interaction occurs. A hard interaction is one in which the momentum exchange between p or \bar{p} beams is some reasonable percentage ($\sim 1\%$ or higher) of the total beam momentum. Most of the time, elastic or diffractive interactions do not fire the Level Ø detector. For most interesting events, both N and S ends of the LØ will show a signal.

DØ Coordinate System and Transverse Energy

Coordinates are needed to specify the locations of objects in the DØ detector. The standard polar coordinates used are ϕ , θ , and z . The z -axis is defined to be along the beam direction, with $+z$ along the proton direction, and $-z$ along the anti-proton beam. The z coordinate is most often used to specify the location of the event vertex – the location of the $p\bar{p}$ interaction within the detector. The ϕ -coordinate is an angle defined using the right-hand rule (with the thumb pointed in the direction of the $+z$ axis) to be the azimuth of a location “around” the beam direction. The scattering angle, θ ,

from the $+z$ direction is more often expressed in terms of the pseudo-rapidity:

$$\eta = -\ln \tan \frac{\theta}{2} \quad (4.1)$$

Cartesian coordinates (x, y, z) are also used, and are defined in the right-hand sense as well. x and y are the coordinates perpendicular to the z -axis.

The concept of *transverse energy* is very important in high-energy physics because before collision, the beam starts out with zero total transverse energy or E_T , defined to be

$$E_T = E \sin \theta. \quad (4.2)$$

Momentum is conserved, so after a hard collision, when two objects are “back to back” in the detector, and there is very little else showing in the detector, one may conclude that the transverse energies of those objects are equal. E_T is also useful when discussing neutrinos, which do not interact with the detector. When large amounts of “missing E_T ” (or \cancel{E}_T) are seen by taking the vector sum in the x, y plane,

$$\vec{\cancel{E}}_T = - \sum_i \vec{E}_{T_i}, \quad (4.3)$$

where \vec{E}_{T_i} is the E_T of every cell in the calorimeter, we may conclude that a neutrino was produced by the event, or that the calorimeter energies for the event were mis-measured. Events with high transverse-energy objects indicate a large momentum exchange between the proton and antiproton. This is a very important indicator of a “hard” (or interesting) event.

Data Aquisition

During Run I, there are $\sim 300,000$ $p\bar{p}$ crossings per second. However, the events of interest happen much less frequently. This, combined with limitations in storage speed means that the data aquisition system (DAQ) must be able to sift through this high rate in order to finally write about 2 events per second to tape, technically feasible at the time the DAQ was built in the early 1990’s. To accomplish this, a three-level triggering system is used at DØ. They are the level 0 (LØ), level 1 (L1), and level 2 (L2) triggers. Due to the tradeoff between speed and complexity, the LØ and L1 triggers are hardware-based, where the L2 system uses software to make the final selection.

L0 makes the initial decision to keep an event by detecting particles scattered significantly away from the beam-pipe indicating a hard interaction. The number of events per second accepted is now $\sim 100,000$. After L0, L1 requires a variety of thresholds on the events such as the E_T of a calorimeter tower, calorimeter imbalance in E_T or missing E_T (\cancel{E}_T), or muon E_T . These thresholds are used together to look for events with a particular physics interest in mind. This leaves the event rate down to ~ 100 Hz. Finally, L2 uses software to do a fast event reconstruction to identify candidate physics objects such as jets, photons, and electrons. Threshold and fiducial requirements are placed on these objects to decide on keeping an event.

Various physics working groups make many different L1 and L2 triggers depending on the kinds of events that are of interest to them. Many triggers run simultaneously (trigger “packages”) as part of the DAQ to find events of interest for all of the physics groups.

Luminosity

The instantaneous luminosity is the number of $p\bar{p}$ crossings per unit area per unit time. This quantity is purely a function of the quality of the Tevatron beam, which runs through the middle of the D0 experiment. Two major properties result in high luminosity: beam diameter and particle intensity. The beam diameter is an effective diameter of the intersection of the proton and anti-proton beams near the interaction region of the detector. Since \bar{p} 's are difficult to produce, one of the limitations to luminosity is the number of \bar{p} 's in the beam.

The integrated luminosity is the number of crossings per unit area over a given running period. Since this is an inverse area, it is conveniently expressed in units of inverse-picobarns (pb^{-1}). Hence, the number of events expected from a given physics process having a cross-section σ is

$$N = L \cdot \sigma, \tag{4.4}$$

where L is the integrated luminosity and is the principal normalization factor used in an analysis. Since not all triggers are on at the same time, different triggers have different luminosity “exposure.” This is accounted for by recording the triggers and instantaneous luminosity in effect in each data-run, and keeping a database of that information.

5 OVERVIEW OF THE SEARCH

This analysis looks for high-energy physics events that are predicted by the theory of extended technicolor. These predicted events are in the $\gamma b\bar{b}$ channel. Unfortunately this signal is *not* unique. The standard model predicts $\gamma b\bar{b}$ via the leading order diagrams shown in Figure 5.1, where the outgoing quark or gluon fragment to produce additional (heavy) jets. In the left-hand diagram, the b -quark is produced by gluon splitting, and in the right-hand diagram by QCD bremsstrahlung, and sea-quark content of b -quarks in the proton or anti-proton.

In addition, the cross-section for three or more jets is very high, and there are many cases when a jet “fakes” a photon. For example, jets copiously produce π^0 's, which decay via $\pi^0 \rightarrow \gamma\gamma$. The π^0 is very short-lived, leaves no charged track in the detector, and if it is high energy, it may be impossible to tell the two photons apart. This can register rather easily as a single high-energy photon. To counter jet backgrounds, standard DØ γ -ID cuts are applied [17, 19]. Jets still fake photons, but the rate is much lower with the additional γ -ID cuts. A detailed description of the background calculation is in Chapter 7.

An essential task to any analysis is to maximally reduce the number of background events while keeping signal events. For example, an excess of 20 events above a background of 1000 is considered negligible, since the Poisson distribution on 1000 events may easily fluctuate between 900 and 1100 ($1000 \pm \sqrt{1000}$). One criterion that may be used is the value of S/\sqrt{B} , where S is the expected number of signal events, and B is the expected background. Hence, in this case $S/\sqrt{B} = 0.2$. If the selection of the data is “smarter” – *i.e.*, it is tuned to the differences between signal and background—then we can reduce those background events while maintaining a high signal acceptance, and the new numbers might be 15 signal and 3 background, yielding $S/\sqrt{B} = 8.7$! Now, we are well on the way to the discovery of a new phenomenon. If there is an excess of data events, then the number of standard deviations is computed. Several standard deviations would indicate the potential for a discovery. If this is not the case, then we calculate an upper limit on the cross-section of the predicted process. In order to yield the most powerful search along with the lowest possible cross-section limits, we use several observables as

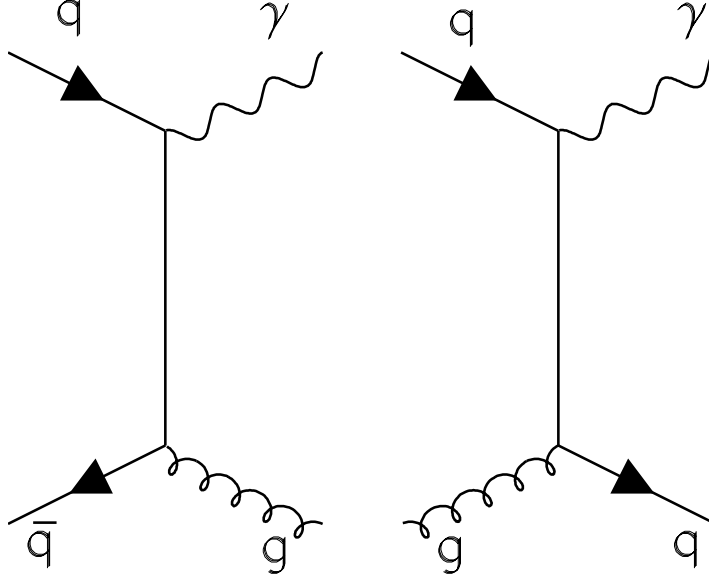


Figure 5.1 Leading Order Feynman diagrams for single direct photon production: one of the ways that $\gamma b\bar{b}$ gets produced. Initial state quarks and gluons are on the left side of each diagram; final state particles are on the right side.

inputs to a neural network program, called JETNET [26] to quantify the difference between technicolor and background events.

Physics Variables

Technicolor events and background events must be distinguished from one another in a quantitative way. To begin with, the ω_T and π_T are expected to be quite massive and to produce resonance peaks. In contrast, background events have a more even distribution in mass. Hence, mass variables are used that correspond to the ω_T and π_T . These are $M(\gamma, jets)$ and $M(jets)$ respectively. Approximately 40 other physics variables were considered for technicolor vs. background discrimination properties. Figures 5.2-5.4 contain plots showing examples of technicolor signal superimposed on background for each variable, listed and defined below in order of importance:

- $M(\gamma, jets) = \sqrt{(\sum_i^{\gamma, jets} E_i)^2 - (\sum_i^{\gamma, jets} \vec{P}_i)^2}$. This quantity corresponds to the mass of the ω_T .
- $M(jets) = \sqrt{(\sum_i^{jets} E_i)^2 - (\sum_i^{jets} \vec{P}_i)^2}$. This is the mass of the π_T when evaluated on technicolor events.

- $(M(\gamma, jets) - M(jets))/M(\gamma, jets)$. The “reduced mass difference” peaks very sharply for technicolor events, but is very broad for background events.
- Dijet opening angle $\Delta R_{jj} = \sqrt{(\phi_{j1} - \phi_{j2})^2 + (\eta_{j1} - \eta_{j2})^2}$. This is sensitive to the mass of the technipion, and is more peaked for technicolor events than for background events. Similarly, the opening angles between all leading objects $\Delta R_{\gamma jet_i}, \Delta R_{jet_i jet_j}$ were considered.
- Dijet opening ϕ -angle $\Delta\phi = |\phi_{j1} - \phi_{j2}|$. Again, this is also sensitive to the relatively massive π_T . In addition, the opening angles $\Delta\phi_{\gamma jet_i}$, and $\Delta\phi_{jet_i jet_j}$ were also considered.
- E_T^γ . Photon transverse energy. The photon emitted from the decay of the ω_T has a large transverse energy.
- E_T^{j1}, E_T^{j2} . These are the transverse energies of the highest E_T jets in the event.
- η^j, η^γ . The pseudo-rapidity of the jets and photon is similar to the scattering angle and is defined to be $\eta = -\ln \tan \theta/2$.
- $M(\gamma, jets) - M(jets)$. The mass difference is also a strong peak for technicolor events.
- Two-body mass combinations, $M(\gamma, j1), M(\gamma, j2), M(\gamma, j3), M(j1, j3), M(j2, j3)$
- $S_T = \sum_i^{all} E_T$. The sum of the transverse energies of all of the jets, the photon, and the muon in the event.
- $H_T = \sum^{jets} E_T$. The sum of the transverse energies of the jets in the event.
- E_T^{j1}/H_T . The ratio of the leading jet E_T to the sum of the jet E_T 's.
- \cancel{E}_T . Missing transverse energy of the event.
- N_{jet} . The jet multiplicity is the number of jets produced in the event.
- Aplanarity and Sphericity: These indicate the momentum flow of the event and are event shape variables. They are computed by diagonalizing the momentum tensor $M_{ab} = \sum_j^{N_{jets}} p_{ja} p_{jb} / \sum_j^{N_{jets}} p_j^2$ where a, b run over the x, y , and z momentum components and j is the jet index. The eigenvalues are Q_1, Q_2 , and Q_3 . Aplanarity is defined $A = \frac{3}{2}Q_1$, and Sphericity is defined $S = \frac{3}{2}(Q_1 + Q_2)$. These variables were inspired by the top quark search in the $t\bar{t} \rightarrow jets$ channel.

Many of the above quantities provide at least some level of discrimination. At the start of the selection process, the above variables were plotted and qualitatively evaluated for their individual discrimination properties. As seen in Figures 5.2-5.4, there are several candidates that show promise.

To maximize the discrimination power of many variables simultaneously, we employ neural networks. However, there is redundancy between many of the variables listed above, and some yield less discrimination than others. Hence, a small complementary subset was selected after trying many different variable combinations in a neural network. This following five were found to be the most effective combination:

1. $(M(\gamma, jets) - M(jets)) / M(\gamma, jets)$
2. $M(jets)$
3. E_T^γ
4. $\Delta R_{jj} = \sqrt{(\phi_{j1} - \phi_{j2})^2 + (\eta_{j1} - \eta_{j2})^2}$
5. S_T

Search outline

The remaining chapters describe in detail the search for ω_T at the DØ experiment. Below is a schematic outline of this search program.

1. **Filter Run 1 DØ data** to extract $\gamma b\bar{b}$ candidate events. This includes kinematic cuts, photon identification, and b-jet identification by identifying a μ close to the jet in the decay $b \rightarrow X\mu\nu_\mu$.
2. **Derive the “tag-rate”** function to be used to compute the background. This function re-weights non b -tagged events to reproduce the spectra of b -tagged events.
3. **Generate technicolor** events and cross-sections using PYTHIA v6.126 and GEANT detector simulation for the events. Use standard reconstruction software, DØRECO, to put the events into a usable form. Apply the event selection criteria to these Monte Carlo events. Because the masses of the ω_T and the π_T are unknown, the search is performed by varying the two masses over a 2-dimensional grid at roughly 20 GeV interval. Each combination of masses is a separate search. This analysis evaluates thirty-two such “mass points,” ranging over $140 < M(\omega_T) < 300$ GeV and $40 < M(\pi_T) < 140$ GeV.

4. **Compute corrections** to the technicolor acceptance due to aspects of $p\bar{p}$ interactions not simulated by GEANT.
5. **Create training samples** used to train neural networks. These samples are from data and signal Monte Carlo events (generated by PYTHIA) using the selection cuts for this analysis, but without the b-tag requirement. Since the neural network inputs (physics variables) depend on the masses given to the technicolor Monte Carlo, a different neural network is trained on each mass point.
6. **Train neural networks** for each of the 32 combinations of ω_T , and π_T^0 mass generated, where the technicolor events are “signal” and non b -tagged events are “background.”
7. **Apply each neural network** to these events, and integrate the D_{NN} distribution for a given NN to get the number of technicolor, background, and data events as a function of the “ D_{NN} cut.”
8. **Select the NN discriminant** cut value for each mass point to maximize potential signal and minimize background events.
9. **Evaluate the significance** of any excesses in the data above the background prediction. If the data are free of non-standard model events, then the background prediction is expected to be the same as the number of b -tagged events.
10. **Compute 95% confidence level** upper limits on the $\sigma \times BR$ at each of the 32 combinations of $M(\omega_T)$ and $M(\pi_T)$ mass.

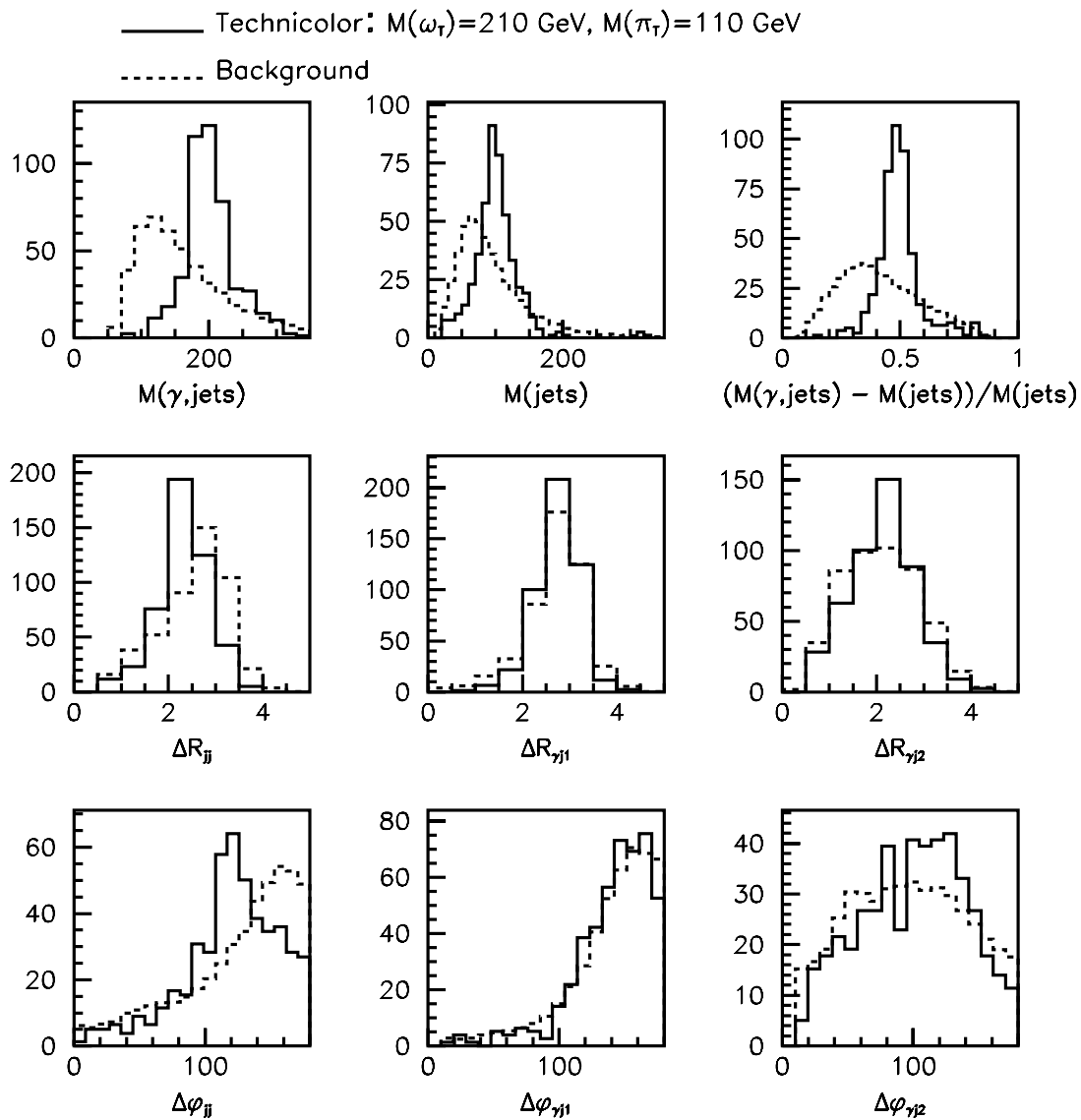


Figure 5.2 An example technicolor signal sample superimposed on background distributions. These show the variables considered for discrimination between technicolor and background before arriving on the final list of five.

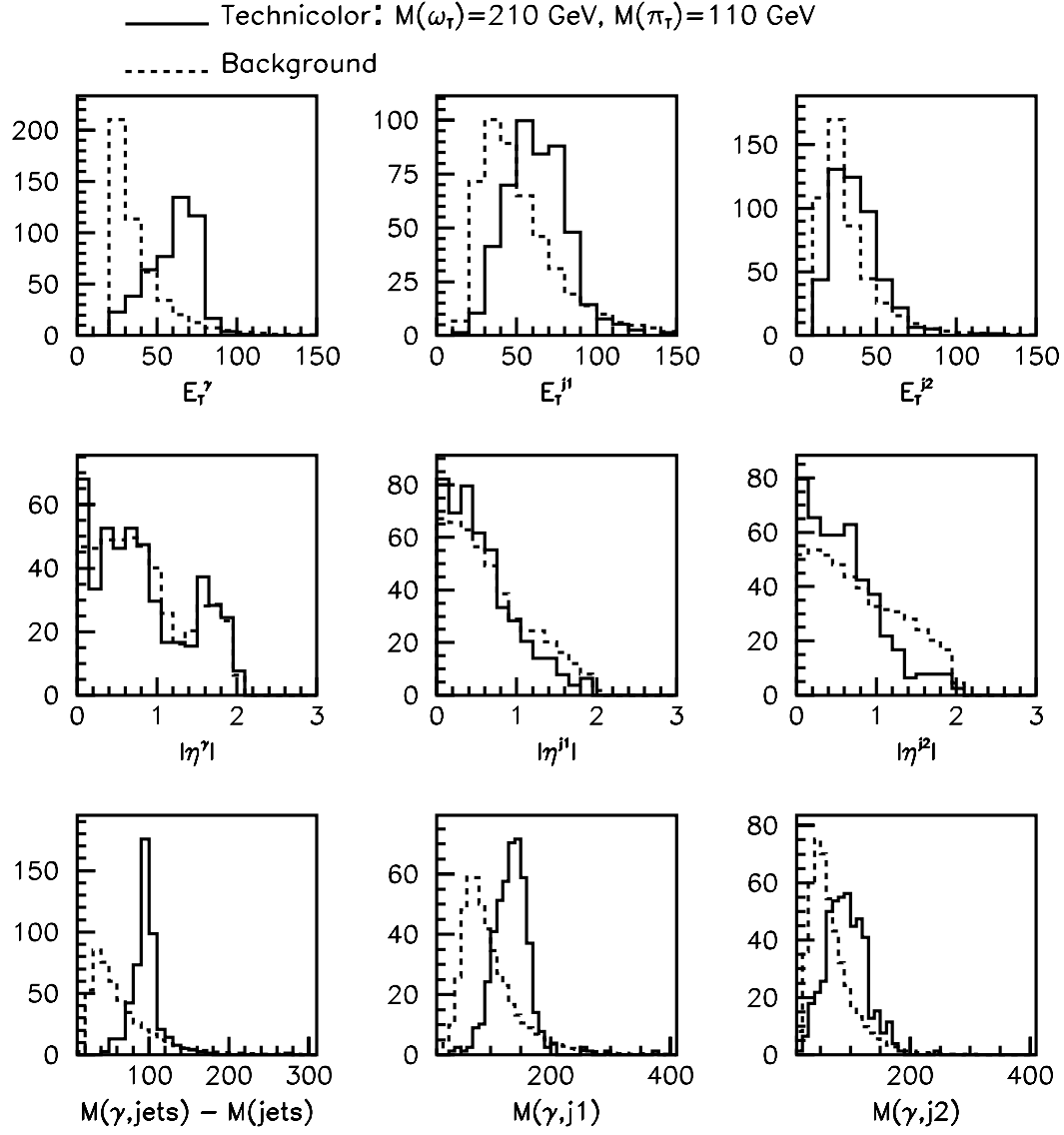


Figure 5.3 Discriminating physics variables continued.

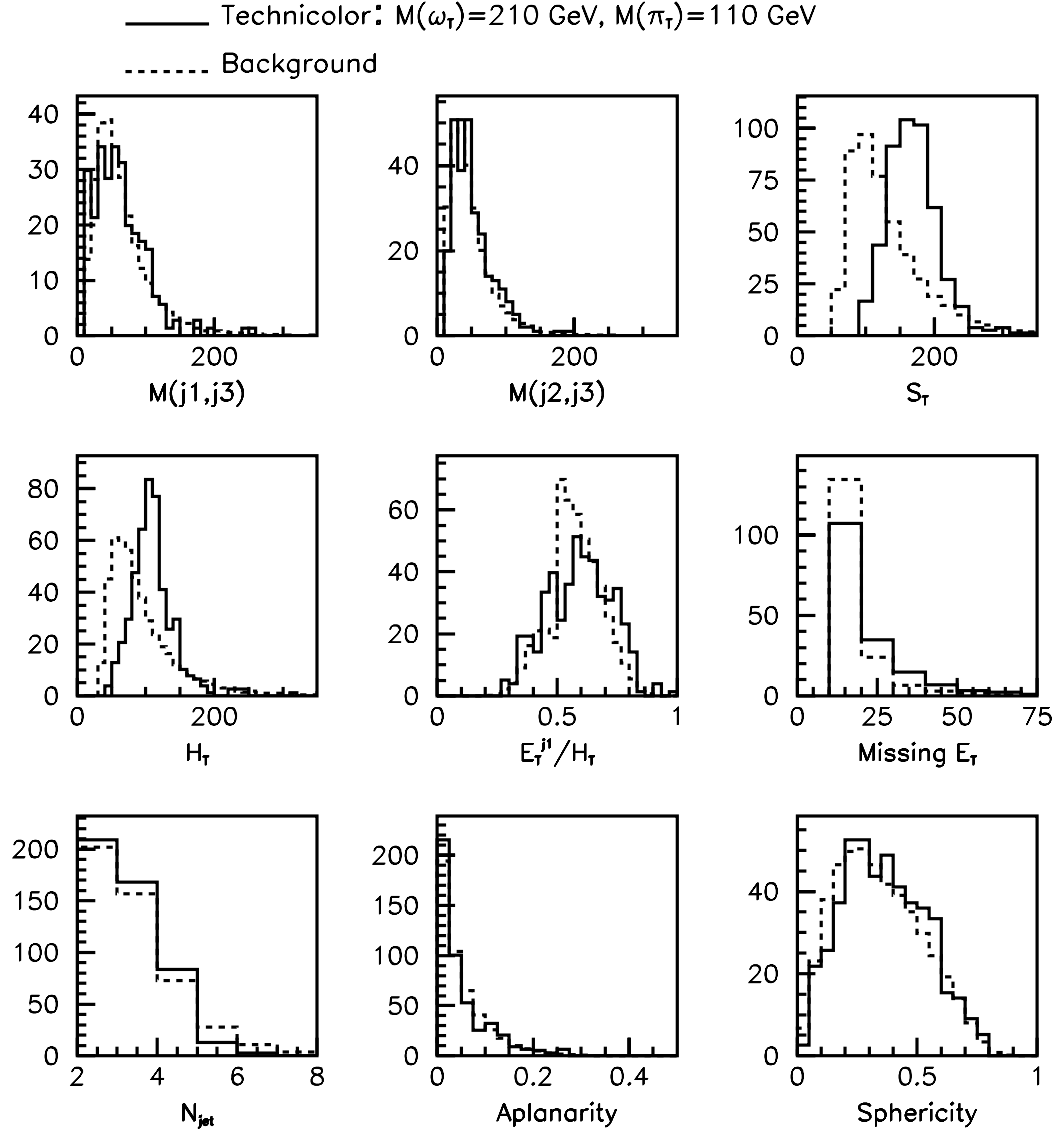


Figure 5.4 Discriminating physics variables continued.

6 DATA SELECTION

The expected technicolor signature is $\gamma b\bar{b}$, so the objects of importance in this analysis are the photon, jet, and muon; the muon indicates the semi-leptonic decay of a b -jet. The two major categories of data selection are *online* and *offline*. The online data selection is handled by the data acquisition system (DAQ), which makes decisions on which $p\bar{p}$ events to write to tape. So, once a decision is made as to what kinds of events are wanted for the analysis, $\gamma b\bar{b}$, we find the event “trigger” that gives the closest specification. In this context, trigger really refers to the data sample that was stored on tape or disk because the corresponding trigger “fired.”

The level 2 (L2) trigger that we require is a superset of $\gamma b\bar{b}$, and has caused the DØ DAQ to store γjj events. This trigger is called GIS_DIJET (or ELE_HIGH for Run 1a), and it triggers on events having the following properties: one or more isolated objects in the EM calorimeter (our photon candidate) with $E_T > 15$ GeV, and $|\eta| < 2.0$, two or more jets with $E_T > 15$, and $|\eta| < 2.0$. Additionally, the total transverse energy scalar sum is required to be > 70 GeV. This trigger was exposed to a beam luminosity of $105 \pm 6 \text{ pb}^{-1}$ [18]. A trigger with the additional requirement of a muon in the event (needed for b -jet identification) was not available. Hence, we begin this search with a sample of γjj events.

With the trigger sample established, more detailed event selection is done. This is made possible by the DAQ’s storage (once the event triggered) of enough information about the jets, photons, etc., in each event to be able to make “quality” decisions about those objects later on. Using this information, the offline cuts are now applied to each event to increase the purity of the sample. The following is a brief summary of all of the selection requirements used in this analysis:

- The DØ data acquisition system has triggered on the events of interest, and has recorded events with a photon candidate and two or more jets. These are the GIS_DIJET(Run 1a), ELE_HIGH(Run 1b) triggers.
- “Clean” requirements. This is the first offline cut, and, as the name suggests, it ensures that the detector and accelerator environment are operating normally. For instance, events with excessive Main Ring activity in the calorimeter is excluded.

- Exactly one photon with $E_T^\gamma > 25$ GeV is required. This is defined to be a narrow, isolated object restricted to the EM calorimeter, and with no track between this EM object and the event vertex.
- Each event must contain two or more jets, where $E_T^{j1,j2} > 20$ GeV and $|\eta^{j1,j2}| < 2.5$. Jets are contained largely in the hadronic section of the calorimeter.
- Events with electron candidates are excluded. These rather tight topological requirements reduce bremsstrahlung backgrounds.
- Missing transverse energy $\cancel{E}_T < 25$ GeV, since no large \cancel{E}_T is expected in the technicolor signal.
- One jet is identified as coming from a b -quark by using the decay $b \rightarrow X\mu\nu_\mu$. This “soft” muon is required to be inside the jet-cone.
- A neural network cut is applied to the events that pass all of the above requirements. The use of neural networks in this analysis is described in Chapters 9–10.

The first offline cut applied is called the “clean” cut. The “clean” requirements ensure that no Main Ring activity, that “hot” cells (spurious, isolated energy) in the calorimeter have $E_T < 10$ GeV, and that good versions of the reconstruction program, DØRECO, were used on the raw data sample (versions 12.00 to 12.12 were found to have bugs). The “DØRECO cut” is 99.92 % efficient, while all of the clean cuts together are $90.74 \pm 0.03\%$ efficient. The error is small due to the large number of events, $\sim 10^6$, used to take the ratio.

Table 6.1 shows the results of these cuts on the data and on a set of technicolor Monte Carlo events. In Chapter 8 we show the details on the computation of the technicolor monte carlo acceptance. The following sections describe each of the data selection requirements in detail.

Photon Identification

The offline γ -ID requirements are set so that the photons have high reconstruction efficiency and reasonable purity, where purity is the probability of the EM object to be a true photon and not a pion (jet) or an electron. The photon shower in the EM calorimeter is narrow and should have most of its energy deposited in the electromagnetic part of the calorimeter. This is in contrast to jets, which have the majority of their energy deposited further out, into the hadronic calorimeter. Also, no tracks or hits in the tracking system are expected from photons, since they are neutral particles. Hence:

- $E_T^\gamma > 25$ GeV. To get higher trigger efficiency, this should be several GeV higher than the trigger threshold.

Table 6.1 Shown are the results from the event selection cuts, excluding the NN cut. A typical Signal MC is shown for comparison. The acceptance correction efficiencies are included, and are described in Chapter 8.

Cuts	Expected Signal MC $M(\omega_T) = 180, M(\pi_T) = 100$	N_{events}
CLEAN ELE_HIGH (Run Ia) GIS_DIJET (Run Ib)	395	956733
$N_\gamma = 1, N_{jet} \geq 2$ $N_{elec} = 0$	269	427453
$E_T^j > 20\text{GeV}$ $ \eta^j \leq 2.5$	196	157259
$E_T^\gamma > 25$ $ \eta^\gamma \leq 2.5$ & ICD cut	163	81717
Iso < 0.1 $\chi^2 < 100$ EM fraction > 0.95	149	44694
HITSINFO	134	33057
$\cancel{E}_T < 25\text{GeV}$	124	32067
μ -tag	11.3	218

- Inter-cryostat detector (ICD) region cut: $|\eta_{det}^\gamma| < 1.1, |\eta_{det}^\gamma| > 1.5$, where η_{det} is the *detector* η , not the physics (reconstructed) η of the particle. The detector- η indicates the actual struck region in the detector. Physics η is the η of the outgoing particle relative to the event vertex. Hence, physics and detector- η disagree when the event vertex is other than $z = 0$.
- $|\eta^\gamma| < 2.5$. This is the limit of the tracking system, so outside of this, it is harder to tell the difference between electrons and photons.
- EM fraction > 0.95. This is the fraction of the energy of the photon candidate carried by the EM calorimeter. A high fraction indicates a high probability of an electron or photon.
- H-matrix $\chi^2 < 100$. Computed by RECO for each candidate from calorimeter shower shape variables. The lower the number, the more likely that the particle is a true EM object.
- $f_{iso} < 0.1$, where

$$f_{iso} = \frac{E(r < 0.4) - E(r < 0.2)}{E(r < 0.2)}, \quad (6.1)$$

where r is the radius in $\eta \times \phi$ space from the cluster center in the calorimeter, and E is the energy deposited within the indicated radius. The smaller the value of f_{iso} , the narrower and more photon-like or electron-like is the shower.

- No tracks in a narrow conical volume between the EM cluster in the calorimeter and the main vertex of the event. These are the HITSINFO cuts, which are explained in more detail below.

When the shower centroid of the photon candidate is traced back to the event vertex, the occupancy in the tracking system is required to be relatively low. This is specified by the the so-called HITSINFO cuts. Once the centroid of the photon candidate is determined, a narrow “road volume” in $\theta - \phi$ space is used to evaluate tracks in between the EM cluster in the calorimeter and the primary event vertex [19]. Depending on the detector subsystem, the road volume is defined in Table 6.2.

Table 6.2 Definition of the road volume for a photon candidate [19]. This volume is inside the tracking chamber between the EM calorimeter signature and event vertex.

HITSINFO road volume		
Detector	$\delta\theta(rad)$	$\delta\phi(rad)$
VTX	0.005	0.012
CDC	0.05	0.0075
FDC	0.005	0.015

Table 6.3 describes the actual values used to specify the HITSINFO cuts. The cryptic-looking variables refer either to the fraction of wires hit in the vertex detector (VTX) or in the central or forward drift chambers (CDC or FDC), or to the *number* of hits in various regions of the central detector (CD). There is typically a lot of stray charge from sources other than the object of interest (our photon candidate), but by adding the HITSINFO requirement, the probability of the EM object being a photon is significantly increased, since no tracks are expected from photons. The following quantities are typically used to specify the HITSINFO cuts within the “road volume” between the EM cluster and the vertex:

- RHVTXW: fraction of wires hit in the VTX
- NHVTX3D: number of VTX hits in the road volume
- RCCDCW (RHFDCW): fraction of CDC (FDC) wires hit
- NHCDCXY (NHFDCXY): number of CDC (FDC) X-Y hits

- NHCDC3D: number of CDC 3-dimensional road volume hits
- NHCDCZS: number of CDC z-segment hits

Table 6.3 Definition of the standard HITSINFO cuts [17, 19]. Candidates passing this cut have a higher probability of being a photon. This probability is sometimes referred to as photon purity.

HITSINFO requirements	
Vertex Chamber	
RHVTXW < 0.3	
NHVTX3D ≤ 8	
Central Drift Chamber	Forward Drift Chamber
RHCDCW < 0.3	RHFDCW < 0.7
NHCDCXY ≤ 20	NHFDCXY ≤ 36
NHCDC3D ≤ 1	
NHCDCZS = 0	

b-jet Identification

One of the ways in which b -quarks decay is via $b \rightarrow X \mu \nu_\mu$. Because DØ is designed to detect muons, this semi-leptonic decay is used to detect the presence of a b -quark jet. The “tagging” muon is required to be at a small angle with respect to the jet, *i.e.* inside the jet cone.

Therefore, a *single* muon tag is required to significantly increase the signal-to-background ratio in this search. A muon emerges from the decaying b -quark for just under 20% of $b\bar{b}$ events, and the basic muon tag requirement ensures that the muon has $P_T^\mu > 4$ GeV and $\Delta R < 0.5$ of the jet centroid, where $\Delta R = \sqrt{\delta\phi^2 + \delta\eta^2}$. As seen in Table 6.1, slightly more than 10% of Monte Carlo signal events pass the μ -tag requirement alone. However, only 0.4% of data events remain. This large difference in acceptance makes the single b -tag a very effective signal vs. background discriminator. Because of low total acceptance of the technicolor signal to a double b -tag ($< \sim 1\%$), only a single muon is required for the event.

The requirement of a μ -tag thus divides data into two samples: the “signal” sample that passes the μ -tag requirement along with the other selection cuts, and the untagged sample. The latter is used to estimate the background by applying a *tag-rate function* to each jet passing a threshold. More detail on the tag-rate function is given in section 7.

Table 6.4 describes the detector variables used to identify a b -jet using a muon. First, the following terms need some explanation:

- **QUAD**: The muon system has 12 quadrants. Only the first four correspond to the “central iron” (or CF) detector. Due to the low efficiency of the “end iron” detectors (or EF), we only use muons entering the CF.
- **IFW4**: Also called muon track “badness.” IFW4 results from a fit of all of the tracking information. The higher the number, the more flaws in the track.
- **MTC**, Muon Tracks in the Calorimeter: Muons leave minimum-ionizing tracks in the calorimeter that can be matched with the rest of the tracking system. The MTC software to do this comparison was not available until Run 1b, hence the reconstruction (DØRECO) version requirement shown in the table. **HFRACT** is the number of “hits” by the muon candidate divided by the *possible* number of hits that it can make in the hadronic portion of the calorimeter. **EFRACT** is the energy in a 3×3 region of cells around the muon track candidate. So, if HFRACT is not 1.0 (100% of the possible hits the muon could make in the hadronic system), then the additional requirement is made on the last EM layer (see the table).

Table 6.4 Requirements for a μ -tag indicating a b -quark jet in terms of detector variables. MTC refers to muon tracks in the calorimeter.

Soft muon b -Tagging Requirements [20, 21]
Muons in CF only ($\text{QUAD} \leq 4$)
Track Quality $\text{IFW4} \leq 1$
MTC cuts if RECO version ≥ 12.13 :
$\text{HFRACT} \geq 0.75$
$\text{EFRACT}_H(1) > 0$ if $\text{HFRACT} \neq 1$
$\Delta R < 0.5$ between muon and jet axis
$P_T^\mu > 4 \text{ GeV}$

Because of radiation damage in the muon chambers from Main Ring activity, there is a run-number dependence to the efficiency of the DØ muon chambers in the Run-1 detector. The following run-ranges are used in this analysis [22, 23], and in particular, the measurement of the tag-rate function (see Chapter 7):

- Run number < 70 K: Run 1a.

- Run number from 70 K to 84 K: Run 1b, before an increase in voltage to the muon chamber wires, and the recharge of muon chamber gas near the time of run number 84 K.
- Run number from 84 K to 89 K: The time after the above change and before zapping the muon chamber wires for cleaning.
- Run number > 89 K: Run 1b, post-zap.

Missing Transverse Energy (\cancel{E}_T)

In $\gamma b\bar{b}$ events, no large \cancel{E}_T is expected in the technicolor signal. The only \cancel{E}_T in the target events comes from the low energy neutrino of the b-quark decay. The background calculation does not currently take this effect into account, hence the \cancel{E}_T comparison between μ -tagged data and background does not hold for $\cancel{E}_T > 30$ GeV.

7 BACKGROUND CALCULATION

As previously stated, this analysis looks for excesses in the $\gamma b\bar{b}$ channel. Since this is a counting experiment, any excesses must be evaluated in reference to the *null hypothesis*, or background, i.e. where technicolor would not exist or is not significant.

After the basic selection cuts, there is still not enough discrimination in the analysis to find such a low-rate signal $\sigma \times BR \approx 1 - 10 pb$. To increase discriminating power, a neural network cut will be applied as a function of technicolor mass. A prediction is now needed of the number of data passing a given neural network cut, after passing the initial event selection. This prediction is the purpose of this background calculation.

The best and simplest background calculations are derived from data. This is partly because the physics and detector sources of background are combined, but also because the events include (by definition) the correct fragmentation and bremsstrahlung effects in a given event. The background calculation in this analysis is indeed data-based, with a carefully-chosen weighting scheme.

The background for this analysis results from several identifying sources: three (or more) jet events where a jet fakes a photon (mostly via $\pi_0, \eta \rightarrow \gamma\gamma$), single direct-photon production (QCD photons), ejj production with an electron losing track information, and hadronic modes of $Z\gamma$ and $W\gamma$. The $W\gamma$ is mentioned, since only one b-tag is required. Many events of these types, along with the hypothesized signal, comprise the $\gamma b\bar{b}$ sample identified in Chapter 6.

Consider the sample of events that fail the μ -tag requirements, but pass the other γjj requirements in this analysis. It is assumed that these γjj events contain the same physics processes (except for soft μ 's produced by heavy quarks) and $e, j \rightarrow \gamma$ fake-rates that exist in $\gamma b\bar{b}$. Therefore, this is the sample that is used to estimate the background. For every μ -tagged event, there are approximately 150 events that pass all cuts except for the μ -tag. Therefore, plenty of data exists on which to base a background estimate.

The next problem is to find a way to weight these 32,000 events, so that they model physics distributions for the ~ 220 b -tagged events. The probability of a b -tag increases slightly with jet E_T .

In addition, the DØ μ detector efficiency is a function of $|\eta|$, where low- $|\eta|$ (central) regions are more efficient than the outer regions. Therefore, a constant weighting for every jet would not be appropriate in modeling the $\gamma b\bar{b}$ sample. In addition, there is an overall dependence of the B -tagging on the run number due to the changes in the efficiency of the central muon system with time. These facts are used to create a variable per-jet weighting called a *tag-rate function*. This function is a measurement of the number of μ -tagged *jets* per untagged jet in the same ranges of E_T , η and run number. In turn, this tag-rate function is used to compute the background estimate. A tag-rate background calculation was also similarly used in the search for the top quark [23] and the fourth generation b-quark (b') [17]. Figures 7.1 and 7.2 show the resulting tag-rate function used in this analysis, and this function is simply the values in the plots shown. The binning was selected to optimize the statistics going into each ratio (of tagged to untagged events), and no fit or smoothing is used. The tag-rate function for jets is expressed as:

$$R(E_T^j, \eta^j, r) = N(r) \times f(E_T) \times \epsilon(\eta, r) \quad (7.1)$$

where R is the tag-rate for jets, r is the DØ run number, and the independent functions f and ϵ are the ratios of tagged to untagged events. The normalizations, $N(r)$, are the following:

- $N(r < 70 \text{ K}) = 4.966$
- $N(70k \leq r < 84 \text{ K}) = 4.639$
- $N(84k \leq r < 89 \text{ K}) = 4.590$
- $N(r \geq 89 \text{ K}) = 4.482$

Each part of the tag-rate function, $N(r)$, $f(E_T)$, and $\epsilon(\eta, r)$ is computed separately. First, $\epsilon(\eta, r)$ is measured independently of E_T^{jet} . Second, $f(E_T)$ is measured independently of η^{jet} and run number, r , then $f(E_T)$ normalized to 1.0. For the next iteration, $f(E_T) \times \epsilon(\eta, r)$ is evaluated on the jets in the untagged sample, totaled, and compared to the number of μ -tagged events in each run-number set. The normalizations are computed as a function of r so that the tag-rate, when evaluated over the untagged events, gives back the total number of tagged events passing the same cuts, and reproduces the physics distributions of the tagged events. The errors in f and ϵ are statistical and a function of the same variables, E_T , η , and r . The normalizations $N(r)$ are considered to be exact, since they are from ratios containing the same jets in the numerator and denominator as the $\epsilon(\eta, r)$ function, so the statistical errors are already included.

To reduce the statistical error in the tag-rate function, the data sample used to derive the tag-rate is slightly more inclusive (372 events) than the one for the counting analysis (which are specified in Chapter 6). The following was required of the events used to derive the tag-rate:

- Trigger and Clean requirements for each event
- Event topology : $N_{jet} \geq 2, N_\gamma = 1, N_{elec} = 0$
- All γ -ID cuts, ICD cut, and $E_T^\gamma > 25$ GeV, $|\eta^\gamma| < 2.5$
- $\cancel{E}_T < 25$ GeV.
- Each jet used to compute the tag-rate function has $E_T^{jet} > 15$ GeV, $|\eta^{jet}| < 2.0$. All other jets are assigned a tag-rate of zero.

Now, the number of background events passing some NN cut may be computed. These events will be a sub-sample of the ~ 220 events originally selected by the counting analysis cuts of Chapter 6. Each untagged event passing the same cuts as the tagged sub-sample is weighted by applying the sum of the tag-rates from every jet in the event above the μ -tagging threshold (see section 6) of $E_T^{jet} > 15$ GeV and $|\eta^{jet}| < 2.0$. A typical tag-weight for an event is 5×10^{-3} and is given by

$$W_{event} = \sum_{jet}^{N_{E_T > 15, |\eta| < 2.0}} R(E_T^j, \eta, r) \quad (7.2)$$

where W is the tag-rate given to the event. For histograms in a given observable, such as jet-mass, $M(jj)$, the proper value of the background and error in the background must be computed. This is done first by filling 3 histograms:

- One with W^+ , the tag-rate for each event, with the statistical error added
- Another with W^- , the tag-rate for each event, with the statistical error subtracted
- A third with the squares of the tag-weights W^2 .

The nominal value of the background histogram is computed by taking the average of the W^+ and W^- histograms. The error in each bin in the resulting histogram is computed by

$$\delta W = \sqrt{\sum W^2 + \left(\frac{\sum W^+ - \sum W^-}{2} \right)^2} \quad (7.3)$$

where the sums are taken over the events in a given bin, and the W^2 term is the statistical error in the sub-sample on which the tag-rate is being evaluated.

Assume for the moment the existence of technicolor-induced events in the data. Ninety percent of the π_T 's produced decay to b-quarks. Combining the probability of a b-quark producing a soft μ with the DØ μ -detector efficiency, less than 10% of the b-quark events will actually become μ -tagged. After all cuts, including neural network and μ -tagging, this would imply an excess above background of ~ 10 events (for some of the “high” $\sigma \times BR$ cases) within a narrow $M(\omega_T), M(\pi_T)$ mass range. Therefore, the other ~ 90 technicolor events that have passed all cuts except μ -tagging will end up in the background sample. However, the average value of the tag-rate is about 7×10^{-3} , so these events would produce a negligible effect on the background calculation. (See Table 11.2 to see typical numbers of events). Similarly, the technicolor events in the tagged sample will have produced a small upward bias in the normalization, $N(r)$, of the tag-rate function. Therefore, the tag-rate method for a background calculation is only valid if the expected signal above standard model is small.

Figures 7.3 – 7.5 show the comparison between data and background for several physics variables. As seen by the χ^2 comparisons shown on the plots for each variable, the bin-to-bin agreement between data and background is good, so the tag-rate method seems to be a reliable method to use for the background calculation. Also shown is the un-tagged sample with no tag-rate applied so that the action of the tag-rate function may be seen. For example, the graph of E_T^{jet1} in Figure 7.3 shows the distribution of the highest E_T jet (the “leading” jet) in the event. The dotted line is a plot of the $\sim 32K$ untagged events, and simply renormalized to the number of tagged events (solid line). The dotted and solid histograms do not correspond very well, but when the tag-rate function is applied to the untagged events the correspondence is much improved. The χ^2 per degree of freedom is shown in each case to compare the predicted number of tagged events with the tagged distributions. The tag-rate function not only gives a normalization, but also contains shape information.

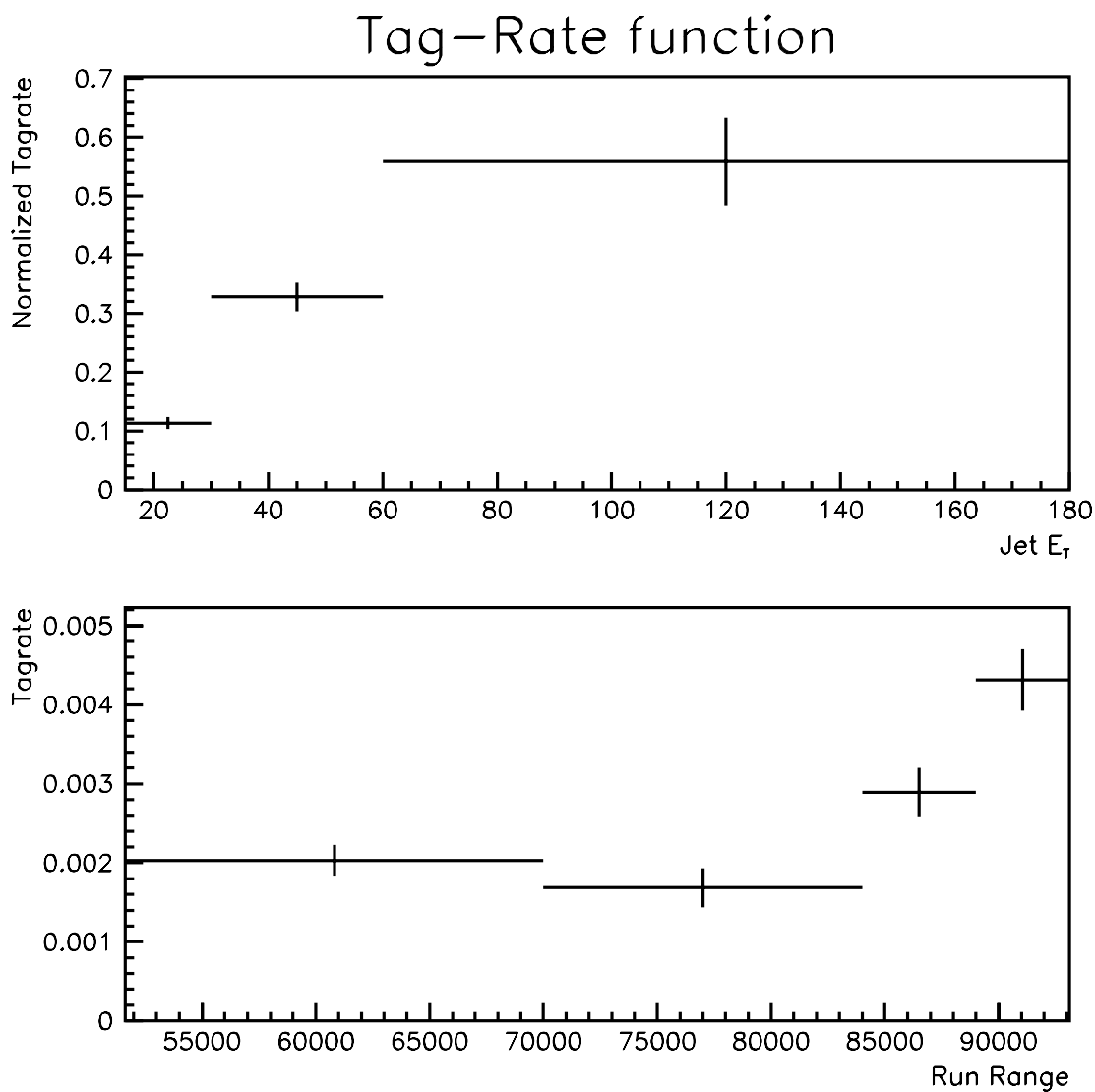


Figure 7.1 The top plot shows the jet E_T tag-rate, $f(E_T)$, and has been normalized. It is assumed to be independent of η and run-number, and is one of the three components of the tag-rate function. The other two components are the normalization as a function of run-number, $N(r)$, and the tagged-jet η dependence, $\epsilon(\eta, r)$ (shown in the next figure). The bottom plot shows the run-range, r , dependence to the tag-rate function, and is a demonstration of how the efficiency of the DØ muon detector changed with time.

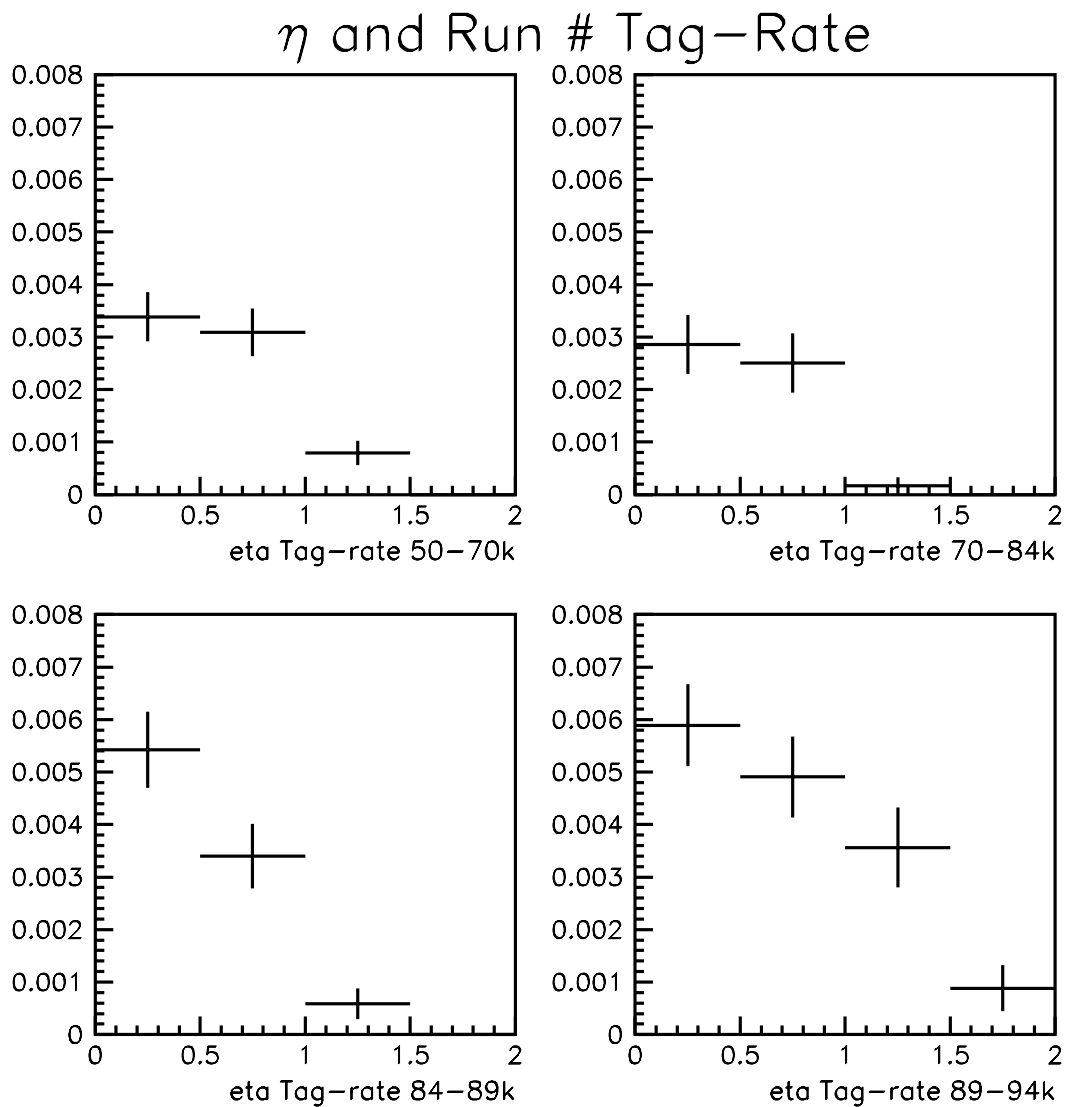


Figure 7.2 These show the other major component, $\epsilon(\eta, r)$, of the tag-rate function. The vertical axis is the rate of the number of μ -tagged jets over the number of untagged jets. The muon detection efficiency changed in different η -regions of the detector at different times, so the run number dependence is necessary in the function, $\epsilon(\eta, r)$, but not in $f(E_T)$.

Data & Tag-Rate Background

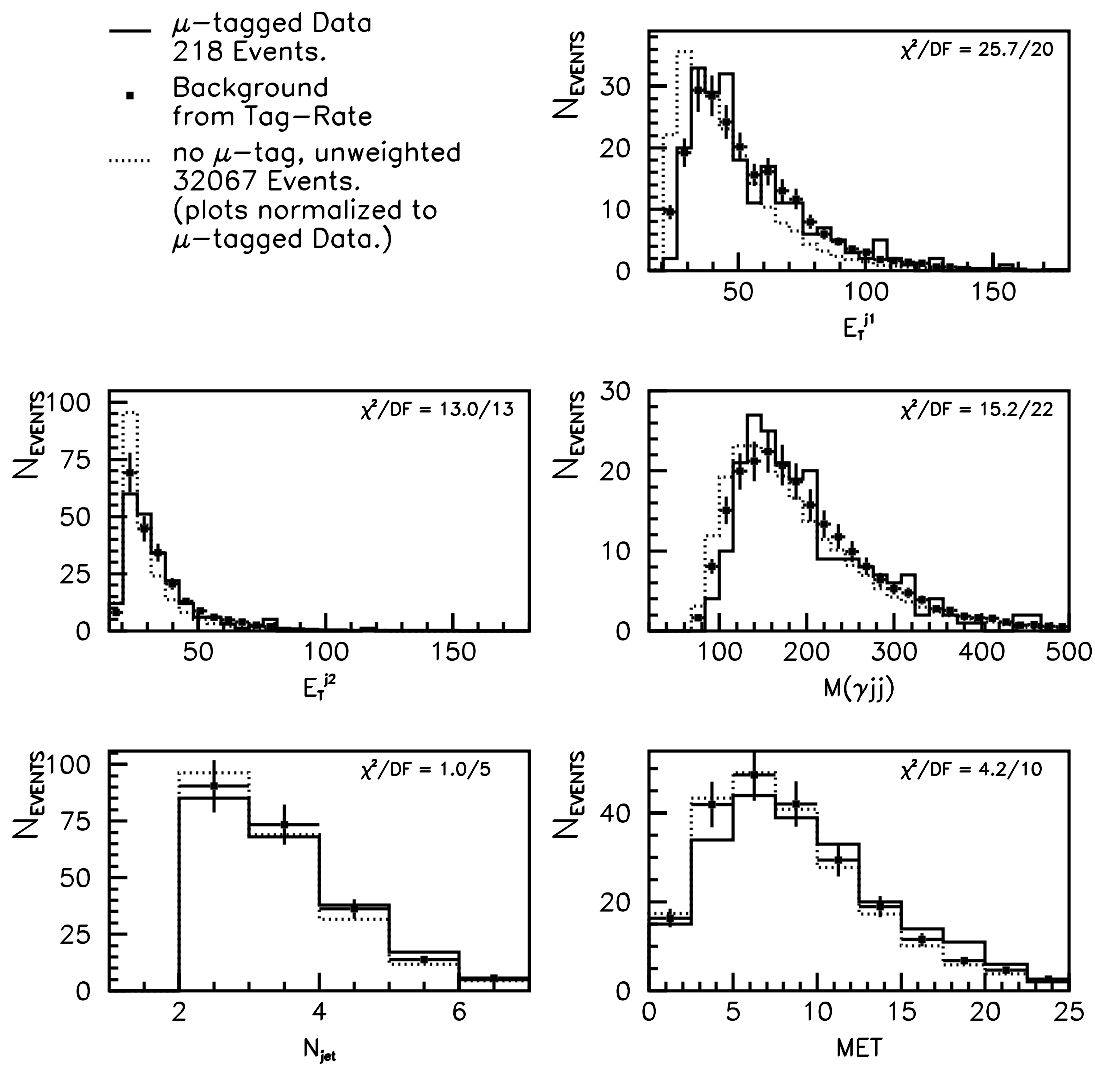


Figure 7.3 Plots showing comparison of Tag-Rate shapes to tagged data. The observables shown here and in the plots that follow show the bin-to-bin correspondence between the background calculation and μ -tagged data for several physics variables.

Data & Tag-Rate Background

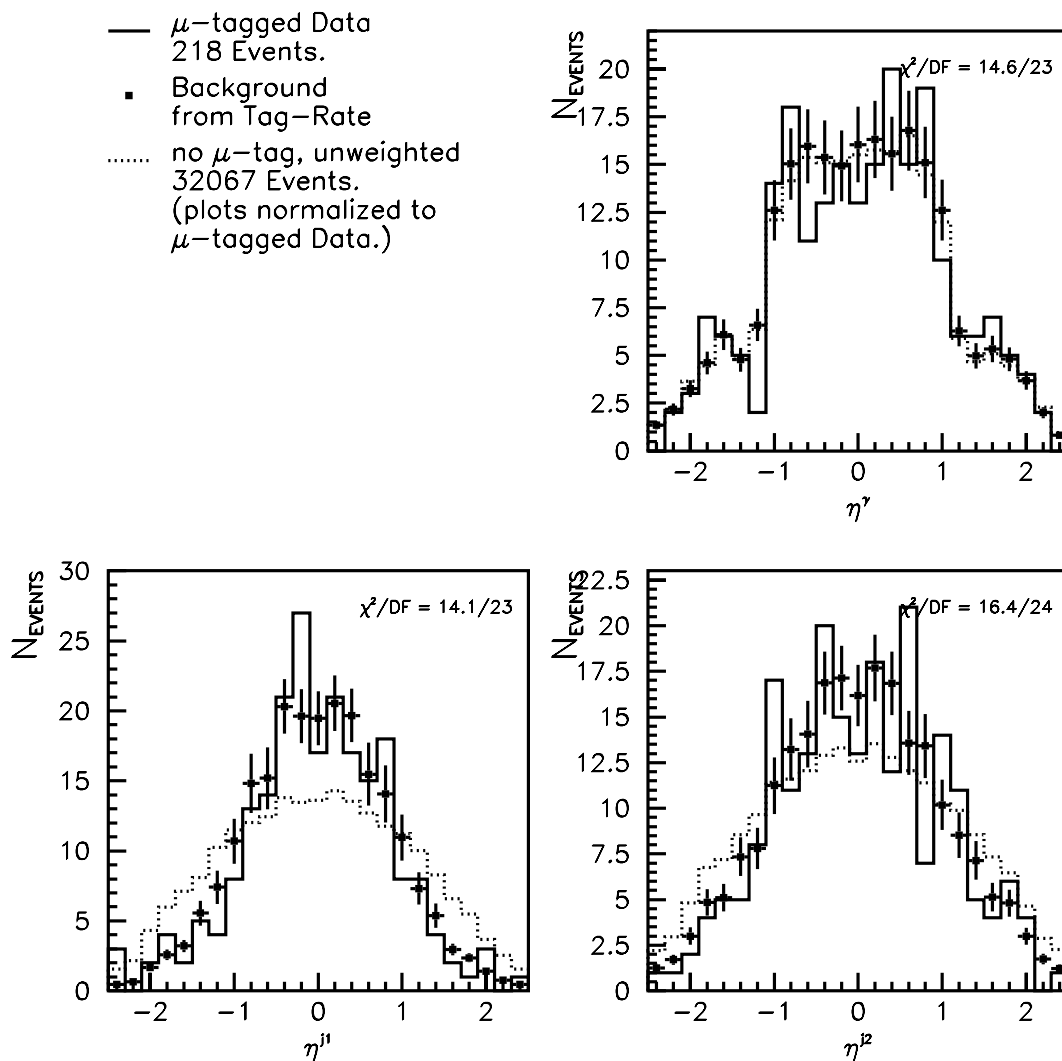


Figure 7.4 Plots showing comparison of Tag-Rate shapes to tagged data. The observables shown here and in the plots that follow show the bin-to-bin correspondence between the background calculation and μ -tagged data for several physics variables.

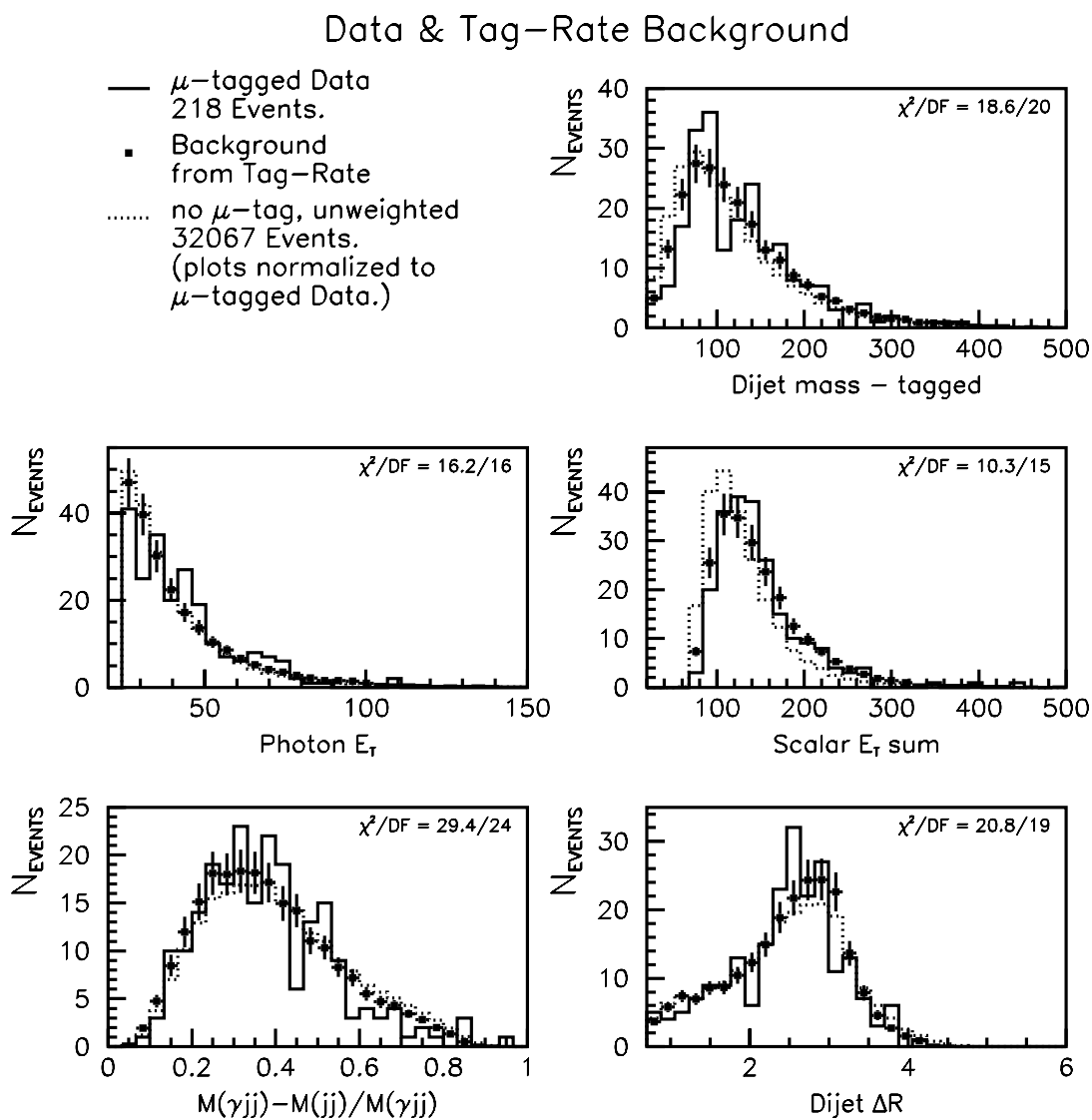


Figure 7.5 These plots also compare background shapes to tagged data. The five observables shown here are used in training the neural networks.

8 TECHNICOLOR MONTE CARLO AND ACCEPTANCE CORRECTIONS

In this search experiment, we compute the number of technicolor events expected in the data after the analysis cuts are made as a function of $M(\omega_T)$ and $M(\pi_T)$. The Monte Carlo program, PYTHIA v6.126, generates the technicolor events, and the detector response to those events is evaluated with the DØ Run-I version of GEANT. In addition, PYTHIA calculates the technicolor LO differential cross-section, $d\sigma/dQ^2$, based on technicolor theory, on the requirements of momentum conservation, and on Lorentz invariance. Calculating the number of technicolor events that pass the selection cuts is now possible. Typically, $\sim 10,000$ Monte Carlo events are used in the acceptance calculation. The number of expected technicolor events (for a given technicolor hypothesis), takes the form:

$$N = \sigma \cdot BR(\omega_T/\rho_T^0 \rightarrow \pi_T/\pi'_T \rightarrow b\bar{b}) \cdot L \cdot \epsilon \cdot \frac{N_{acc}}{N_{gen}} \quad (8.1)$$

where $\sigma \cdot BR$ is the PYTHIA-calculated cross-section (including the specific decay “branching ratio” to $\gamma b\bar{b}$), L is the integrated luminosity taken at DØ during Run I (1992-1996), N_{acc} is the number of technicolor events passing selection cuts, and N_{gen} is the number of technicolor events generated ($N_{acc} < N_{gen}$). Finally, the efficiency, ϵ , is the necessary adjustment to N_{acc} needed to account for inaccuracies in the detector simulation, and for conditions not simulated, such as main-ring “veto.” For an ideal environment, $\epsilon = 1$. Figures 8.1 – 8.3 show the comparison between three selected technicolor mass points, and backgrounds.

Table 8.2 shows the 32 sets of technicolor MC that have been generated. This table includes the $\sigma \times BR$, the acceptance \times acceptance corrections, the relative efficiencies of NN cuts of signal vs. background, and the number of technicolor events generated. There are a number of parameters of the theory other than masses which are also considered, but they are kept constant in this analysis, and are the nominal values suggested in [5], and also later in [6] for the more updated model, which now includes the ρ_T^0 and π'_T decay channels. This low-scale technicolor model corresponds to one that is in

observational range of the Tevatron, and it encompasses the standard model and currently predicts the observed phenomenology of standard model processes. The parameters used within PYTHIA to generate technicolor events and compute the $\sigma \times BR$ as a function of $M(\pi_T), M(\omega_T)$ are listed in Appendix A. The printout in Table 8.1 is a partial listing of typical technicolor event generated by PYTHIA.

Each row in the table corresponds to a particle generated by the $p\bar{p}$ collision (indicated in the first two rows). The column headings indicate the name of the particle produced, the standard Monte Carlo name of the particle (KS & KF numbers), the line number the particle decayed from (“orig”), the four components of momentum and energy, and the mass of each particle.

Table 8.1 An example $\omega_T \rightarrow \gamma\pi_T$ event generated by PYTHIA. The ω_T does not show up since it is a virtual particle in the propagator, and PYTHIA only stores real particles for the event.

Event listing (summary)									
I	particle/jet	KS	KF	orig	p_x	p_y	p_z	E	m
1	!p+!	21	2212	0	0.000	0.000	900.000	900.000	0.938
2	!pbar-!	21	-2212	0	0.000	0.000	-900.000	900.000	0.938
=====									
3	!u!	21	2	1	0.086	0.130	92.765	92.766	0.000
4	!ubar!	21	-2	2	0.154	-0.165	-322.869	322.869	0.000
5	!u!	21	2	3	10.298	-3.412	34.621	36.281	0.000
6	!ubar!	21	-2	4	0.151	-0.161	-315.906	315.906	0.000
7	!gamma!	21	22	0	-62.532	-2.807	-32.448	70.506	0.000
8	!pi_tech0!	21	51	0	72.982	-0.767	-248.837	281.681	109.989
9	!b!	21	5	8	60.425	-27.050	-242.541	251.463	5.000
10	!bbar!	21	-5	8	12.557	26.283	-6.296	30.218	5.000
=====									

The PYTHIA-generated events are simply lists of particles and their momenta. The detector simulation program library, GEANT [15], is combined with the geometry of the DØ experiment [16] to compute the response of the detector to the PYTHIA-generated events. GEANT turns the simulated particles into “hits” in the various components of the detector and simulates the effect that an event (such as the decay of a ω_T) would have on the elements of the DØ detector. The same software, DØRECO, which is used to reconstruct the data taken from Tevatron $p\bar{p}$ collisions, reconstructs the GEANT’ed MC events.

Acceptance Corrections

Some effects, however, are missing from the detector simulation: Main Ring activity in the $80 < \phi < 120$ “ ϕ -hole” of the calorimeter; the “underlying event” that partially populates the central tracking and calorimeter systems; the muon detector’s time-dependent inefficiency due to radiation damage; and the intrinsic inefficiency in the muon system not accounted for by GEANT.

Table 6.1 shows the cuts used in this analysis (not including neural net) applied to an example signal Monte Carlo along with data. The numbers shown include the cuts as well as the different corrections applied to the acceptance, where

$$\epsilon = \epsilon_{\mu} \cdot \epsilon_{hits} \cdot \epsilon_{clean}. \quad (8.2)$$

The ϵ ’s are the corrections applied for the μ -ID, γ -ID (HITSINFO correction), and CLEAN requirements respectively. This total correction is applied to Equation 8.1.

b-tagging Correction

The number of signal Monte Carlo events is corrected for the muon detection efficiency, usually referred to as the “eye-scan” efficiency [24]. This is calculated by looking at ~ 1000 MC and data event displays with muons, and computing a factor to correct the overestimate of the acceptance of muons by GEANT. Muons in the Central Iron region (CF) are given a correction of $94.1 \pm 1.8\%$ and $91.1 \pm 1.9\%$ in the End Iron (EF).

Due to the main-ring passing through the DØ calorimeter, there is a ϕ region in which the muon detection efficiency is lower. This is called the “ ϕ -hole.” The ϕ -hole ($80^\circ < \phi^\mu < 120^\circ$) muons are given a correction of $95 \pm 5\%$ for Run 1a, $90 \pm 5\%$ for Run 1b pre-zap, and no correction for Run 1b post-zap [21]. Since the MC is corrected instead of the data, we take a weighted average of the run-number dependent corrections: the fraction of events in the γjj trigger sample from Runs 1a, 1b pre-zap, and 1b post-zap, respectively, are used to compute a weighted-average ϕ -hole correction of $93.9 \pm 3.4\%$ for found muons within the ϕ -hole.

HITSINFO (no hits in road) Correction

The “underlying event” is a feature of most $p\bar{p}$ interactions, and results from the breakup of the p and the \bar{p} after one quark from each is involved in the hard (high- E_T) interaction. This produces a low-energy (~ 1 GeV) shower of particles, which register in the tracking system and in the calorimeter.

The technicolor events of this analysis were generated without an underlying event added, so the extra occupancy of the central tracking system due to charged particles from the underlying event is not simulated. Hence, the number of events passing the no hits in road, or HITSINFO, requirement for γ -ID is overestimated. The technique of using ϕ -rotated $Z \rightarrow ee$ events is used here to derive the correction. The assumptions are that the physics of any given event is ϕ -independent, and that high-energy electrons and photons have the same signature in the calorimeter system. So, when the $Z \rightarrow ee$ events are rotated 90° away from their tracks, the γ -ID software can no longer tell the difference between the electron produced by the Z and a real photon, since photons are neutral and leave no track in the drift chambers. The fraction of these ϕ -rotated $Z \rightarrow e^+e^-$ events passing the HITSINFO cut is $90 \pm 4\%$ [17]. This is the rate-correction applied to the MC events for this cut.

CLEAN Correction

As discussed in Section 6, main ring activity in the calorimeter, hot-cells in the calorimeter and RECO version cuts are not accounted for in the detector simulation, so a correction is applied to the acceptance. The applied correction is $90.74 \pm 0.03\%$, and was calculated by taking the ratio of events in the data passing the initial trigger requirement (*i.e.* the ELE_HIGH and GIS_DIJET trigger sample), with and without the CLEAN requirement. To verify the independence of the CLEAN correction to event selection cuts, the same ratio was taken after the remaining data selection cuts (but not the NN cut), and the result was consistent ($88 \pm 2\%$).

Some Observables Showing Signal & Background

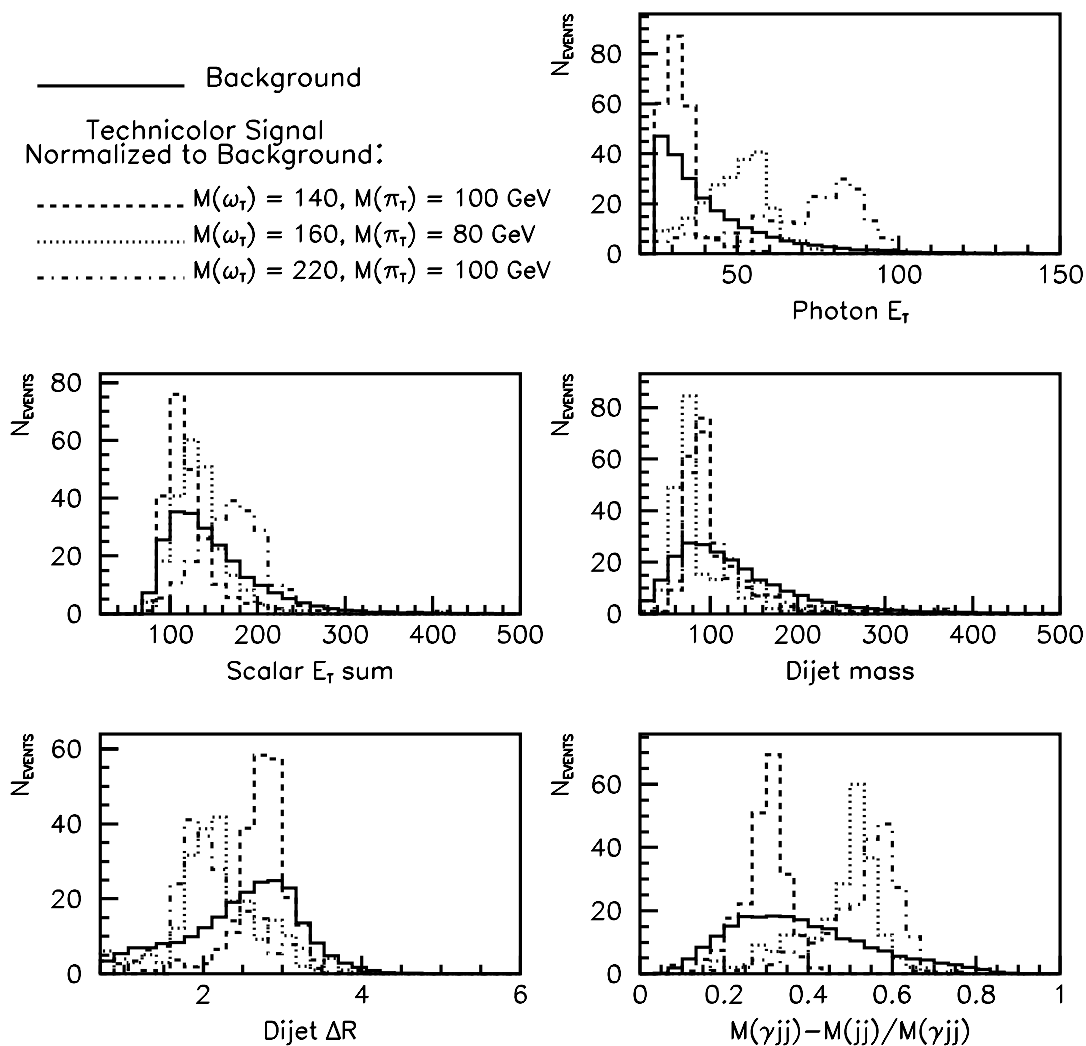


Figure 8.1 Here are five observables which show how technicolor would present itself in the data for 3 different mass values compared with background distributions, with the background calculated using the tag-rate method described in Chapter 7. These five variables have excellent signal-to-background discrimination properties, and are used in training the 32 neural networks to search for technicolor events in the data.

Some Observables Showing Signal & Background

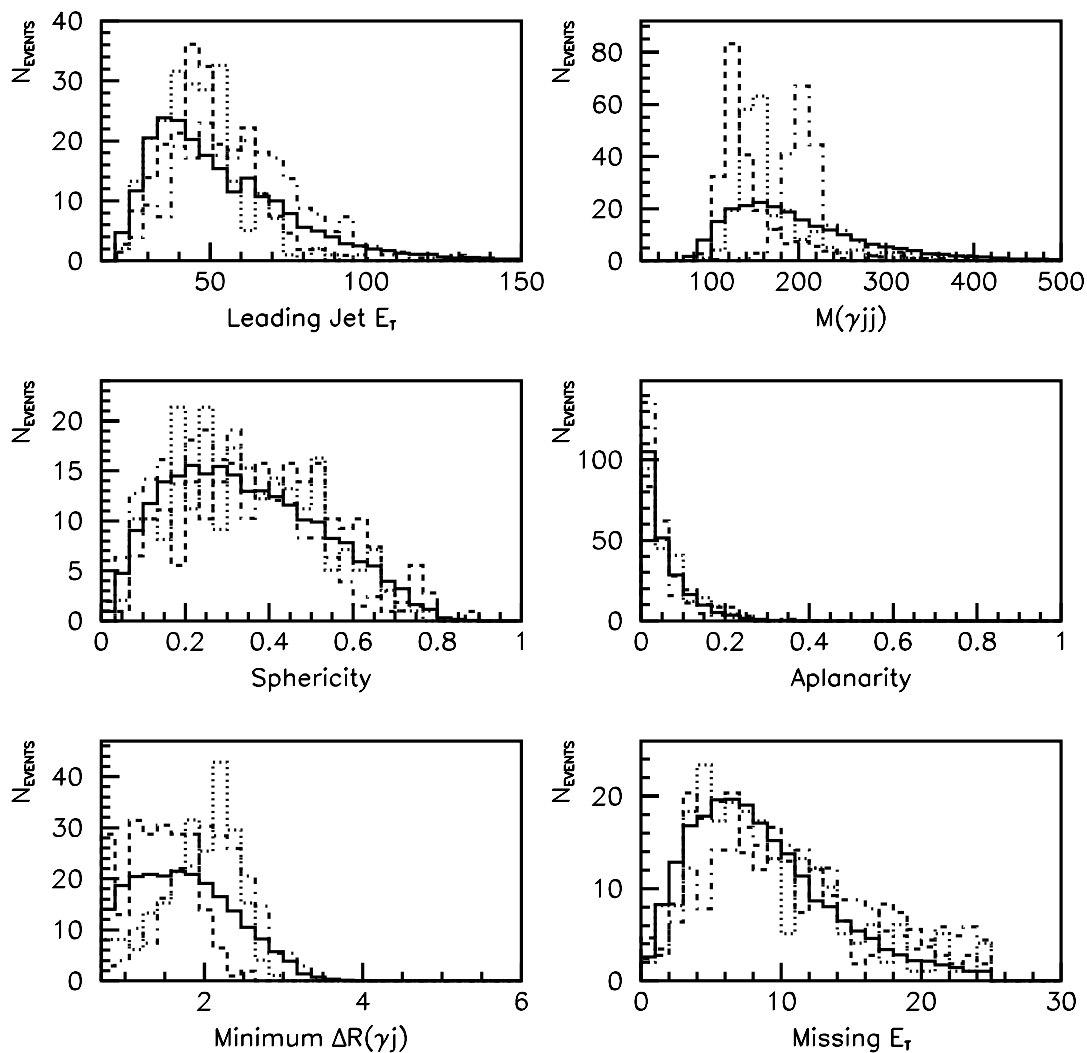


Figure 8.2 These are some of the variables that were considered for NN training, but not currently used. They either have relatively little discrimination power or are redundant in conjunction with the five NN variables currently in use.

Some Observables Showing Signal & Background

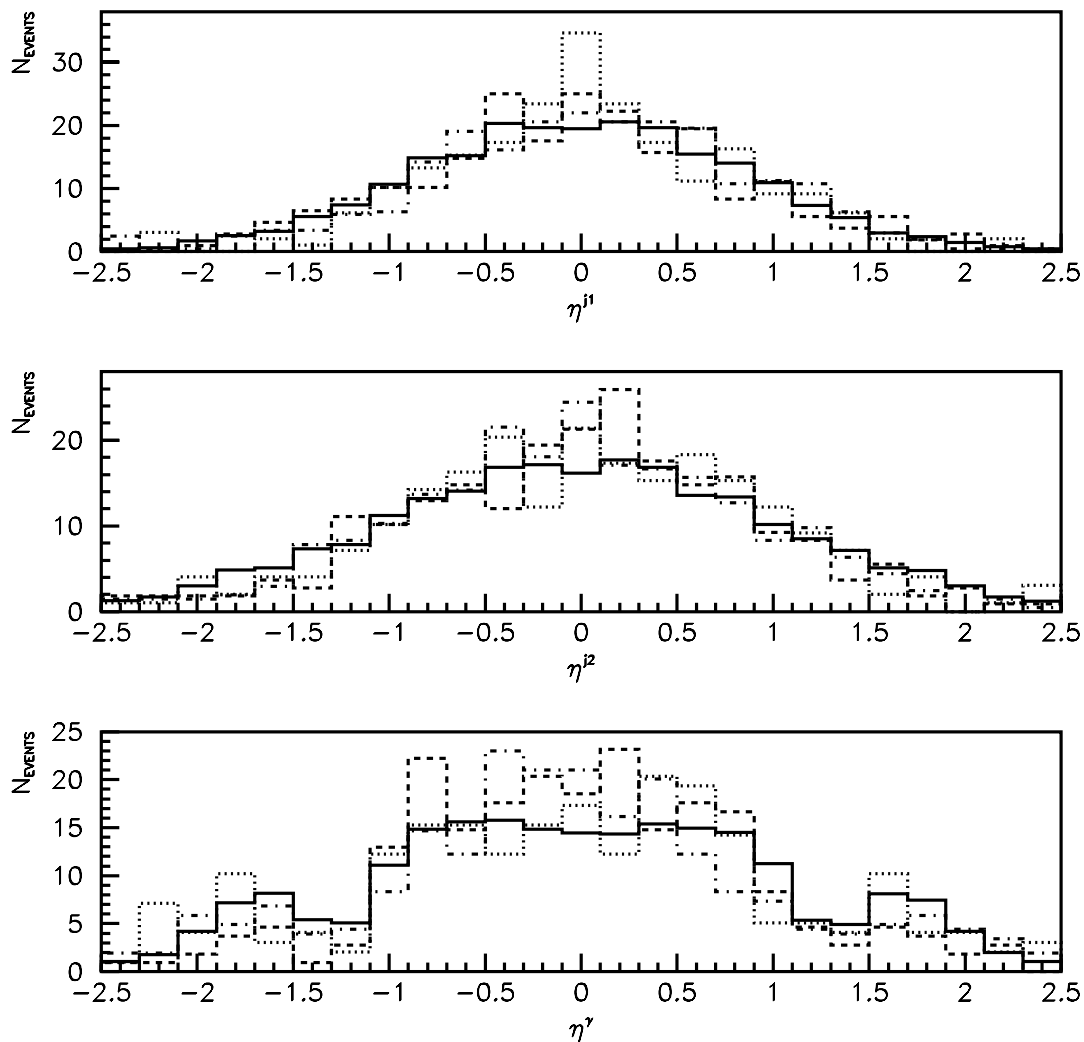


Figure 8.3 The physics- η variables of the γ and the two leading jets. The Monte Carlo events are shown to correspond well to the background events derived from DØ data. It can also be seen that the η distribution alone is not an effective discriminator between technicolor MC and background.

Table 8.2 Technicolor Monte Carlo (PYTHIA v6.126 with GEANT, SHOWERLIB). Shown are all of the mass combinations generated for this analysis. The quantity $A \times \epsilon$ is the fraction of events passing selection cuts with the correction applied. The last column is the relative fraction of technicolor and background events passing a NN cut of $D_{NN} > 0.9$.

Masses (GeV)		Events Generated	$\sigma \times BR$ (pb)	Initial Selection $A \times \epsilon$	$\epsilon_{D_{NN} > 0.9}^{rel}$	
$M(\omega_T)$	$M(\pi_T)$				MC	Bkg
140	40	13280	9.53	0.008	0.431	0.024
140	60	10000	9.13	0.009	0.310	0.010
140	80	10000	15.62	0.013	0.250	0.016
140	100	14000	8.59	0.016	0.299	0.020
160	40	14500	5.86	0.011	0.745	0.024
160	60	9985	5.81	0.013	0.507	0.030
160	80	13000	11.89	0.016	0.297	0.019
160	100	13500	9.42	0.022	0.410	0.037
180	40	14000	3.92	0.016	0.796	0.020
180	60	14000	3.84	0.017	0.625	0.027
180	80	9507	4.19	0.021	0.573	0.039
180	100	8849	7.57	0.029	0.365	0.024
180	120	9507	5.79	0.028	0.448	0.045
200	20	14500	2.75	0.006	0.719	0.058
200	40	9016	2.71	0.015	0.749	0.027
200	60	10000	2.62	0.020	0.676	0.037
200	80	12000	2.71	0.023	0.527	0.033
200	100	14000	4.05	0.029	0.614	0.047
200	120	10000	4.88	0.032	0.484	0.039
210	90	10000	2.35	0.028	0.547	0.047
210	110	9506	3.41	0.036	0.459	0.041
220	60	14000	1.90	0.023	0.671	0.025
220	80	4856	1.87	0.032	0.685	0.073
220	100	14000	2.10	0.030	0.645	0.042
220	120	14000	2.83	0.033	0.497	0.034
260	60	9506	1.06	0.029	0.871	0.042
260	100	10000	1.02	0.035	0.756	0.052
280	40	3888	0.85	0.020	0.942	0.038
280	120	4909	0.81	0.039	0.694	0.053
300	40	10000	0.67	0.013	0.972	0.035
300	80	10000	0.61	0.030	0.947	0.041
300	140	9008	0.67	0.040	0.802	0.041

9 NEURAL NETWORK IMPLEMENTATION

After the $\gamma b\bar{b}$ events are selected, there are still a relatively small number of technicolor signal events and a large number of background events. We now pursue a multivariate technique to better separate potential technicolor events from backgrounds. In this analysis, neural networks are used to accomplish this separation. The purpose of the neural networks is to categorize events in the data set into one of two types: technicolor candidates and background events. As a method of finding the optimal region of physics variable-space, neural networks (NN) are able to yield significantly better signal acceptance and at the same time lower backgrounds compared to other methods [25].

In general, a neural network must be trained on a sample of signal (in this case, technicolor MC) and on a sample of background events. During training, the neural network output value, called the discriminant, or D_{NN} , is constrained to yield a value near 0 for the background events and 1 for the signal events. In other words, the NN is trained to recognize signal and background events based on a selected set of events (the training sample) and the physics variables associated with each event.

The NN program JETNET [26] is a “feed-forward” NN program with 3 layers of decision points or “nodes”: the input layer, the hidden layer, and the output layer. The structure is shown in Figure 9.1, and was inspired by the way in which the neurons of the brain function and “talk” to each other [27]. Feed-forward neural networks have information flow in one direction from the input layer to the hidden layer, then finally to the output layer. In other words, no feed-back mechanism is included in these neural networks. The input layer nodes correspond to the input physics variables selected for their signal-to-background discrimination properties. The hidden layer provides additional nodes to process the information contained in the training samples. The user selects the number of hidden nodes to optimize the discriminating characteristics of the neural network. In general, the last layer – the output layer – can have many nodes, but for our purposes, only one node is used, and it gives the output value of the neural network, D_{NN} , which varies between 0.0 and 1.0.

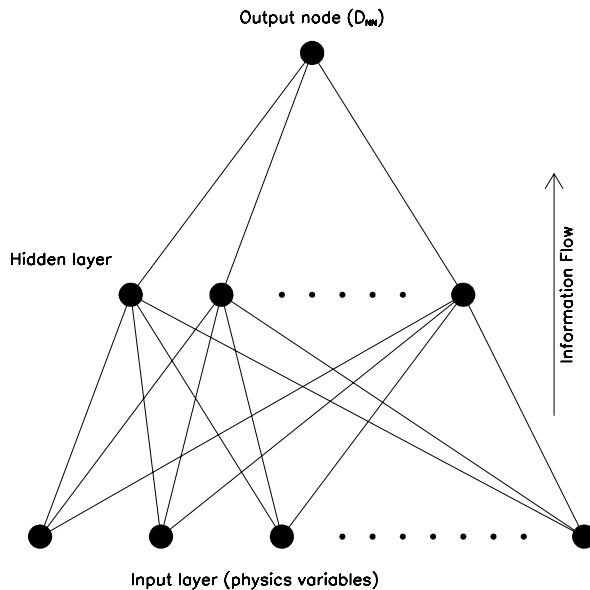


Figure 9.1 Diagram showing the node structure of a feed forward neural network with multiple inputs, one hidden layer, and a single output node, which is the neural network discriminant, D_{NN} . The input nodes correspond to the set of input physics variables selected to best discriminate between signal and background events.

The Input Layer: Physics Variables

The number and type of input variables – the input nodes– determine the success or failure of the NN. These must be a set of variables that already discriminate signal from background moderately well without being redundant. Figures 8.1 and 8.2 exhibit some possible input variables. Note the strong peaks in the mass variables $M(\gamma, jets)$ and $M(jets)$, which represent the $M(\omega_T)$ and $M(\pi_T)$ masses. To make it easier for the neural network to train, these input variables are normalized to give values of order 1. This is done by estimating the maximum value of a given variable, and dividing. For example, for photon transverse energy, E_T^γ , the actual variable used is $E_T^\gamma/130$. It is not imperative that the denominator actually be the maximum value, just that the adjusted value be of order 1.

After an extensive selection process, the following variables have been selected which, together, yield very good technicolor and background discrimination. The normalizations are shown also:

1. $E_T^\gamma/130$ – Photon transverse energy.
2. $S_T/350$ – This is the sum of the transverse energies, E_T , of all jets, the photon and the muon in the event.
3. $M(jets)/200$ – Jet mass of the event. This is the magnitude of the four-vector sum over the jets in the event.
4. $\Delta R(j_1, j_2)/5$ – Opening ΔR between leading (highest E_T) two jets: $\Delta R = \sqrt{\Delta\phi^2 + \Delta\eta^2}$.
5. $\frac{M(\gamma, jets) - M(jets)}{M(\gamma, jets)}$ – Reduced mass difference, where $M(\gamma, jets)$, the photon + jet mass is the magnitude of the four-vector sum of those objects.

A fuller description of the definitions and variable selection process is described in Chapter 5. These five variables are the input nodes for the first layer of the neural network.

The Hidden Layer

The neural network is able to identify “contour regions” in physics variable space which have a high probability of technicolor signal. The number of hidden nodes defines the complexity of these $N - 1$ dimensional contours in variable space, where N is the number of input variables. Typically, on the order of $2N$ hidden nodes are used. Currently, the number of hidden nodes is set to 12 with the 5 input variables. The number of hidden nodes was selected by trying different values ranging from 5 to 20, and arriving at the smallest number of nodes (12) in which the search results were stable.

As Figure 9.1 illustrates, the lines indicate the information-flow from layer to layer. Each node in the hidden layer receives information from every node in the input layer. Like the input nodes, each of the hidden nodes (indexed by j) has a value h_j associated with it that also ranges from 0 to 1, where

$$h_j = g \left[\left(\sum_i^{N_{inputs}} w_{ji} \cdot x_i \right) - \theta_j \right]. \quad (9.1)$$

The weights w_{ji} and thresholds θ_j are found numerically as a result of the training process, and the physics variables are x_j . The function g is the sigmoid function shown in Figure 9.2, and models the “firing” of the neuron or node when the inputs exceed the threshold θ_j for that node.

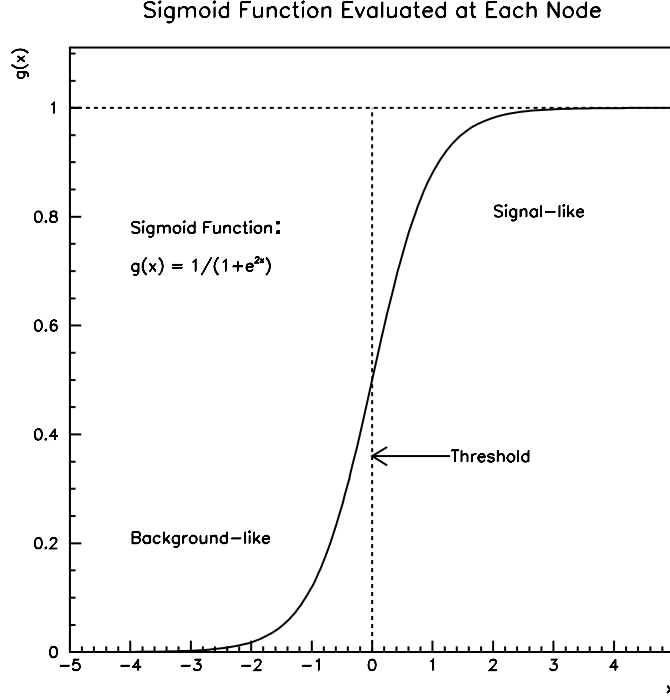


Figure 9.2 This is the “activation function” used to give the output value at each of the hidden nodes and the output node, D_{NN} . The function origin is the threshold value, θ , and may be different for each node.

The Output Layer: D_{NN}

Once the neural network is trained, it is a continuous, well-defined function of the selected input physics variables. The final output value of the NN is called the neural network discriminant, D_{NN} . This value is computed by summing the weighted outputs from the hidden layer, subtracting a threshold and evaluating the result again using the sigmoid function of Figure 9.2. In other words,

$$D_{NN} = g \left[\left(\sum_j^{N_{hidden}} w_{j1} \cdot h_j \right) - \theta_{D_{NN}} \right], \quad (9.2)$$

where h_j are the outputs of the hidden layer nodes given by Equation 9.2, w_{j1} are the weights between the hidden layer and the single output node, and $\theta_{D_{NN}}$ is the final threshold value.

The training algorithm adjusts the output value of the NN to be as close to 1 as possible for the ensemble of signal events, and as close to 0 as possible for the background ensemble, since their type is known *a priori* in the training. This is called “supervised” training. In practice, the signal and

background events will be spread out in D_{NN} with background events tending to the low (0.0) values, and signal tending to the high (1.0) values.

The weights w_{ij} and thresholds θ are found by minimizing the error function

$$E = \frac{1}{2N_p} \sum_{p=1}^{N_p} (D_{NN}^{(p)} - t^{(p)})^2 \quad (9.3)$$

using an iterative method, called “back propogation.” N_p is the number of “patterns” or events used in training, and $t^{(p)}$ is the known value 1(0) of each signal(background) event. The sum is over all of the events in the training sample.

The weights and thresholds are updated after each pass (or epoch) on the training events by using the rule

$$\vec{\omega}_{t+1} = \vec{\omega}_t + \Delta \vec{\omega}_t \quad (9.4)$$

where

$$\Delta \vec{\omega}_t = -\eta \frac{\partial E}{\partial \vec{\omega}} + \alpha \Delta \vec{\omega}_t, \quad (9.5)$$

and $\vec{\omega}$ refers to the vector of weights and thresholds of the neural network. The learning rate η is generally selected to be 0.01, as is the case in this analysis. A momentum term, the second term in Equation 9.4, is also added to stabilize the learning, where $\alpha = 0.9$

Unfortunately, even after being fully trained there are cases where some signal events are given values near 0.0, and background events may have values of D_{NN} near the signal region of 1.0, meaning that those background events are indistinguishable from technicolor events. Figure 9.3 shows an example of the output of a trained neural network. As expected, nearly all of the signal events have a D_{NN} value close to 1.0, where a large proportion of background events are much less than that. However, a number of background events continue to have high D_{NN} . A cut of $D_{NN} > 0.9$ would now be a very effective way to eliminate a large portion of the background events, while accepting a relatively large number of technicolor signal events. This property allows us to perform a focussed search for excesses in the data indicating a very particular signature.

Figure 9.4 compares data and background passing event selection cuts when applied to trained neural networks. These plots also show the correspondence between the tag-rate background calculation and the b -tagged data.

Training-Sample Selection

Before we can use neural networks as a tool, we must select signal and background event samples to be used for training. As mentioned earlier, technicolor signal is generated using PYTHIA for many combinations of $M(\omega_T)$ and $M(\pi_T)$. The background sample used for training is a subset of the γjj data. All training samples pass the event selection cuts outlined in Chapter 6, except for the b -tag requirement, which they are required to specifically fail. Hence, the b -tagged events in the search that are evaluated by the trained neural networks are an independent sample. Typically ~ 2000 events from both samples are used in training.

It is also important to ensure that the signal and background samples have the same E_T cuts applied to them so that “trigger turn-on” effects in the training samples are minimized. Otherwise, the NN may assign a high discriminant value (D_{NN}) to a region in which the data are not completely efficient relative to the Monte Carlo signal sample. This would bias the search to a region of variable-space where a potential signal could not actually be found, and cause the 95% confidence limits on $\sigma \times BR$ to be artificially low. This fact is partially what drove the selection cuts for this search.

Other Considerations for Training

The number of epochs, or times that the samples are “looped over” during training, is also considered. From 3000 - 5000 epochs are used in this analysis. This was selected by increasing the number of epochs until the discrimination power of the trained NN reached a stable value.

Because each NN can only search for technicolor in a fairly narrow mass-range, a different NN is trained for each of the 32 technicolor mass points; hence, each mass point in the search is separately optimized. Table 8.2 shows the acceptances of MC and background for a $D_{NN} > 0.9$ cut. As seen in the table, from 25 to 97% of technicolor monte carlo events pass the this cut, but no more than 7% of background events pass this cut. Hence, the neural network is an effective discriminating tool.

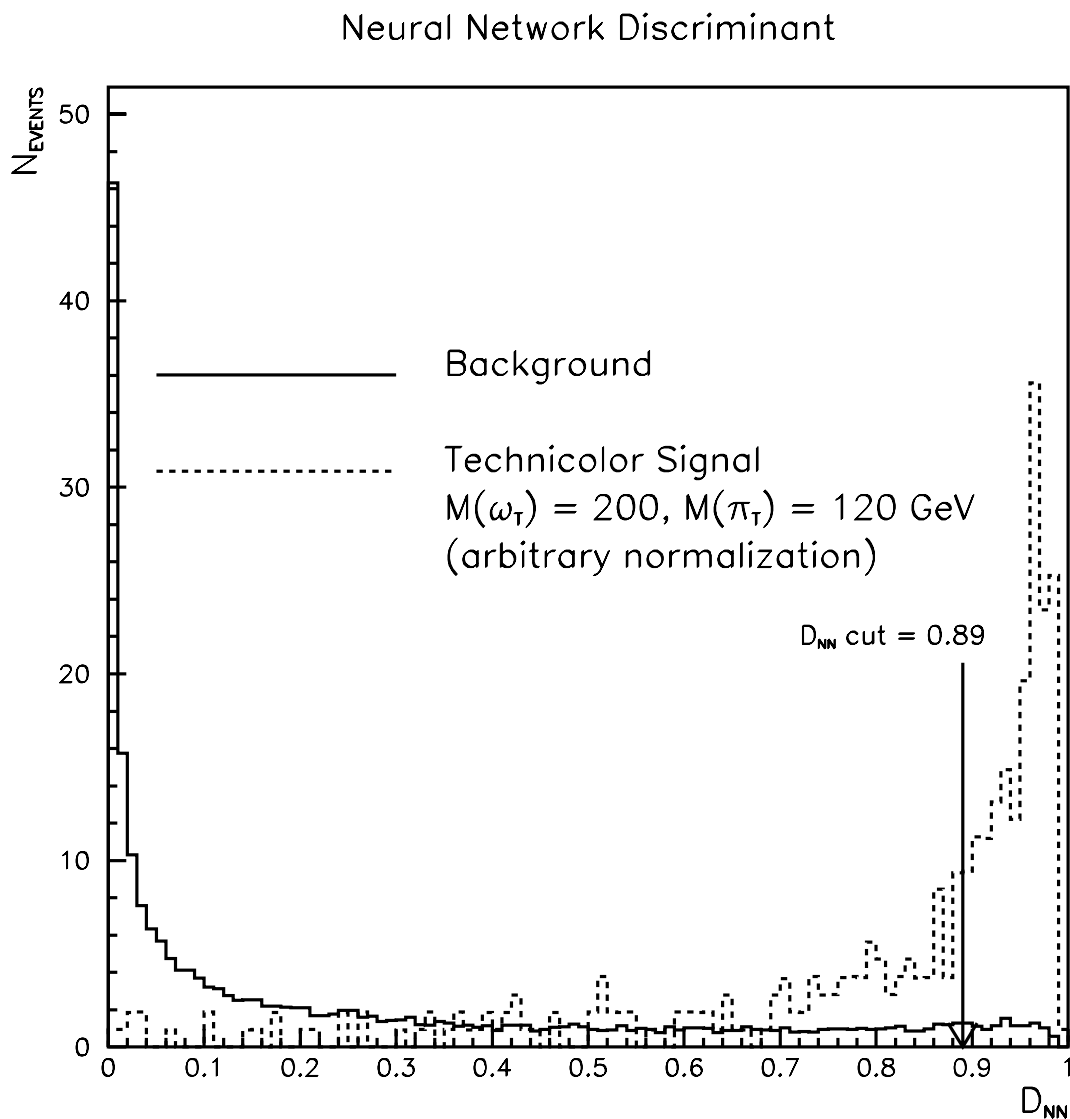


Figure 9.3 An example output of a neural network trained on a set of untagged technicolor signal events and a subset of untagged γjj data. The arrow shows where the D_{NN} cut was placed to get the best discrimination between signal and background by finding the minimum expected cross-section limit. Chapter 10 discusses the selection of the D_{NN} cut for each neural network trained at each technicolor mass point.

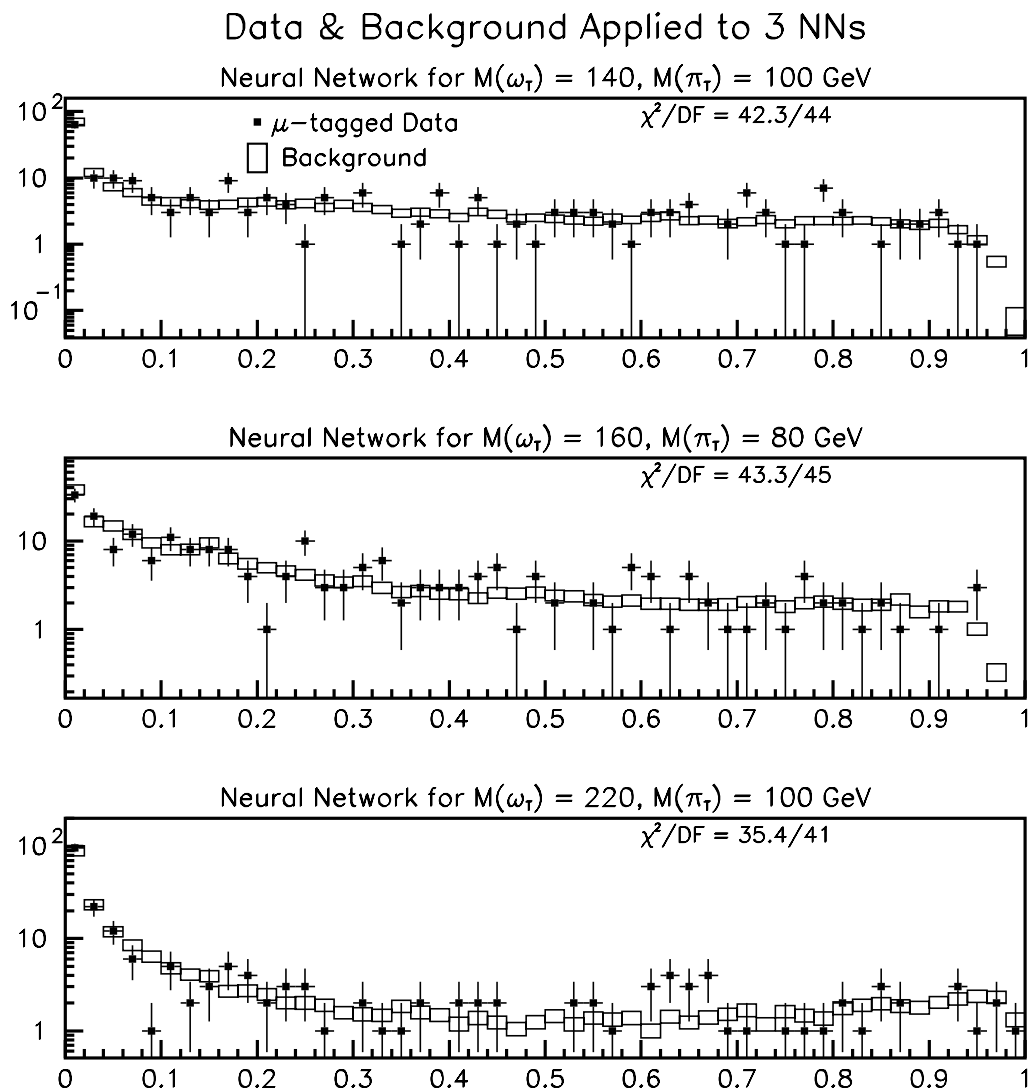


Figure 9.4 These plots show the comparison between the background calculation as a function of D_{NN} and the b -tagged data for 3 examples of neural networks. The events here pass the event selections mentioned in Section 6. There are 218 b -tagged data events to compare with 32,067 untagged events applied to the tag-rate function. The χ^2 comparison indicates good agreement between the data and background. This visual also shows the *lack* of evidence for technicolor events in the data for these 3 mass ranges.

10 FINAL EVENT SELECTION USING NEURAL NETWORKS

With the neural networks trained on each technicolor mass point, we must now select a D_{NN} cut for each technicolor mass point to eliminate as many background events as possible while still preserving a high relative efficiency of technicolor signal events. The two criteria used to accomplish this are the “discovery” and the “limit setting” criteria. These criteria depend on the number of events of background and technicolor MC passing a given D_{NN} cut.

The first method maximizes the value of the discovery significance formula:

$$S(D_{NN}) = \frac{N_{MC}}{\sqrt{N_{MC} + N_{bkg}}}, \quad (10.1)$$

where N_{MC} and N_{bkg} are the expected number of technicolor events and background events that pass a given D_{NN} cut. Recall that N_{bkg} is calculated by the tag-rate function described in Chapter 7. The maximization of Equation 10.1 as a function of D_{NN} is used to decide the D_{NN} cut for each technicolor mass point. This significance is roughly equal to the number of standard deviations of signal above the the error in the quantity signal+background. The denominator takes this form for two reasons: to prevent it from going to zero, which also tends to stabilize the results under small changes in the analysis. The other reason is that if the technicolor hypothesis were true, then the technicolor events would be mixed into the data sample as well, so those events are included in the denominator. Table 11.1 shows the results of this analysis when the discovery significance is used to determine the neural network cut for each mass point.

Another criterion for optimizing the D_{NN} cut is to minimize the expected 95% CL cross-section limit [32]:

$$\sigma_{95}^{expect}(D_{NN}) = \sigma_{TH} \times \frac{N_{95}(N_{bkg}) - N_{bkg}}{N_{signal}}, \quad (10.2)$$

where σ_{TH} is the cross-section \times branching ratio ($\sigma \times BR$) provided by technicolor theory, and N_{bkg} and N_{signal} are the numbers of background and signal events passing a D_{NN} cut. Once again, N_{bkg}

is computed using the tag-rate function. N_{signal} includes the $\sigma \times BR$, efficiency, acceptance, and luminosity information as discussed in Section 6, and shown in Table 8.2. $N_{95}(N_{bkg})$ is the expected 95% CL upper limit on the number of b -tagged events in the data, and is computed by the following method using various applications of the Poisson probability distribution:

$$N_{95}(N_{bkg}) = \sum_{k=0}^{\infty} \frac{N_{bkg}^k e^{-N_{bkg}}}{k!} N_{95}(k, N_{bkg}) \quad (10.3)$$

and, $N_{95}(k, N_{bkg})$ is the numerical solution for N in the equation below:

$$0.95 = 1 - \frac{\sum_{i=0}^k N^i e^{-N} / i!}{\sum_{i=0}^k N_{bkg}^i e^{-N_{bkg}} / i!}. \quad (10.4)$$

This method and the “discovery significance” method described above are strictly functions of the number of MC events and background events accepted for a given D_{NN} cut. The minimization of Equation 10.2 is the optimization method used to arrive at the D_{NN} cut in order to finally compute the 95% confidence upper limits of the technicolor $\sigma \times BR$ on the $M(\omega_T)$ & $M(\pi_T)$ mass plane.

In summary, we use two methods to determine the D_{NN} cut: maximizing the discovery significance or minimizing the expected 95% CL on the technicolor cross-section. The D_{NN} cut is recalculated based on these criteria and for each technicolor mass point. The plots in Figures 11.7 through 11.17 illustrate the optimization of D_{NN} for each neural network. The dotted line is a graph of $\sigma_{95}^{expected}$ (using the linear scale on the right side of each plot). The arrow shows where the D_{NN} cut was selected to minimize $\sigma_{95}^{expected}$ before computing the full 95% CL upper limit on the technicolor cross-section, as discussed in the next chapter.

11 RESULTS

Resonance peaks found in high-energy physics data are analogous to the discrete spectral lines observed in atomic emission spectrum experiments of the past. Because of the large binding energies involved in particle physics, the new resonance peaks correspond to new particles, rather than just excited states. This search has two goals: to search for technicolor particles by searching for peaks (excess events) in the data relative to the expected number of events. If no large signal is found, to compute the 95% confidence-level upper limits. In addition, other experimental searches for technicolor at CERN and Fermilab have seen no significant excesses, and have produced mass exclusion regions in technicolor parameter space. These results are summarized in Appendix B and in [33]. Notably, this analysis is the first to use neural networks to search for ω_T/ρ_T production.

The essential event selection criteria of this analysis have been the following:

- Exactly one photon that passes a standard $D\bar{O}$ identification
- Two or more jets, which pass standard jet ID
- One of those jets came from a b -quark, as indicated by a μ inside the jet “cone”
- A favorable value of the neural network discriminant, thus indicating an event in the data to resemble a technicolor event

With these requirements in place, excesses of data above background are compared to the expected number of technicolor events.

The Search

Table 11.1 contains a few instances of an excess in data one standard deviation (1σ) relative to expected background, where

$$P(\geq N_{obs}|b) = \sum_{n=N_{obs}}^{\infty} \int_0^{\infty} d\mu \frac{e^{-\mu} \mu^n}{n!} \frac{1}{\sqrt{(2\pi)\sigma_b}} e^{-(\mu-b)^2/2\sigma_b^2}, \quad (11.1)$$

where $P(\geq N_{obs}|b)$ is the probability of observing at least N_{obs} given the background b and error in the background σ_b . The parameter μ is used to integrate over the Gaussian probability distribution of the background for each value of $n \geq N_{obs}$ tried.

As seen in Table 11.1, the two searches showing excesses well above 1σ are the mass-points $M(\omega_T) = 160$ GeV, $M(\pi_T) = 40$ GeV, and $M(\omega_T) = 140$ GeV, $M(\pi_T) = 80$ GeV. Figures 11.3 through 11.6 show the neural network variables for technicolor, background, and data for these cases. Indeed, the excesses do show up where the neural networks are trained to look, *i.e.* where the signal events peak before applying the D_{NN} cut.

There are no excesses above 2σ of data above the background calculation over the technicolor phase-space evaluated in this analysis. We now pursue an upper bound on the theoretical $\sigma \times BR$ that is allowed for each technicolor mass point.

The Method for Computing the Technicolor Cross-Section Limits

The 95% confidence level upper limits on ω_T/ρ_T^0 production are each computed by numerically solving the integral equation for σ_{ul} [1, 30]:

$$0.95 = \int_0^{\sigma_{ul}} \rho(\sigma|k, I) d\sigma \quad (11.2)$$

where σ_{ul} is the cross-section (a branching ratio may be included) limit, ρ is the posterior probability density that is explained later, k is the number of b -tagged events in the data passing all selection and neural network cuts, and I is the “prior” information. The prior information includes the errors on the signal, background, and luminosity as well as the gaussian probability distributions used to describe those errors. The notation for $\rho(\sigma|k, I)$ reads “the probability density of σ given k data events, and the prior information, I .” For notational brevity, I use σ interchangeably with $\sigma \times BR$, but ultimately, the upper limit on $\sigma \times BR$ is computed.

The probability density $\rho(\sigma|k, I)$ is not yet known, and its computation is not entirely obvious. Now, using the Poisson distribution, the probability

$$P(k|\mu) = \frac{e^{-\mu} \mu^k}{k!} \quad (11.3)$$

is the probability of measuring k events in the data, given a predicted mean, μ , where the mean is given

by

$$\mu = b + \sigma\epsilon L, \quad (11.4)$$

where the variable b is the background, σ is the technicolor cross-section, ϵ is the technicolor acceptance, and L is the integrated luminosity taken during DØ Run I. So, in effect, μ is the mean number of data events expected if the technicolor hypothesis ($\sigma > 0$) were true. The probability, P , now becomes

$$P(k|\sigma, b, L, \epsilon) = \frac{e^{-(b+\sigma\epsilon L)}(b + \sigma\epsilon L)^k}{k!} \quad (11.5)$$

The immediate goal, however, is to compute $\rho(\sigma, b, L, \epsilon|k)$, so Bayes' theorem is applied to accomplish this. In effect, the Poisson probability in equation 11.5 must be “inverted” to give us a function of cross-section *given* a measurement of k events in the data. In terms of generic propositions A, B , and C , Bayes' theorem states:

$$P(A|BC) = \frac{P(B|AC)P(A|C)}{P(B|C)}, \quad (11.6)$$

and allows just such an inversion of the arguments. By inspection, the substitutions for A, B , and C are the following:

- $A \equiv$ the cross-section is between σ and $\sigma + d\sigma$, the integrated luminosity is between L and $L + dL$, the signal efficiency is between ϵ and $\epsilon + d\epsilon$, and the background is between b and $b + db$.
- $B \equiv k$ events are observed in the data
- $C \equiv$ all other prior knowledge, I : The assumption that the errors in b , ϵ , and L are gaussian, and the “flat prior” for σ is assumed. The flat prior means that a uniform probability distribution is assigned to the initial distribution in σ and represents the fact that no particular mean value of σ is expected *a priori*.

Inserting this information into Bayes' theorem gives the probability density with respect to σ :

$$\rho(\sigma, b, L, \epsilon|k, I) \propto P(k|\sigma, b, L, \epsilon, I) \{ \rho(\sigma|I) P(L|I) P(\epsilon|I) P(b|I) \}, \quad (11.7)$$

The normalization condition

$$\int_0^\infty db \int_0^\infty dL \int_0^1 d\epsilon \int_0^\infty \rho(\sigma, b, L, \epsilon | k, I) d\sigma = 1 \quad (11.8)$$

fixes the denominator term, $P(k|I)$, required by Bayes' theorem. It is assumed that the quantities σ, L, ϵ , and b are independent, and so are the respective probability distributions. The integrals are over the appropriate Gaussian distributions. For the cross-section, the flat prior is used to introduce the probability density with respect to σ :

$$\rho(\sigma|I) = \begin{cases} 1/\sigma_{max} & \text{if } 0 \leq \sigma \leq \sigma_{max} \\ 0 & \text{otherwise.} \end{cases} \quad (11.9)$$

where σ_{max} is chosen sufficiently large that it has no effect on the final probability distribution or the cross-section limit. The other three probabilities use the Gaussian probability distribution:

$$P(x|I) = \begin{cases} \frac{1}{\sigma_x \sqrt{2\pi}} e^{-\frac{(x-\bar{x})^2}{2\sigma^2}} & \text{if } x > 0 \\ 0 & \text{if } x \leq 0. \end{cases} \quad (11.10)$$

where x stands for L, b , or ϵ , and σ_x is the corresponding error in each quantity.

Finally, the integral over the “nuisance parameters” L, ϵ , and b gives the final probability density:

$$\rho(\sigma|k, I) = \int_0^\infty dL \int_0^1 d\epsilon \int_0^\infty db \rho(\sigma, b, L, \epsilon | k, I). \quad (11.11)$$

Equation 11.2 is now used to compute the upper limit to the cross-section.

Technicolor 95% cross-section limits

The method for computing the actual value of $\sigma \times BR_{95\%CL}$ is now applied. The inputs to the program used by the searches at DØ provided by [31], are the following:

1. $\epsilon_{signal}, \delta\epsilon_{signal}$
2. $N_{bkg}, \delta N_{bkg}$
3. N_{data}

4. $\int \mathcal{L} dt$ and $\delta \int \mathcal{L} dt$, where the current values being used are $105.0 \pm 6.0 \text{ pb}^{-1}$ according to the DØ luminosity data-base.

Table 11.2 shows the limits calculated for each Technipion and Techniomega mass.

Three Technicolor mass points have been excluded at the 95% CL. They are:

- $M(\omega_T) = 160 \text{ GeV}, M(\pi_T) = 80 \text{ GeV}$ at 9.15 pb
with $\sigma \times BR_{TH} = 11.89 \text{ pb}$
- $M(\omega_T) = 180 \text{ GeV}, M(\pi_T) = 100 \text{ GeV}$ at 5.03 pb
with $\sigma \times BR_{TH} = 7.57 \text{ pb}$
- $M(\omega_T) = 200 \text{ GeV}, M(\pi_T) = 120 \text{ GeV}$ at 4.39 pb
with $\sigma \times BR_{TH} = 4.88 \text{ pb}$

Figure 11.1 shows log plots of the five variables used in training the neural networks from one of the excluded technicolor mass points $M(\omega_T) = 160 \text{ GeV}, M(\pi_T) = 80 \text{ GeV}$. All analysis cuts are applied except for the neural network cut for the left-hand plots, and after the NN cut for the right-hand plots. One can see here that the neural network cut is very effective in eliminating background while keeping a large fraction of technicolor events.

To give a better idea of how the sensitivity of the limits change with mass, the 90% CL exclusions are computed as well:

- $M(\omega_T) = 140 \text{ GeV}, M(\pi_T) = 100 \text{ GeV}$ at 7.99 pb
with $\sigma \times BR_{TH} = 8.59 \text{ pb}$
- $M(\omega_T) = 180 \text{ GeV}, M(\pi_T) = 80 \text{ GeV}$ at 3.43 pb
with $\sigma \times BR_{TH} = 4.19 \text{ pb}$
- $M(\omega_T) = 200 \text{ GeV}, M(\pi_T) = 60 \text{ GeV}$ at 2.44 pb
with $\sigma \times BR_{TH} = 2.62 \text{ pb}$

The 90% and 95% CL excluded points are adjacent on the $M(\omega_T)$ vs. $M(\pi_T)$ mass plane. The sensitivity of the analysis increased with $M(\omega_T)$ and $M(\pi_T)$. In other words, the neural network acceptance got a little better for high masses (see Table 8.2). However, the cross-section plummeted with $M(\omega_T)$, thus limiting our ability to exclude Technicolor to a 60 GeV-wide region.

Table 11.1 Results of choosing the D_{NN} cut based on the discovery significance, $S/\sqrt{S+B}$. The σ deviation is given for the cases where the number of b -tagged data events exceeds the background calculation.

Masses (GeV)		D_{NN} cut	Expected Events			$P(\geq N_{obs} b)$	σ dev.
$M(\omega_T)$	$M(\pi_T)$		MC	Obs	Bkg		
140	40	0.810	3.57	11	9.44 ± 1.15	0.352300	0.38
140	60	0.880	3.16	3	3.83 ± 0.46	0.727200	
140	80	0.730	11.28	31	22.55 ± 2.62	0.077310	1.42
140	100	0.830	6.45	10	12.86 ± 1.48	0.803600	
160	40	0.970	3.44	5	1.89 ± 0.26	0.046160	1.69
160	60	0.930	2.80	3	4.26 ± 0.52	0.788200	
160	80	0.790	9.85	11	15.67 ± 1.89	0.886200	
160	100	0.840	10.15	22	16.95 ± 2.07	0.160800	0.99
180	40	0.960	3.78	4	2.10 ± 0.31	0.165000	0.97
180	60	0.910	3.46	4	6.07 ± 0.76	0.843000	
180	80	0.910	4.32	3	8.62 ± 1.07	0.988100	
180	100	0.770	13.27	14	18.29 ± 2.28	0.838700	
180	120	0.850	8.11	19	17.71 ± 2.20	0.415100	0.21
200	20	0.880	1.19	14	14.95 ± 2.06	0.610800	
200	40	0.960	2.10	4	2.33 ± 0.35	0.210500	0.81
200	60	0.950	2.57	0	3.38 ± 0.46	1.000000	
200	80	0.890	3.21	3	9.25 ± 1.21	0.992000	
200	100	0.890	6.84	13	12.69 ± 1.61	0.496800	0.01
200	120	0.880	7.80	10	12.49 ± 1.61	0.772000	
210	90	0.880	3.64	12	13.31 ± 1.71	0.656700	
210	110	0.800	6.96	22	20.47 ± 2.60	0.404200	0.24
220	60	0.940	2.22	0	2.88 ± 0.41	1.000000	
220	80	0.900	3.62	10	17.20 ± 2.27	0.959300	
220	100	0.950	2.85	4	4.82 ± 0.68	0.696700	
220	120	0.820	5.32	16	14.00 ± 1.82	0.341400	0.41
260	60	0.950	2.17	4	7.17 ± 0.98	0.913200	
260	100	0.960	1.88	6	7.32 ± 1.03	0.720700	
280	40	0.970	1.29	4	6.07 ± 0.86	0.839100	
280	120	0.840	2.16	13	14.77 ± 2.01	0.684800	
300	40	0.980	0.67	6	5.02 ± 0.74	0.388500	0.29
300	80	0.980	1.33	6	5.67 ± 0.79	0.494300	0.02
300	140	0.970	1.53	4	5.47 ± 0.76	0.780300	

Table 11.2 Results summary of $\sigma \times BR$ limits at the 95% confidence level. The D_{NN} cut was selected by minimizing the *expected* 95% CL, which is a calculation based only on signal and background events as a function of D_{NN} ($S(D_{NN})$ and $B(D_{NN})$).

Masses (GeV)		$\sigma \times BR(pb)$			D_{NN}	Expected Events		
$M(\omega_T)$	$M(\pi_T)$	Theo.	90% CL	95% CL	cut	MC	Obs	Bkg
140	40	9.53	22.78	27.41	0.830	3.39	10	8.51 ± 1.03
140	60	9.13	12.60	15.88	0.880	3.16	3	3.83 ± 0.46
140	80	15.62	20.82	24.67	0.810	9.03	17	12.92 ± 1.50
140	100	8.59	7.99	9.79	0.830	6.45	10	12.86 ± 1.48
160	40	5.86	13.10	15.40	0.970	3.44	5	1.89 ± 0.26
160	60	5.81	11.12	13.83	0.940	2.42	3	3.11 ± 0.38
160	80	11.89	7.16	9.15	0.830	8.53	8	11.73 ± 1.42
160	100	9.42	12.68	14.89	0.840	10.15	22	16.95 ± 2.07
180	40	3.92	6.49	7.62	0.960	3.78	4	2.10 ± 0.31
180	60	3.84	4.72	5.96	0.910	3.46	4	6.08 ± 0.76
180	80	4.19	3.43	4.31	0.910	4.33	3	8.62 ± 1.07
180	100	7.57	4.10	5.03	0.780	12.99	14	17.37 ± 2.17
180	120	5.79	6.99	8.39	0.870	7.62	16	15.23 ± 1.92
200	20	2.75	18.52	22.64	0.880	1.19	14	14.95 ± 2.07
200	40	2.71	7.97	9.45	0.960	2.10	4	2.33 ± 0.35
200	60	2.62	2.44	2.99	0.940	2.82	0	4.39 ± 0.59
200	80	2.71	2.92	3.68	0.890	3.21	3	9.25 ± 1.21
200	100	4.05	4.96	6.10	0.920	6.00	10	9.35 ± 1.21
200	120	4.88	3.49	4.39	0.890	7.41	8	11.21 ± 1.46
210	90	2.35	4.62	5.72	0.880	3.64	12	13.31 ± 1.71
210	110	3.41	4.65	5.56	0.820	6.65	18	18.60 ± 2.37
220	60	1.90	2.16	2.71	0.940	2.22	0	2.88 ± 0.41
220	80	1.87	3.90	4.87	0.710	4.54	25	29.13 ± 3.81
220	100	2.10	3.44	4.26	0.950	2.84	4	4.82 ± 0.68
220	120	2.83	5.20	6.33	0.820	5.33	16	14.00 ± 1.82
260	60	1.06	2.00	2.50	0.950	2.17	4	7.17 ± 0.98
260	100	1.02	2.41	3.05	0.930	2.14	7	10.07 ± 1.37
280	40	0.85	2.90	3.64	0.970	1.29	4	6.07 ± 0.86
280	120	0.81	2.61	3.21	0.850	2.12	12	14.53 ± 1.98
300	40	0.67	5.88	7.00	0.970	0.70	6	5.56 ± 0.81
300	80	0.61	2.01	2.51	0.990	1.21	3	4.69 ± 0.67
300	140	0.67	1.76	2.20	0.960	1.62	4	6.24 ± 0.86

An Excluded Technicolor Mass Point

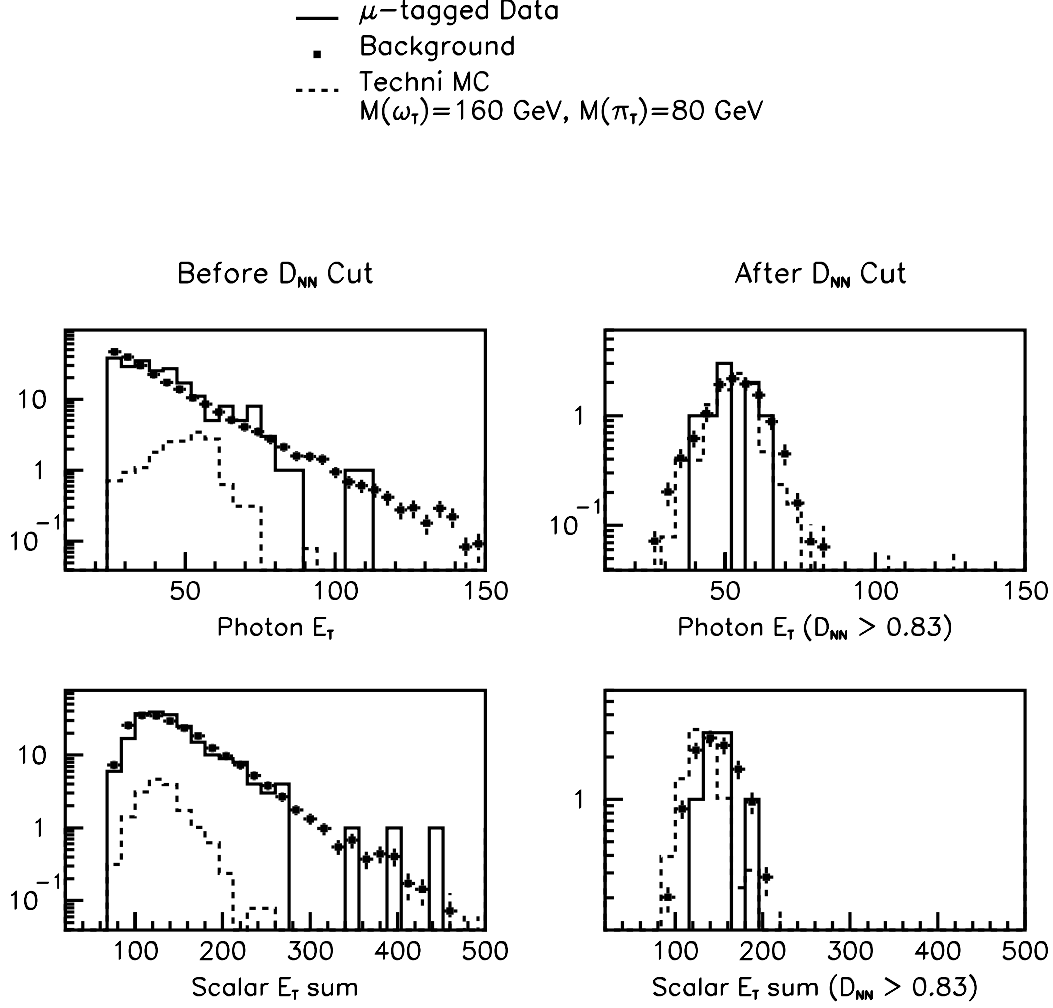


Figure 11.1 Shown in this and in the following figure are the observables used in training the neural networks. The dashed-line signal is normalized to $L = 105 \text{ pb}^{-1}$, and corresponds to one of the mass points that has been *excluded*. The left side plots correspond to data, background, and technicolor events passing event selection cuts. Each plot on the right side shows the sub-sample of events passing an optimal D_{NN} cut. The NN was trained on the shown signal, and the NN response to the signal in the right-hand plots is consistent. The cut of $D_{NN} \geq 0.83$ was selected to minimize the expected 95% confidence limit. See Figure 11.9 for the D_{NN} spectrum in this case.

An Excluded Technicolor Mass Point

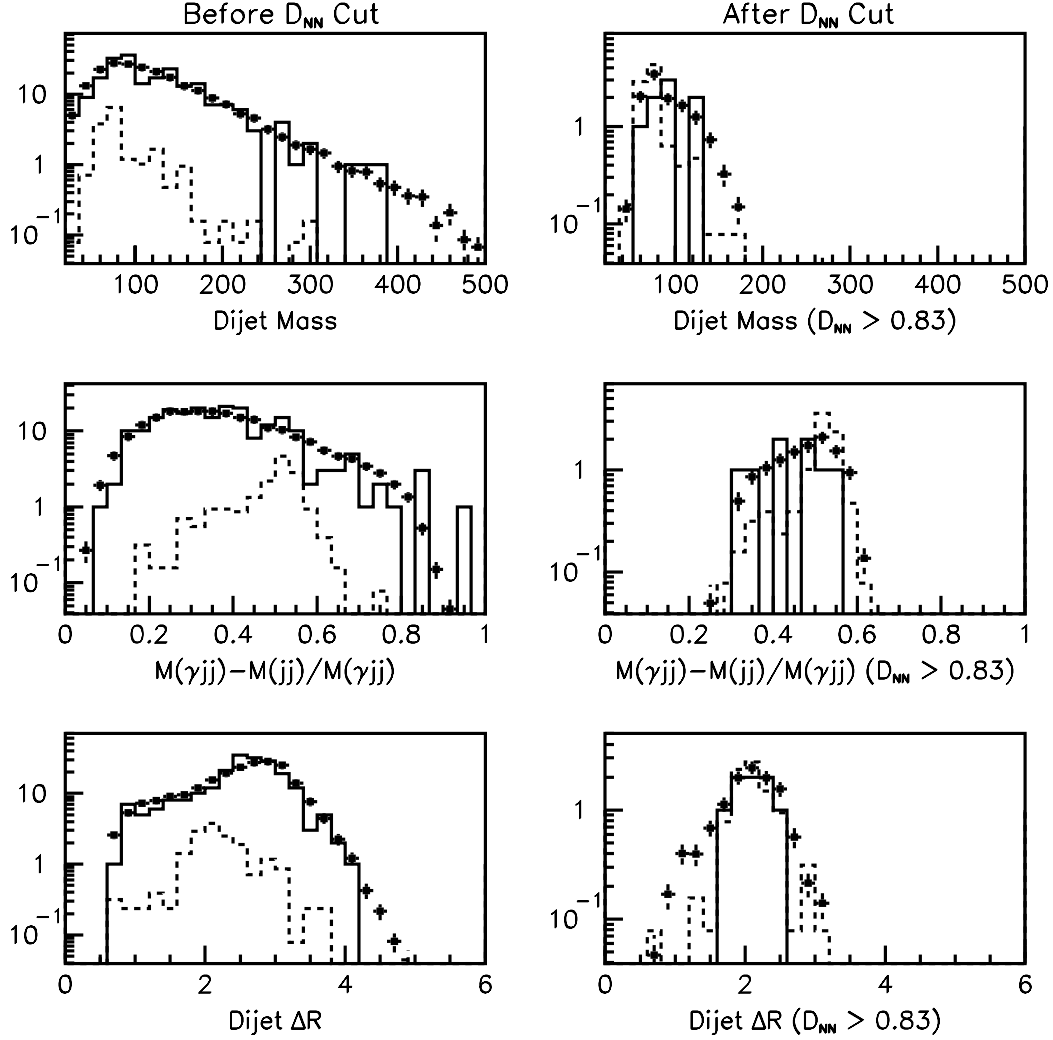


Figure 11.2 Shown are the remaining neural network variables continued from the previous page. This also shows before and after the optimal D_{NN} cut for the technicolor mass point $M(\omega_T) = 160$ GeV, and $M(\pi_T) = 80$ GeV. This mass point has been excluded at the 95% CL. See Figure 11.9 for the D_{NN} spectrum in this case.

A 1.4σ Excess of Events in Data

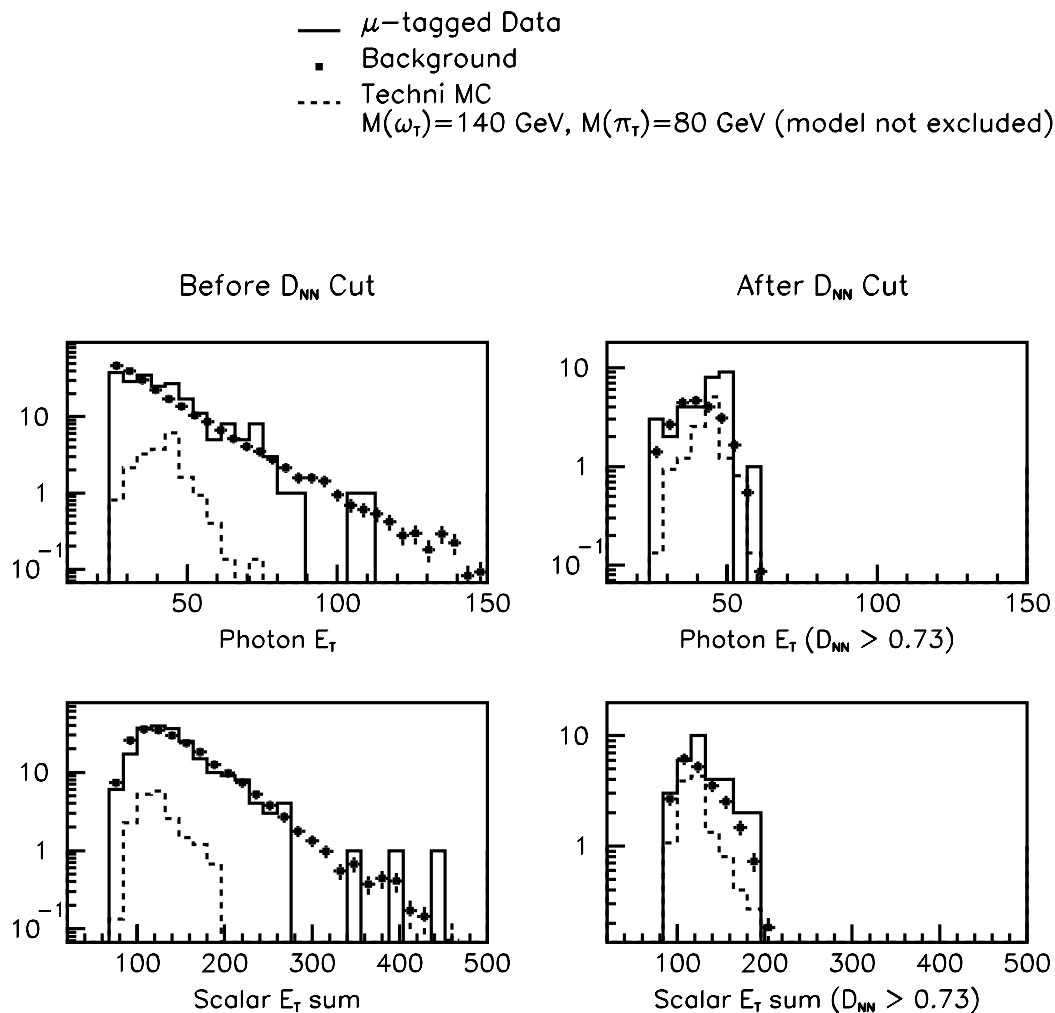


Figure 11.3 This case shown is for $M(\omega_T) = 140$, $M(\pi_T) = 80$ GeV, which is one of the mass-points having an excess of data over background. See Table 11.1 for the results of this case. Here also, the right-hand plots use a D_{NN} cut optimized to maximize the discovery significance formula, $S/\sqrt{S+B}$ as discussed in Chapter 10. See Figure 11.8 for the D_{NN} spectrum in this case.

A 1.4σ Excess of Events in Data

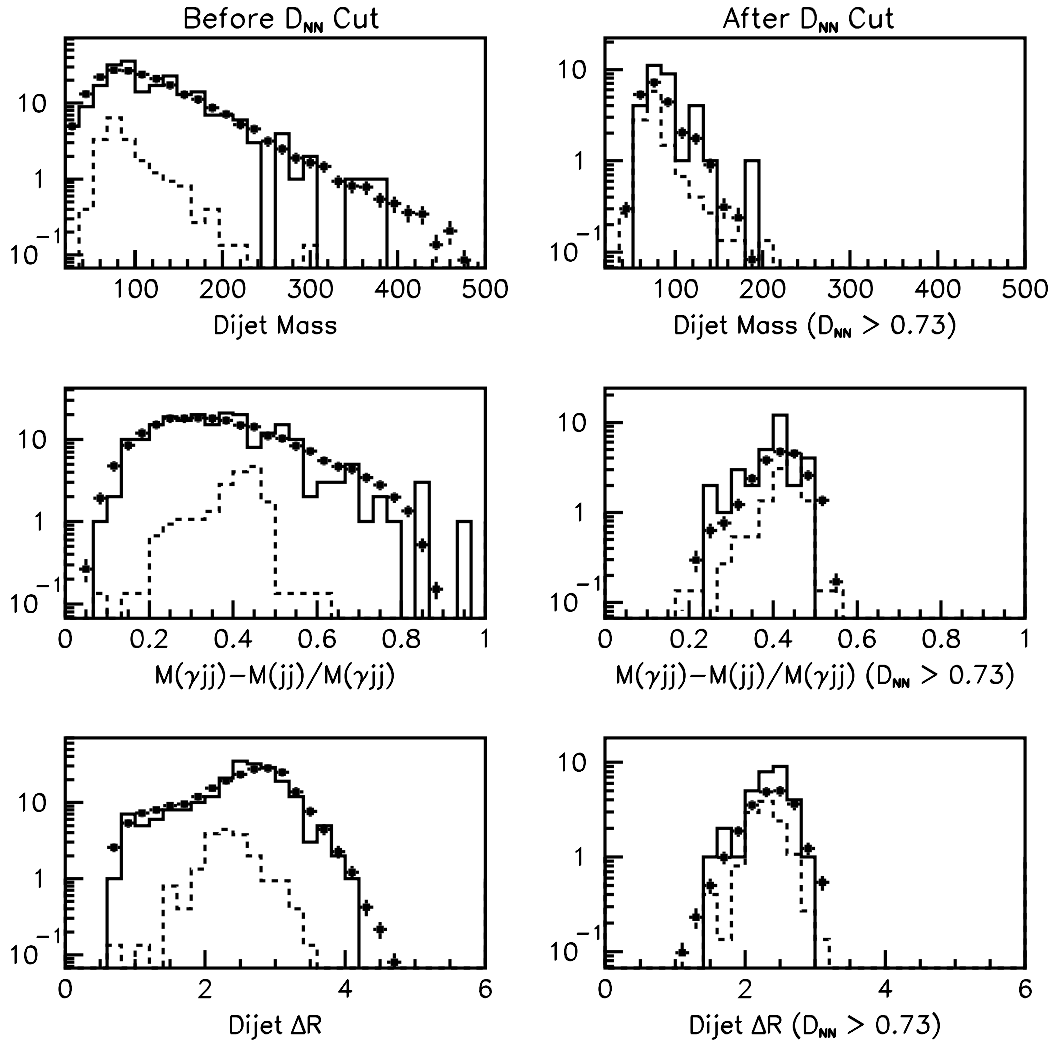


Figure 11.4 Continued from 11.3. See Figure 11.8 for the D_{NN} spectrum in this case.

A 1.7σ Excess of Events in Data

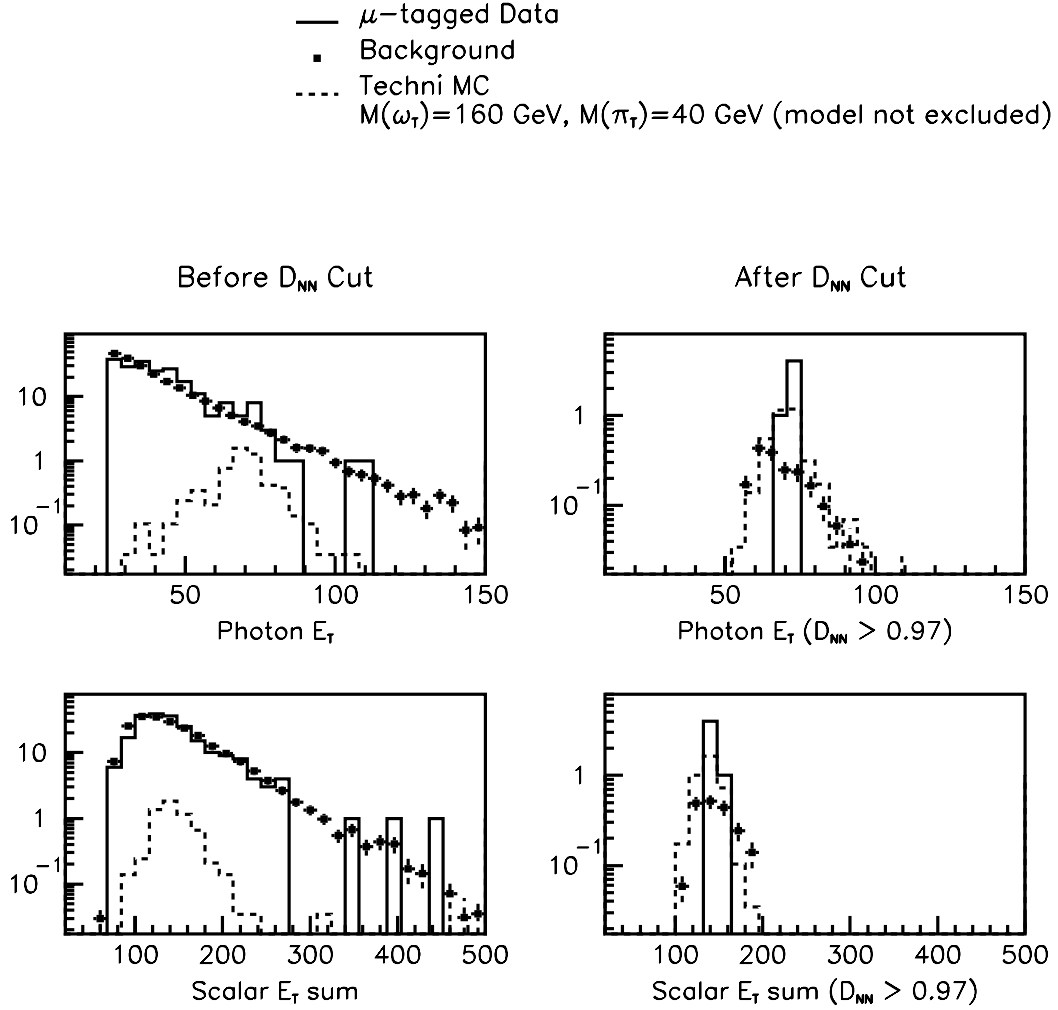


Figure 11.5 The case shown is for $M(\omega_T) = 160, M(\pi_T) = 40$ GeV, which is one of the mass-points having an excess of data over background. Also, see Table 11.1. Here also, the D_{NN} cut for the right-hand plots is set to maximize the discovery significance formula $S/\sqrt{S+B}$. See Figure 11.8 for the D_{NN} spectrum in this case.

A 1.7σ Excess of Events in Data

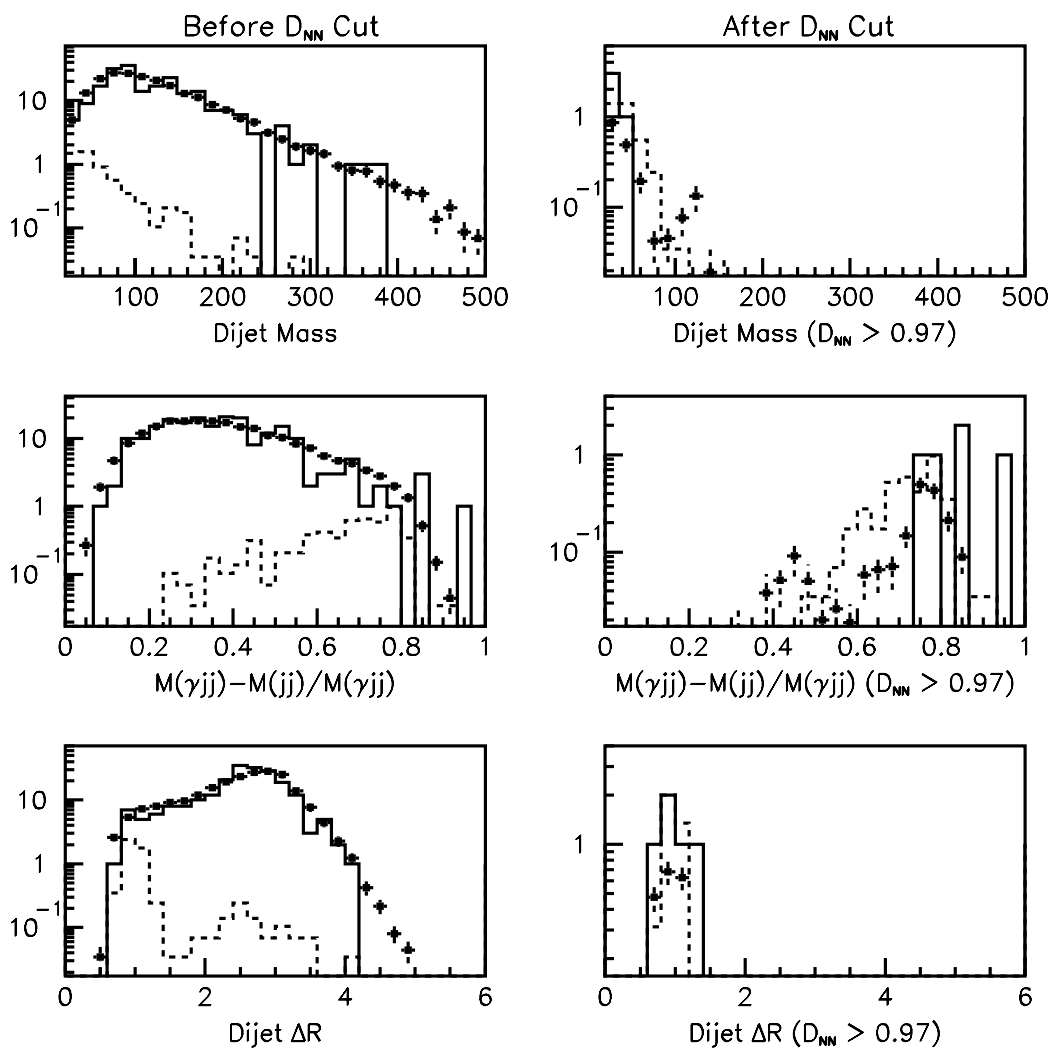


Figure 11.6 Continued from 11.5. See Figure 11.8 for the D_{NN} spectrum in this case.

Key to Results plots:

- Technicolor Signal
 - - - - - Background (tag-rate)
 Expected 95% CL (linear scale)
 minimized to select D_{NN} cut

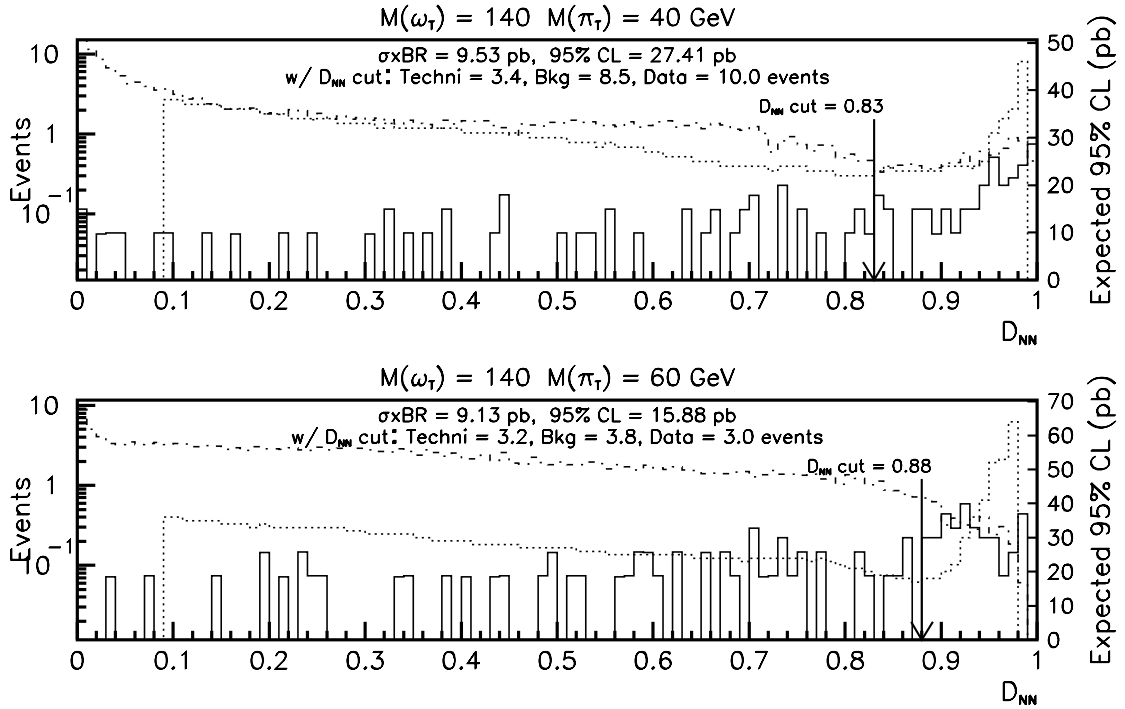


Figure 11.7 Optimization results. These plots and the ones that follow illustrate the selection of the neural network discriminant (D_{NN}) cut for every technicolor mass point in this analysis by finding the minimum *expected* 95% CL (dependent only on the technicolor and background acceptances). Also shown on each plot are the 95% CL, $\sigma \times BR$, and number of accepted technicolor, data, and background events passing all cuts including the D_{NN} cut. If the 95% CL shown is less than the $\sigma \times BR$ for a mass point, then this mass point is considered to be excluded. The numbers shown are the same as in Table 11.2.

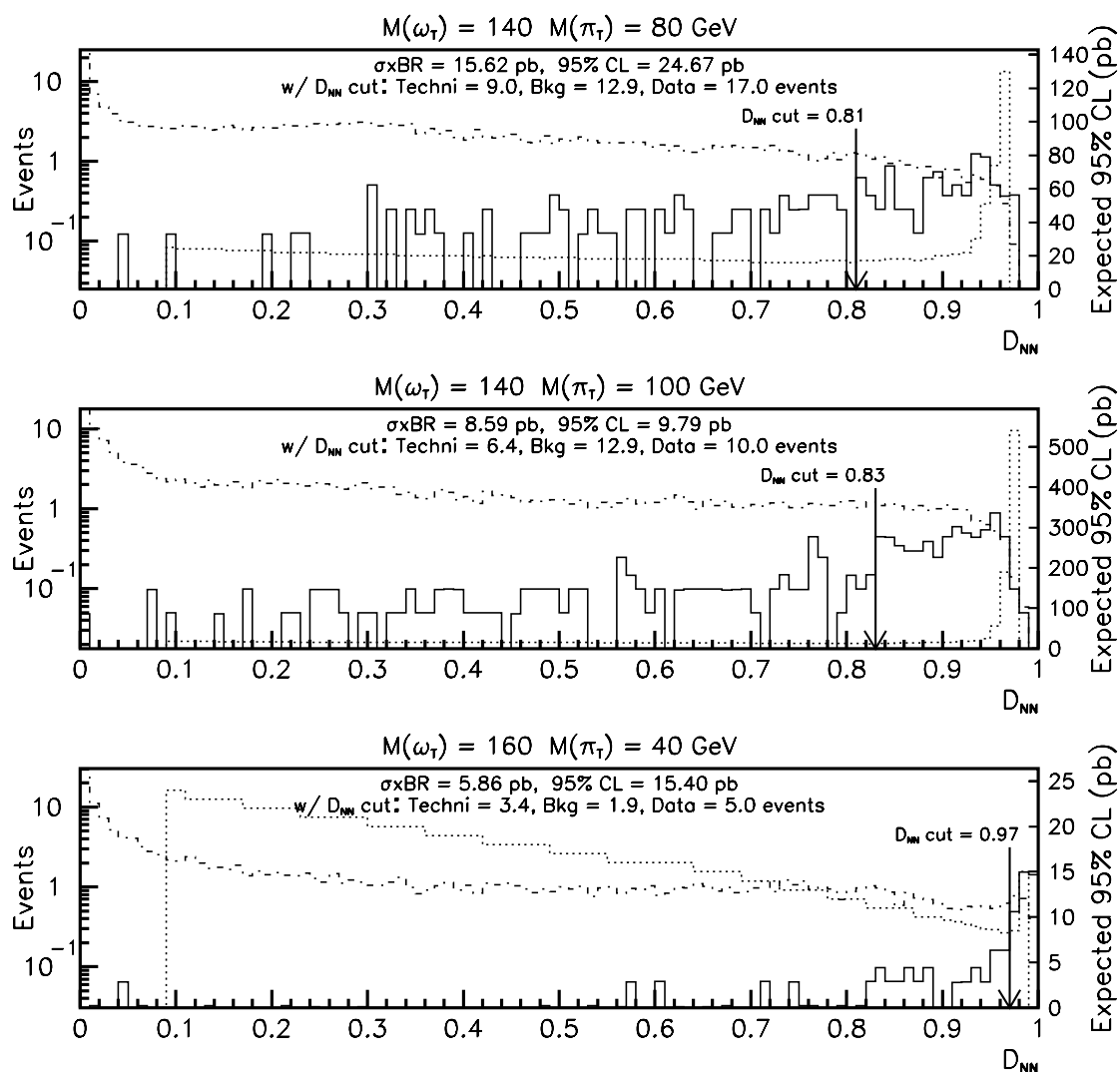


Figure 11.8 Optimization results continued. Compare with Table 11.2.

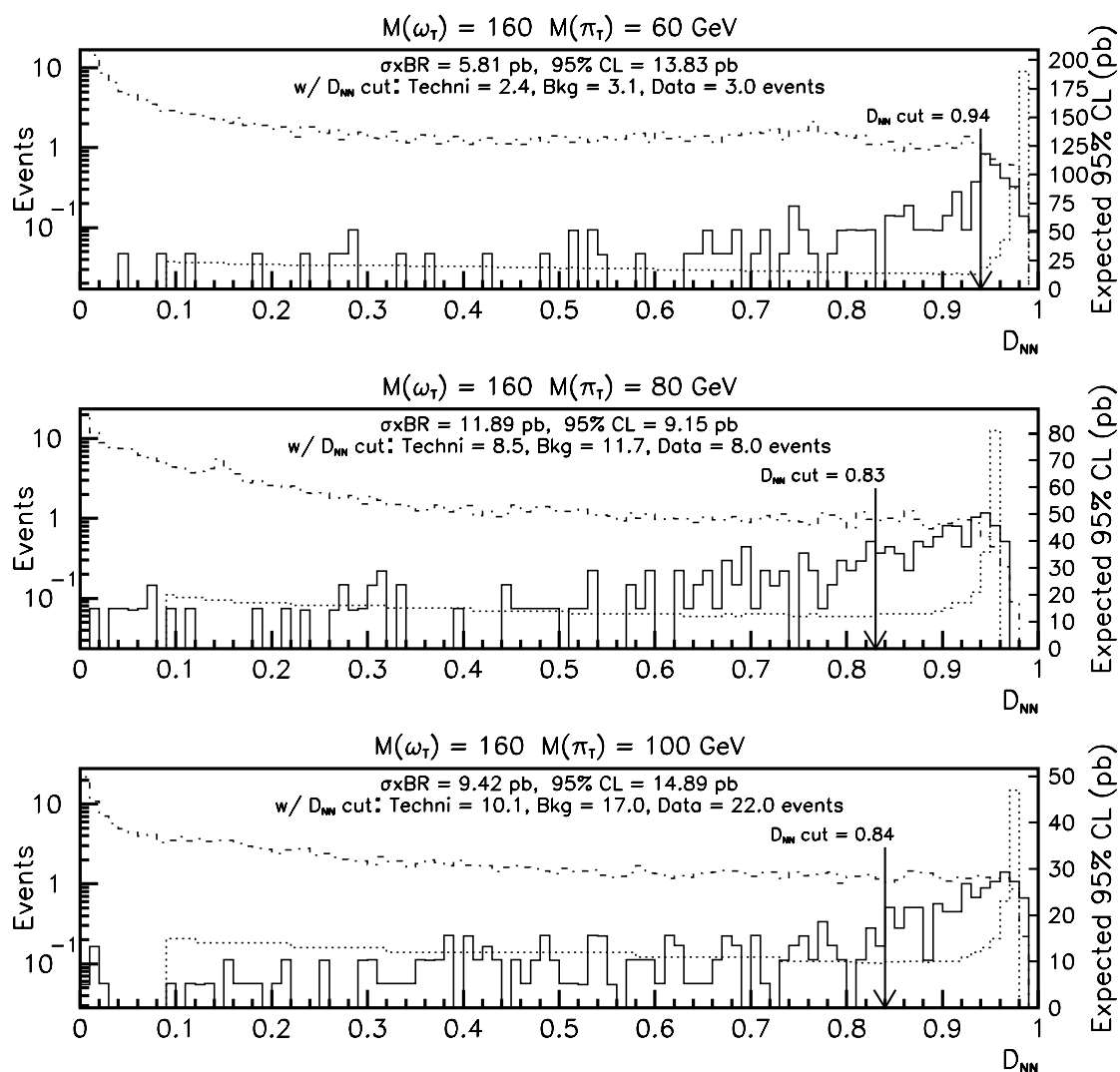


Figure 11.9 Optimization results continued. Compare with Table 11.2.

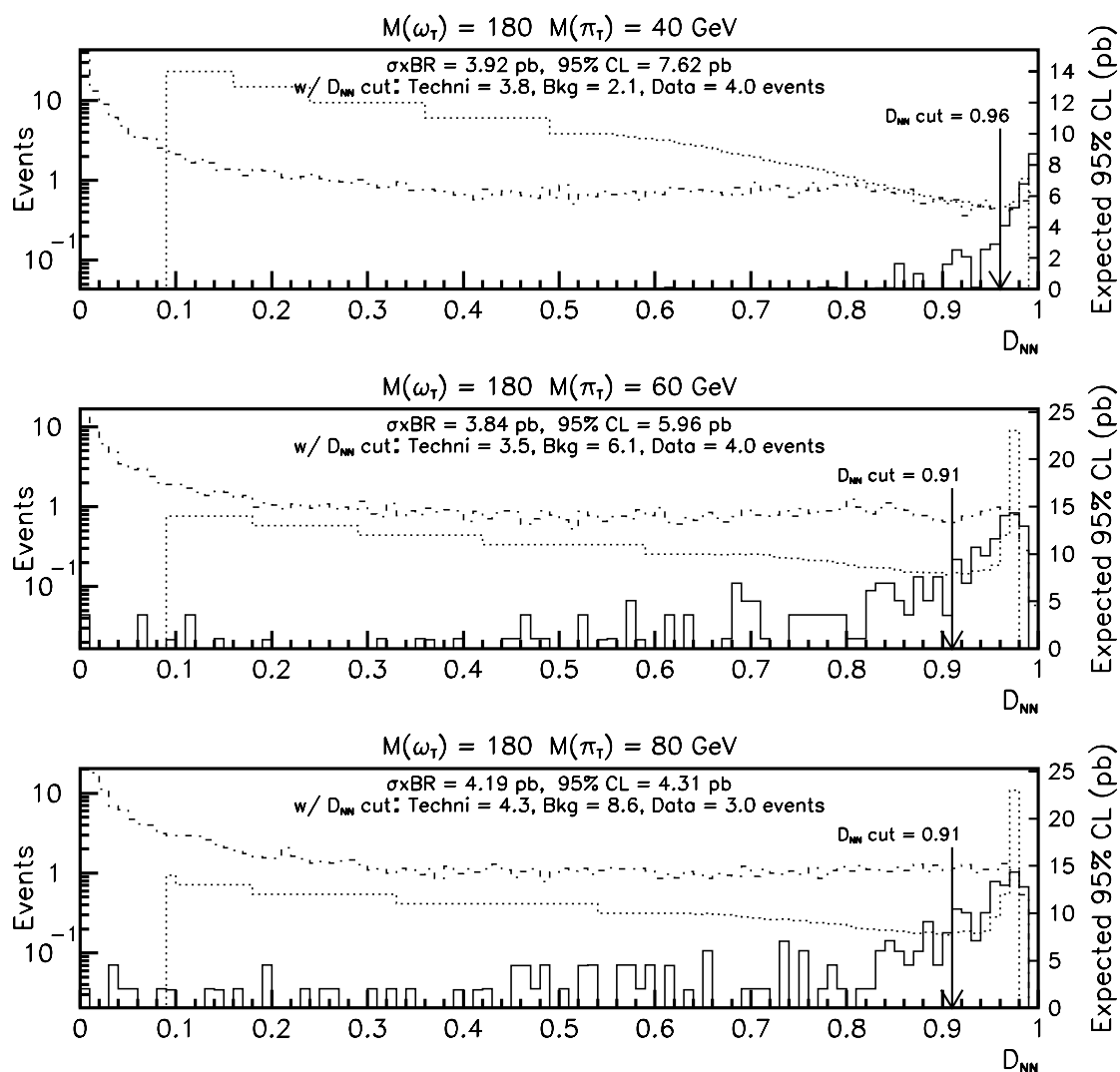


Figure 11.10 Optimization results continued. Compare with Table 11.2.

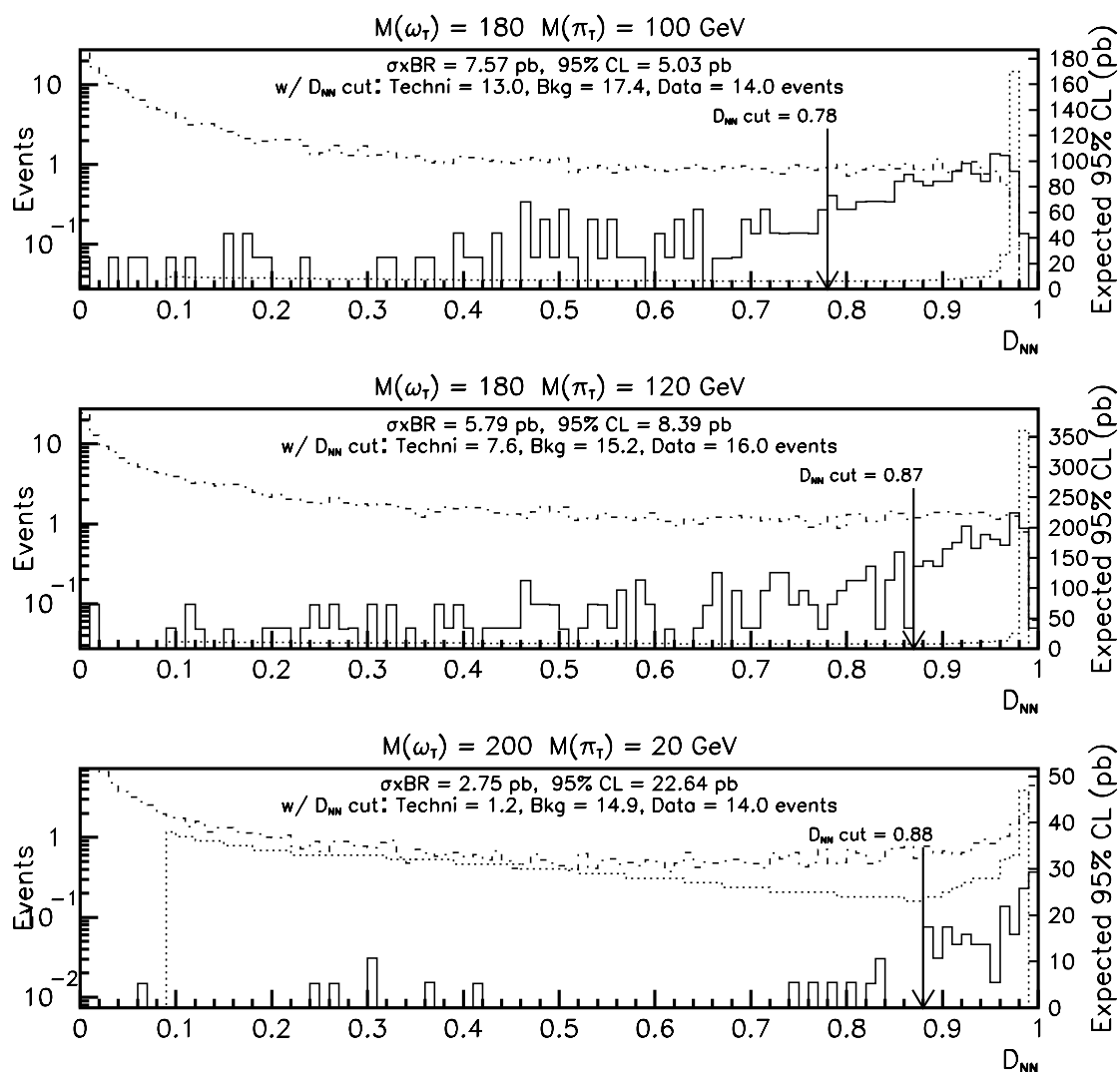


Figure 11.11 Optimization results continued. Compare with Table 11.2.

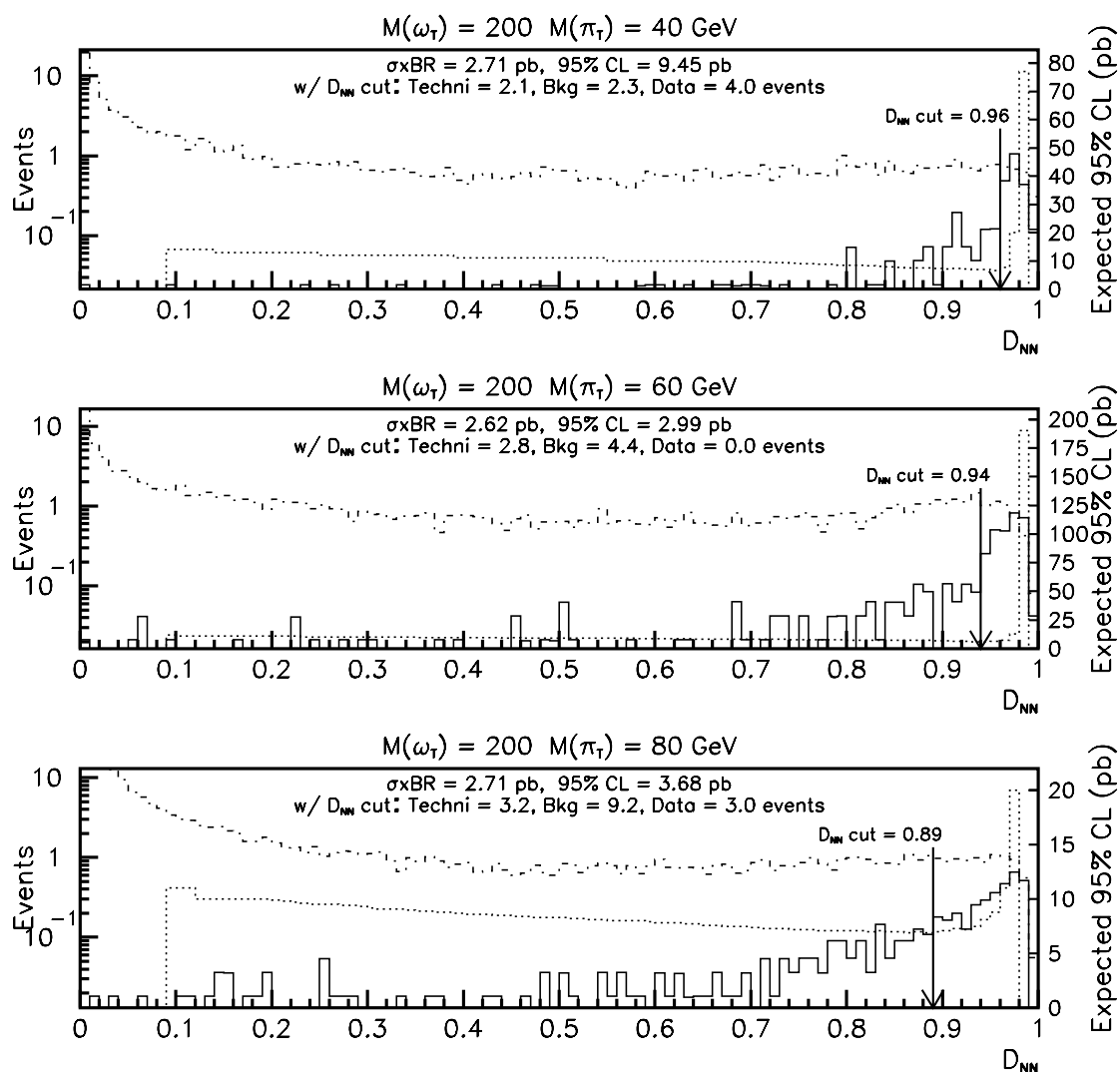


Figure 11.12 Optimization results continued. Compare with Table 11.2.

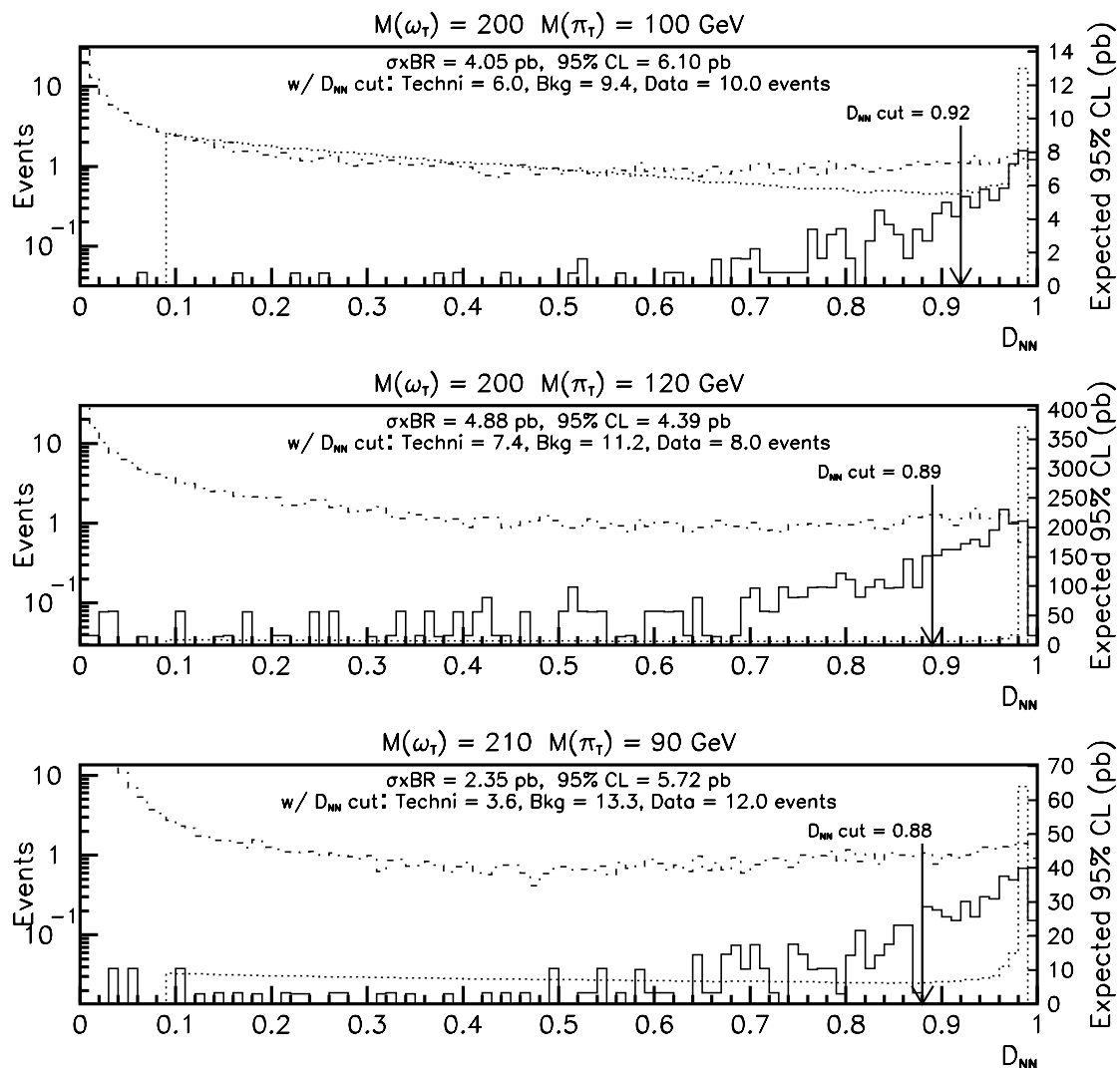


Figure 11.13 Optimization results continued. Compare with Table 11.2.

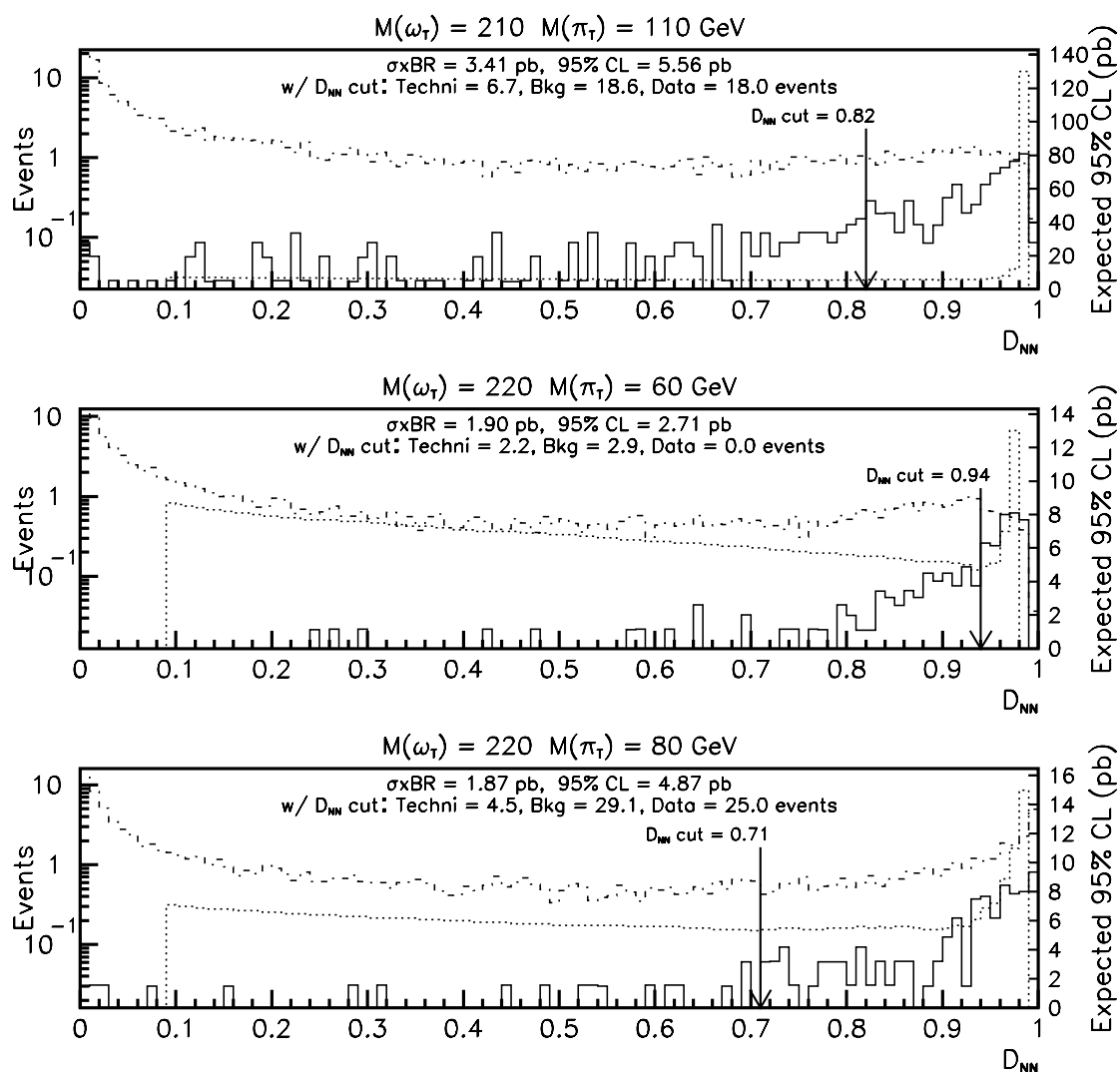


Figure 11.14 Optimization results continued. Compare with Table 11.2.

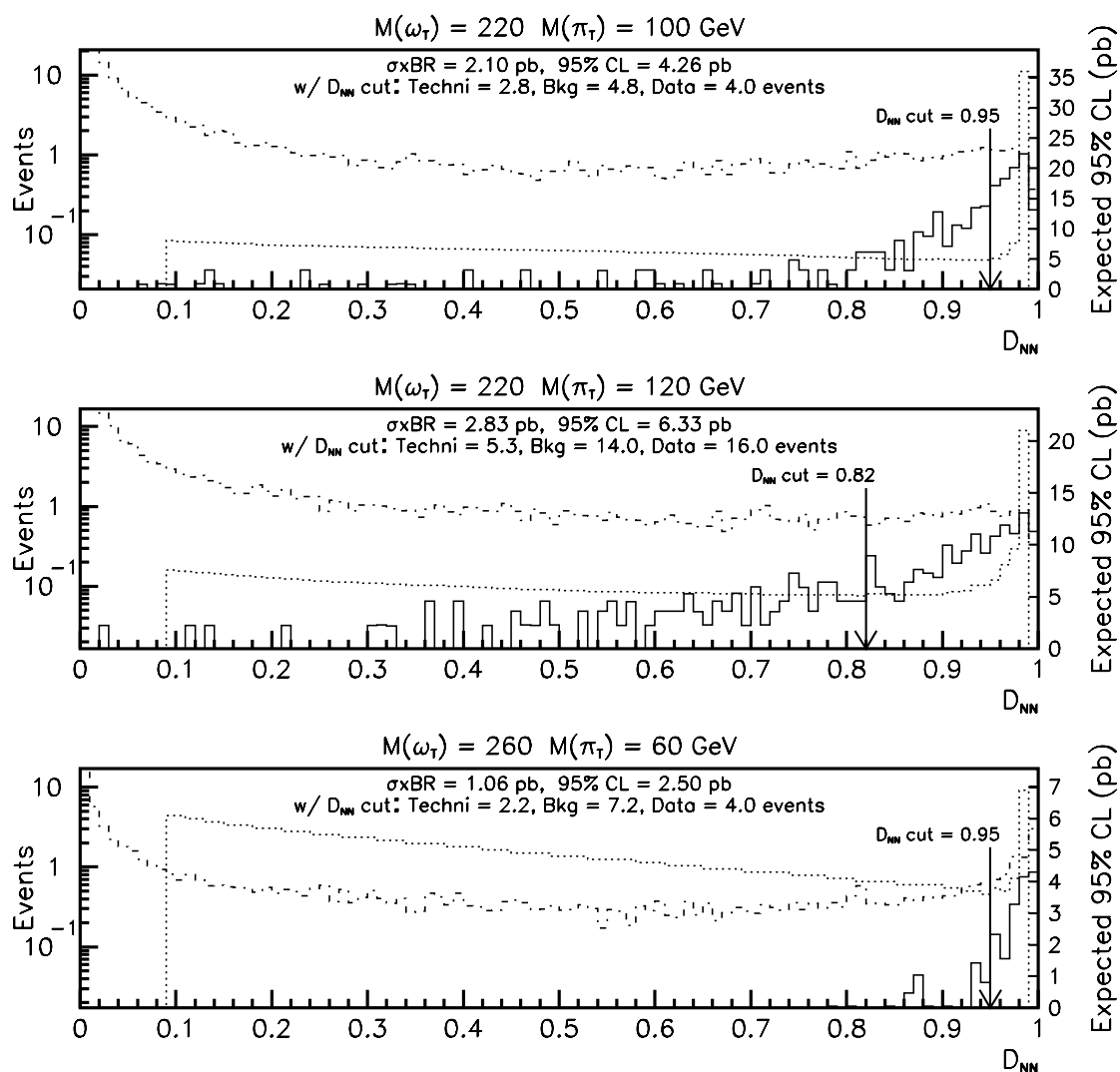


Figure 11.15 Optimization results continued. Compare with Table 11.2.

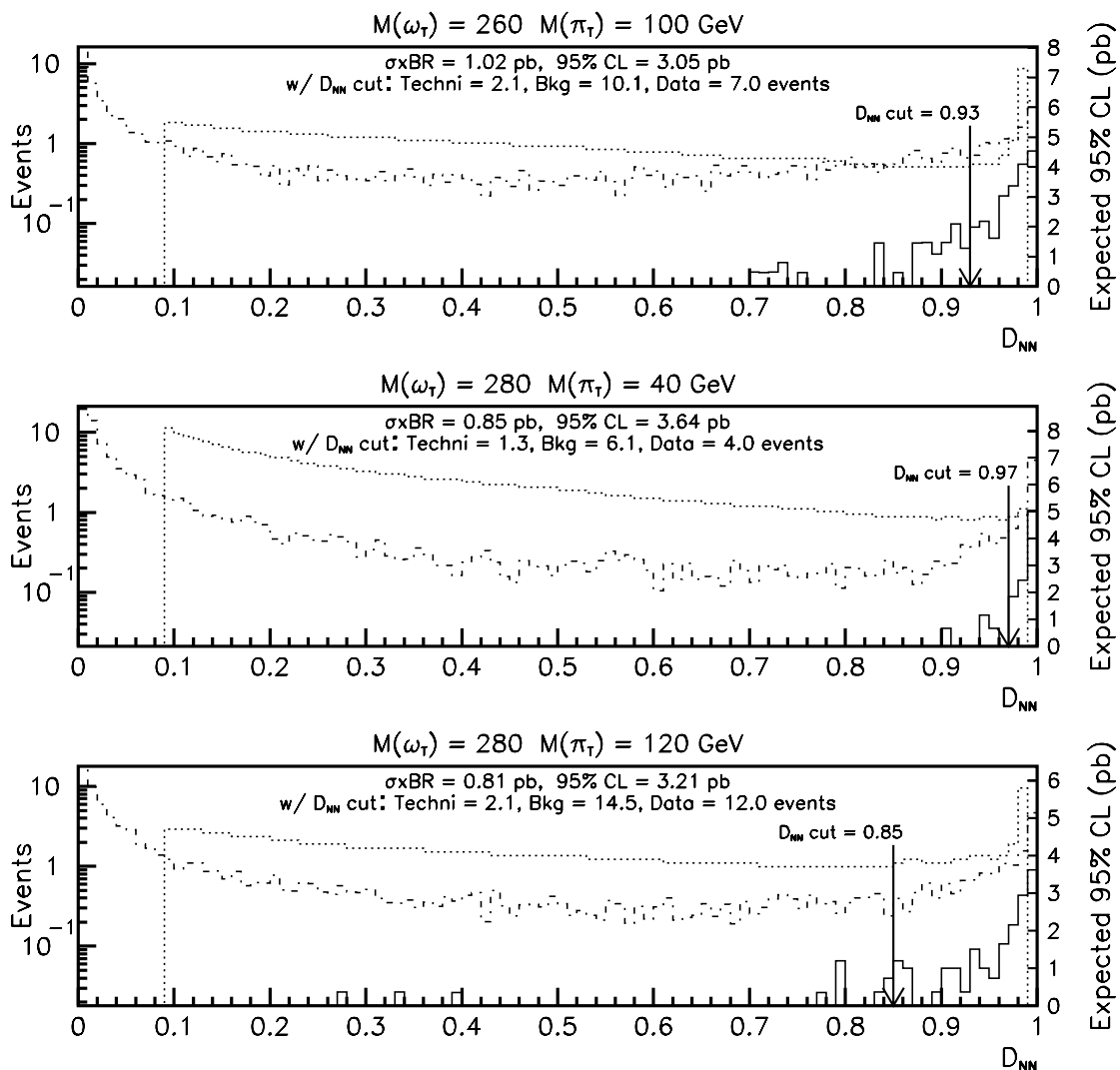


Figure 11.16 Optimization results continued. Compare with Table 11.2.

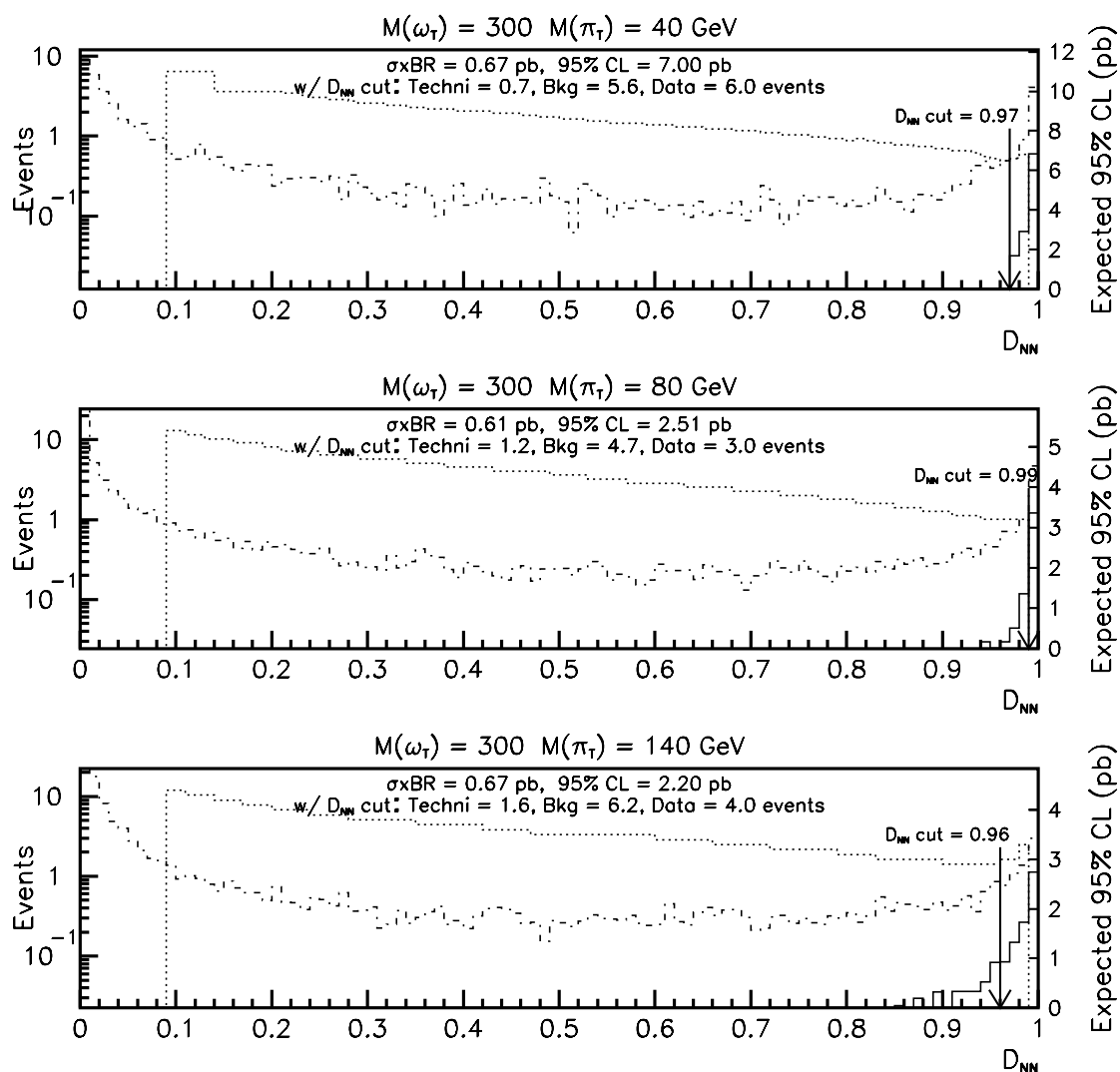


Figure 11.17 Optimization results continued. Compare with Table 11.2.

APPENDIX A PYTHIA PARAMETERS USED TO GENERATE TECHNICOLOR EVENTS

The following are the parameters used in PYTHIA 6.126 to generate the technicolor events and cross-sections [5, 6]. In parenthesis are the PYTHIA variable names:

- Process selection:

$$f + \bar{f} \rightarrow \gamma \pi_T^0 \text{ (MSUB(364)=1)}$$

$$f + \bar{f} \rightarrow \gamma \pi_T^{0'} \text{ (MSUB(365)=1)}$$

- π_T^0 and $\pi_T^{0'}$ assumed degenerate, so when setting the π_T mass, both were set to the same value.

For example, for the case $M(\pi_T) = 100 \text{ GeV}$,

$$\text{(PMAS(51,1)=PMAS(53,1)=100.0)}$$

- ω_T and ρ_T^0 also assumed degenerate. For the case $M(\omega_T) = 200 \text{ GeV}$,

$$\text{(PMAS(54,1)=PMAS(56,1)=200.0)}$$

- The decays of the ω_T and ρ_T^0 were forced to $\gamma \pi_T / \pi_T'$.
- The decays of the π_T and π_T' were forced exclusively to $b\bar{b}$.
- Parton Distribution function: CTEQ3M (MSTP(51)=2)
- $\sin\chi = \sin\chi' = 1/3$ – Mixing angle between π_T / π_T' and mass eigenstates
(PARP(141) = PARJ(144) = 0.3333)
- $F_T = 82 \text{ GeV}$ – The π_T decay constant
(PARP(142) = 82.0)
- $Q_U = Q_D + 1 = 4/3$ – Charge of techniquarks
(PARP(143)=1.333)
- $N_{TC} = 4$ – Number of technicolors
(PARP(144)=4.0)

- $C_C = C_B = C_\tau = 1.0$ – Coefficient of decay to charm, bottom, τ respectively
(PARP(145)=PARP(146)=PARP(148)=1.0)
- $C_t = 0.0182$ – Coefficient of technipion decays to top, estimated to be M_b/M_t
(PARP(147)= 0.0182)
- $C_\pi = 0$ – Coefficient of decay of π_T to gg
(PARP(149)=0.0)
- $C_{\pi'} = 4/3$ – Coefficient of decay of π'_T
(PARP(150)=1.33333)
- $M_V = M_A = 100$ – Vector and Axial vector scales, respectively for decays to transverse gauge bosons and π_T 's
(PARJ(172)=PARJ(173)=100.0)
- Isospin violating ω_T/ρ_T^0 amplitude = 0.05
(PARJ(175)=0.05)

APPENDIX B OTHER EXPERIMENTAL SEARCHES FOR TECHNICOLOR

This appendix is a brief synopsis of the searches for the lightest technicolor mesons, the color-singlets $\omega_T, \rho_T^{0,\pm}$, and the $\pi_T^{0,\pm}$. I only mention the searches for a signature similar to the one presented in this analysis. There are also numerous searches for leptoquarks and color-octet particles, which both have connections to technicolor phenomenology.

Searches at CERN Large Electron Positron (LEP) Collider Experiments

The L3 collaboration search [34] looks for the signatures

$$\begin{aligned} e^+e^- &\rightarrow \rho_T^0 \rightarrow W^+W^-; W_L^\pm \pi_T^\pm \rightarrow l\nu_l bc \\ &\rightarrow \pi_T^+ \pi_T^- \rightarrow c\bar{b}b\bar{c} \\ &\rightarrow \gamma \pi_T^0 \rightarrow \gamma b\bar{b} \end{aligned}$$

The exclusion plot of Figure B.1 indicates the 95% CL limits on the technicolor production cross section times branching ratios for all of the processes mentioned. The darkened area indicates the excluded region, and the light area indicates where the search was not sufficiently sensitive due to the lower cross-section.

Similarly, the DELPHI collaboration [35] simultaneously searches for the same channels, since it is also an e^+e^- experiment. Figure B.2 shows this combination of results.

The LEP measurements are very sensitive, partly due to the “radiative return” effect in e^+e^- collisions, which causes the energy to vary. In addition, the e^+e^- cross-section at the ρ_T^0 resonance is very large since it mixes with the W_L^\pm . There is a possibility that the LEP searches may have used an obsolete cross-section calculation as noted in [33], hence comparison with this analysis is only qualitative at best.

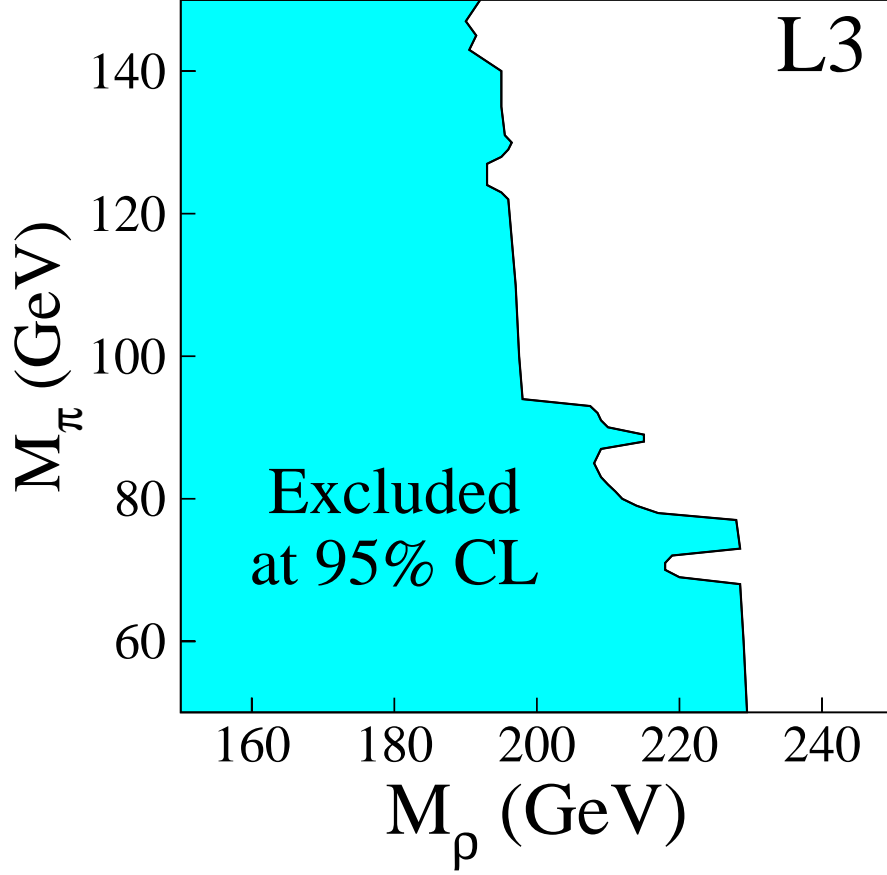


Figure B.1 The mass exclusion region measured by the L3 collaboration [34].

Searches at Fermilab

The CDF collaboration searches involved the final state of lepton + 2 jets with a single b -tag, and photon + 2 jets with a b -tag:

$$\begin{aligned}
 q\bar{q} \rightarrow W^\pm, \gamma, Z^0 \rightarrow \rho_T^\pm \rightarrow W_L^\pm \pi_T \rightarrow l^\pm \nu_l b + jet \\
 \rightarrow \rho_T^\pm, \rho_T^0, \omega_T \rightarrow \gamma \pi_T \rightarrow \gamma b + jet
 \end{aligned}$$

Figure B.3 shows the 95% mass exclusion limits in the leptonic ($l\nu_l b + jets$) channel, and figure B.4 shows the corresponding results in the $\gamma b + jets$ search. Similarly to the LEP measurements, the cross-section model is not the most up-to-date, and used an older version of PYTHIA (v 6.1) to compute the cross-sections. The analysis of this thesis uses v 6.126. Regardless of the theoretical cross-section model, the searches find no large deviations (they are less than $2 - \sigma$) between data and background.

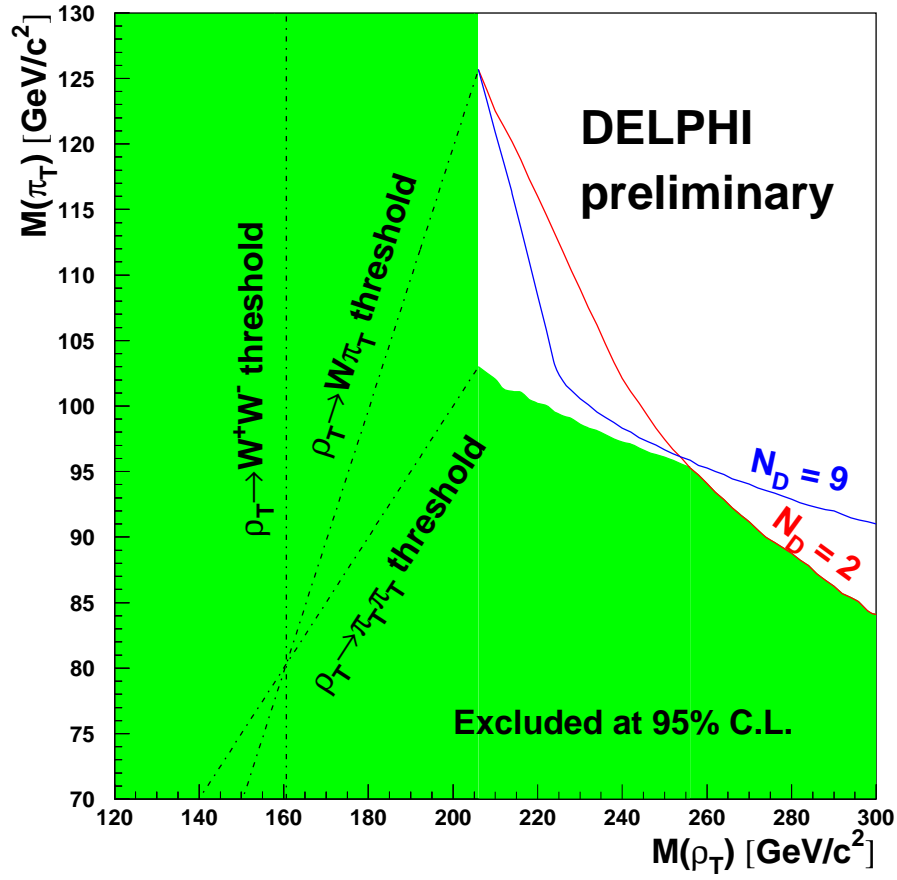


Figure B.2 The mass exclusion region measured by the DELPHI collaboration [35].

By re-analysing the Drell-Yan data, the DØ collaboration has searched for the unique channel

$$q\bar{q} \rightarrow \rho_T^0, \omega_T \rightarrow e^+e^-$$

As with the other searches, no significant deviations were found, and cross-section limits at the 95% CL were computed as shown in Figure B.5.

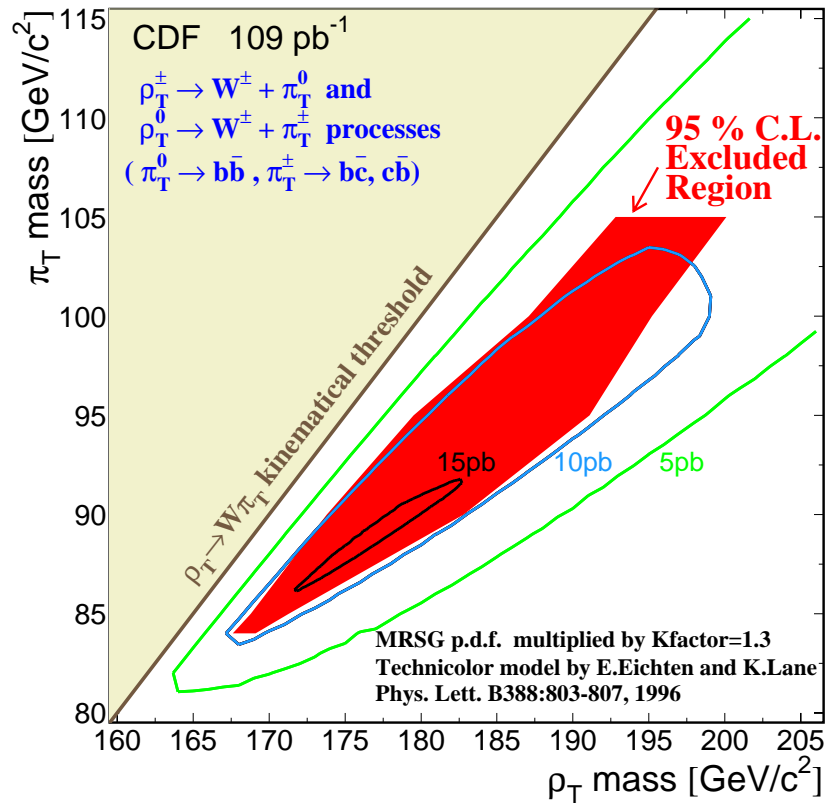


Figure B.3 The mass exclusion region measured by the CDF collaboration [36].

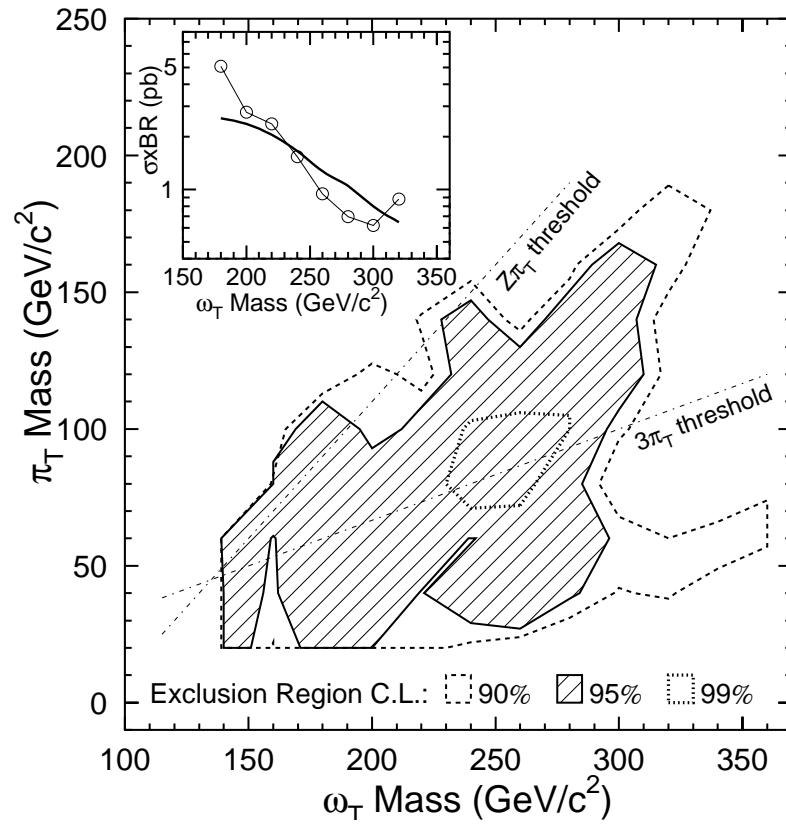


Figure B.4 The mass exclusion region measured by the CDF collaboration [37].

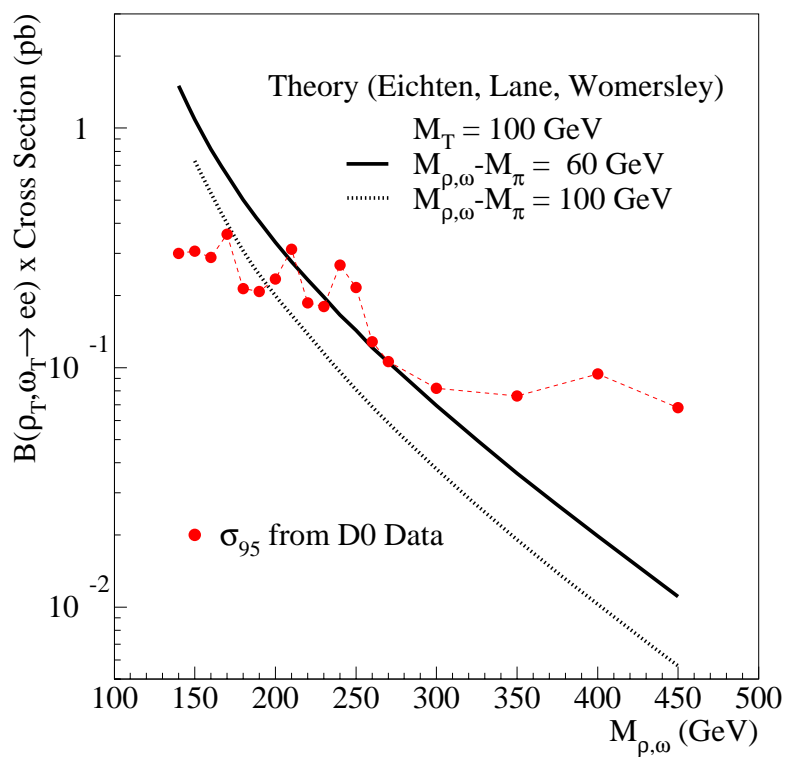


Figure B.5 The mass exclusion region measured by the DØ collaboration [38].

BIBLIOGRAPHY

- [1] Particle Data Group, “Review of Particle Physics,” *European Physics Journal* **C15** 1 (2000).
- [2] D. Griffiths, *Introduction to Elementary Particles*, (John Wiley & Sons, 1987).
- [3] M. Kaku, *Quantum Field Theory: A Modern Introduction*, (Oxford University Press, 1993).
- [4] M. Peskin, D. Schroeder, *An Introduction to Quantum Field Theory*, (Addison-Wesley, 1995).
- [5] E. Eichten, K. Lane and J. Womersley, “Finding Low-Scale Technicolor at the Tevatron,” *Phys. Lett.* **B405** 305 (1997), hep-ph/9704455; E. Eichten, K. Lane, “Low-Scale Technicolor at the Tevatron,” *Phys. Lett.* **B388** 803 (1996), hep-ph/9607213.
- [6] K. Lane, “Technihadron Production and Decay in Low-Scale Technicolor,” *Phys. Rev.* **D60** 075007 (1999), hep-ph/9903369; K. Lane, “Technihadron Production and Decay Rates in the Technicolor Straw Man Model,” hep-ph/9903372.
- [7] F. Halzen, A. Martin, *Quarks & Leptons: An Introductory Course in Modern Particle Physics*, (John Wiley & Sons, 1984).
- [8] S. Weinberg, “Implications of dynamical symmetry breaking,” *Phys. Rev.* **D13** 974 (1976); S. Weinberg, “Implications of dynamical symmetry breaking: An addendum,” *Phys. Rev.* **D19** 1277 (1979); L. Susskind, “Dynamics of spontaneous symmetry breaking in the Weinberg-Salam theory,” *Phys. Rev.* **D20** 2619 (1979).
- [9] T. Abu-Zayyad, *et. al.*, “Measurement of the Cosmic Ray Energy Spectrum and Composition from 10^{17} to $10^{18.3}$ eV Using a Hybrid Fluorescence Technique,” Submitted to *Astrophys J.*, astro-ph/0010652 (October 2000).
- [10] P. Bhattacharjee, G. Sigl, “Origin and Propagation of Extremely High Energy Cosmic Rays,” *Phys. Rept.* **327** 109 (2000), astro-ph/9811011.
- [11] J.M. Conrad, M.H. Shaevitz, T. Bolton, “Precision Measurements with High Energy Neutrino Beams,” *Rev. Mod. Phys.* **70** No.4 (1998).
- [12] S. Abachi *et al.*, “The DØ detector,” *Nuclear Instruments and Methods in Physics Research* **A338** 185 (1995).
- [13] K. Kleinknecht, *Detectors for Particle Radiation*, (Cambridge University Press, 1986).
- [14] T. Sjostrand, “High-Energy Physics Event Generation with PYTHIA 5.7 and JETNET 7.4,” *Comp. Phys. Commun.* **82** 74 (1994).
- [15] F. Carminati, *et al.*, “GEANT User’s Guide,” CERN program Library (1991).
- [16] W. Merritt, A. Jonckheere, “A D0GEANT Condensed User’s Guide (revised),” D0 Note 1373 (unpublished) (1995).

- [17] S. Abachi, *et al.*, “Search for a Forth Generation Charge -1/3 Quark via Flavor Changing Neutral Current Decay,” *Phys. Rev. Lett.* **78** 3818 (1997), FERMILAB-PUB-96/430-E, hep-ex/9611021; H. Greenlee, M. Narain, P. Singh, “The search for a forth generation quark (b') using flavor-changing neutral current decay signatures,” D0 note 3133 (unpublished) (1996).
- [18] B. Abbot, *et al.*, “Extraction of the Width of the W Boson from Measurements of $\sigma(p\bar{p} \rightarrow W + X) \times BR(W \rightarrow e + \nu)$ and $\sigma(p\bar{p} \rightarrow Z + X) \times BR(Z \rightarrow ee)$ and their Ratio,” *Phys. Rev.* **D61** 072001 (2000). The luminosities for a given trigger are computed using the DØ Luminosity Data Base.
- [19] B. Lauer, “A Search for High Mass photon pairs in $p\bar{p} \rightarrow \gamma\gamma jj$ events at $\sqrt{s} = 1.8 \text{ TeV}$,” Ph.D. Thesis, Iowa State University (1997). B. Abbott, *et al.*, “Search for High Mass Photon Pairs in $p\bar{p}$ collisions at $\sqrt{s} = 1.8 \text{ TeV}$,” *Phys. Rev. Lett.* **82** 2244 (1999).
- [20] W. G. Cobau, H. Greenlee, J. D. Hobbs, P. Tamburello, Z. H. Zhu, “Soft μ Tagging of Jets in Multi-Jet Events,” DØ note 2863 (unpublished) (1996).
- [21] John M. Butler, “Update on b-Tag Muon ID,” DØ note 2781 (unpublished) (1995); P. Quintas, “Reconstruction and Selection Efficiencies for High p_T Muons in Run 1B,” DØ Note 2865 (unpublished) (1996).
- [22] Brian Connolly, personal communication.
- [23] S. Abachi, *et al.*, “Measurement of the top quark pair production cross section using all jets decay channel,” *Phys. Rev. Lett.* **83** 1908 (1999).
- [24] J. McDonald, “Search for Single Top Production with the DØ Detector at the Fermilab Tevatron Collider,” Ph.D. Thesis, Florida State University (1999).
- [25] P. Bhat, “Multivariate Discriminant Analysis and Neural Networks,” DØ note 3136 (unpublished) (1996); P. Bhat, H.B. Prosper, “Comparison of Random Grid Search and Neural Network Methods in $t\bar{t} \rightarrow e + \text{jets}$ analysis,” DØ note 2794 (unpublished) (1995); H.B Prosper, “Some Mathematical Comments on Feed-Forward Neural Networks,” DØ note 1606 (unpublished) (1993).
- [26] C. Peterson, T. Rönvaldsson, “JETNET 3.0 – A Versatile Artificial Neural Network Package,” CERN-TH.7135/94.
- [27] P. K. Simpson, *Artificial Neural Systems: Foundations, Paradigms, Applications, and Implementations*, (Pergamon Press, 1990).
- [28] B. Knuteson, “The Random Grid Search Helper,” DØ note 3619 (unpublished) (1999).
- [29] N. Amos, C. Stewart, P. Bhat, *et al.*, “The Random Grid Search: A Simple Way to Find Optimal Cuts” Given at the Computing in High Energy Physics Conference, Rio de Janeiro, Brazil (1995).
- [30] I. Bertram, *et al.*, “A Recipe for the Construction of Confidence Limits,” Fermilab-TM-2104, DØ note 3476, (unpublished) (1999).
- [31] J. Hobbs, “Simple Limit Calculator,”
http://www-d0.fnal.gov/hobbs/limit_calc.html
 See the section on “Running the program by hand” (April 2001).
- [32] B. Knuteson, “Algorithms for Computing Significance,” DØ note 3345 (unpublished) (1997).
- [33] K. Lane, “Technicolor Signatures– Ieri, Oggi E Domani,” hep-ph/0006143 (July 2000).
- [34] The L3 Collaboration, “Search for Technicolor Production at LEP”, L3 Note 2428, submitted to the International Europhysics Conference High Energy Physics 99, Tampere, Finland 15–21 July 1999; <http://l3www.cern.ch/conferences/EPS99>.

- [35] The DELPHI Collaboration, “Search for Technicolour Production at LEP,” DELPHI Note 2000-088 CONF 387, paper No. 375, presented at the XXXth International Conference on High Energy Physics, July 2000, Osaka, Japan.
- [36] T. Affolder, *et al.*, “Search for Color Singlet Technicolor Particles in $p\bar{p}$ Collisions at $\sqrt{s} = 1.8$ TeV,” *Phys. Rev. Lett.* **84** 1110 (2000).
- [37] F. Abe, *et al.*, “Search for a Technicolor ω_T Particle in Events with a Photon and a b -quark Jet at CDF,” *Phys. Rev. Lett.* **83** 3124 (1999).
- [38] V.M. Abazov, “Search for Heavy Particles Decaying into Electron-Positron Pairs in $p\bar{p}$ Collisions,” Submitted to *Phys. Rev. Lett.* (2001), hep-ex/0102048.